The Pennsylvania State University
The Graduate School
Eberly College of Science

EQUILIBRIUM AND NON-EQUILIBRIUM PROPERTIES OF STRONGLY-INTERACTING BOSONS IN OPTICAL LATTICES

A Dissertation in
Physics
by
Wei Xu

Submitted in Partial Fulfillment
of the Requirements
for the Degree of

Doctor of Philosophy

May 2018

The dissertation of Wei Xu was reviewed and approved* by the following:

Marcos Rigol
Professor of Physics
Dissertation Advisor, Chair of Committee

David S. Weiss
Professor of Physics

Jainendra K. Jain
Professor of Physics

Ram M. Narayanan
Professor of Electrical Engineering

Nitin Samarth
Professor of Physics, Department Head

*Signatures are on file in the Graduate School.

Abstract

This dissertation serves as a summary of my Ph.D. work numerically studying equilibrium and non-equilibrium properties of strongly-interacting one-dimensional (1D) boson systems. This work is motivated by the fact that 1D systems are realizable and highly controllable with ultracold atoms in optical lattice and atom chip experiments. We apply a recent worm algorithmic Monte Carlo approach developed for 1D continuous systems to study their equilibrium properties, both with and without an underlying lattice. We also apply an exact lattice approach based on the Bose-Fermi mapping to check our Monte Carlo results in the Tonks-Girardeau limit, and more importantly, to study far-from-equilibrium expansion dynamics of the systems.

We first study the scaling of one-particle correlations of the harmonically trapped Lieb-Liniger gas with changing temperature and interaction strength. Based on the universal behaviors of the density and momentum profiles, we are able to determine the effective parameters needed to fully characterize the system. We also find that the Tonks-Girardeau limit at low temperatures is the ideal regime for the experimental observation of the $1/k^4$ momentum tail.

An extra periodic lattice can drive the transition from superfluid to Mott insulator states. Exact and complete phase diagrams for such transitions are

available only in the weak interacting and deep lattice limit, in which the system can be described using one-band Bose-Hubbard model. Beyond this limit, we use the worm algorithm in continuous space to map out the phase diagrams at various interaction strengths. We compare our phase diagrams with one-band Bose-Hubbard predictions and identify the regime where the one-band description breaks down. We introduce an inverse confined scattering solution to obtain effective Hubbard parameters, with which the Bose-Hubbard model provides correct results for strong interactions and deep lattices at unit filling.

In addition to the equilibrium properties, we also study the expansion dynamics of ultracold atoms in the hard-core limit. Experimentally, this is usually achieved by turning off confining potentials and letting atoms expand in optical lattices. Theoretical studies from initial ground states predicted the occurrence of fermionization of the momentum distribution after long expansion times. In addition, quasicondensation at finite momenta emerges when expanding from Mott insulating domains. Here, we develop a finite-temperature extension of the lattice approach for dynamics. We find the dynamical ferminoization of the momentum distributions at all temperatures. For expansion from initial Mott domains, we observe enhanced correlations reminiscent of dynamical quasicondensation. Surprisingly, we find the systems appear to cool down during the melting of the Mott domains. We use an emergent local Hamiltonian to understand these emergent phenomena.

Table of Contents

List of Figures

List of Tables

List of Symbols

$\hat{\rho}$	The density matrix operator, p. 10
Z	The partition function, p. 10
$\Delta\tau$	Discretization of virtual time in path integral formulation, p. 11
P	Number of time slices in path configuration space, p. 11
$\bar{M}$	Upper limit of the cut/insert length of a worm, p. 18
C	Hyperparameter controlling ratio between diagonal and off-diagonal configurations, p. 18
g_{1D}	Effective one-dimensional coupling strength, p. 23
a_{1D}	Effective one-dimensional scattering length, p. 23
γ	Tuning parameter of the Lieb-Liniger model, p. 23
$\hbar$	Planck constant, p. 23
K	Tomonaga-Luttinger liquid parameter, p. 25
ρ_s	The superfluid density, p. 26
J	Nearest neighbor tunneling, p. 29
a_{HO}	Harmonic oscillator length, p. 31
k_B	Boltzmann constant, p. 31
$\mathcal{C}$	Tan's contact, p. 33
k_L	Wavevector of the external periodic lattice potential, p. 49

U Hubbard onsite interaction, p. 50

E_R The recoil energy, p. 59

λ_η Natural orbital occupations, p. 84

λ_0 Zeroth natural orbital occupation, p. 89

R Characteristic length of a power-law trap in lattice, p. 96

Acknowledgments

The biggest impression of State College is its colorful autumn and amazing winter with beautiful snows, and of course, life for the past five years are impressive as well. Thus I would like to first thank the department of physics at Penn State, who provided me such a great opportunity to have my Ph.D study here.

I am also fortunate to be able to join my advisor Prof. Marcos Rigol's group in my second year after his moving to Penn State, and start the wonderful journey of exploring the quantum world in one dimension. I would like to thank Prof. Rigol for providing a nice research environment, and bringing his insights and rigorousness into guiding my research. I also want to thank Prof. Rigol for his many important advises and patience in shaping me into a qualified scientist. More importantly, I want to give a joint thank to Prof. Rigol and his wife for preparing yummy food for us every Thanksgiving.

The beginning of research is always very difficult. I want to express my gratitude to all individuals who showed me guidance, especially Prof. Rigol. In addition, special gratefulness should go to Prof. Nikolay Prokof'ev, for providing us with the worm algorithm source code and carefully explaining many difficult questions I encountered during my implementation of the method. Prof. Adrian Del Maestro introduced me several high-level details of the worm algorithm in our private

discussions. Juan Carrasquilla also explained many details of the code and provided helpful resources related to implementing the worm algorithm. Zhiyuan Yao and Chao Zhang suggested some ideas for correctly implementing the finite-size scaling of the superfluid density with the worm code. Rubem Mondaini taught me basic concepts about Monte Carlo methods and was always patient to help when I had issue with running jobs on computer clusters. Baoming Tang provided excellent resource for MPI implementation and many other useful techniques. Apart from playing with the worm code, Yinghai Wu also taught me how to diagonalize single-particle or many-body Hamiltonians with Lapack. Without this technique at hand and his guidance, I will not be able to have a lot of fun exploring many interesting condense matter systems, such as topological insulators and fractional Hall effect.

This is definitely not the end of the story. Many more people helped during my subsequent researches. I would like to thank Prof. Maxim Olshanii for sharing with us a beautiful inverse scattering solution. This leads to a better understanding of the phase diagrams we obtained with worm algorithm. I want to also thank Lev Vidmar for clarifying many interesting questions with the expansion dynamics of hard-core bosons. I want to express my sincere gratitude to Prof. David Weiss for the opportunity to collaborate with the BEC group. Thus I was able to know many aspects of the state-of-the-art ultracold atom experiments. Specifically, I want to thank Lin Xia, Joshua Wilson and Neel Malvania, and there is a lot of fun to work with them.

In addition, I want to thank many individuals who make life full of fun here at Penn State. I can still remember how Yinghai Wu clarified all roles in X-men. I can also remember how fun it is to drive on the highway during my very first day

of driving, thanks Teng Zhang. And there are many many people, I want to give joint thank to all you guys!

In the end, I want to leave an extra paragraph for my sole beloved one, my wife Ying Yang. It is the forever unforgettable moment that we got married during my Ph.D study, and I appreciate in my heart that we had the opportunity to face all good and difficult times together. I have no better words to express my love to you! I want to also thank deeply our family members, our fathers and mothers, our sisters, for their support to us over the years, especially for the years my wife and I were both away from them. We miss all of you! We want to also express our sincere gratitude to Yu Pan and Qingze Wang, Yufei Shen, Zhong Lin, for their many helps to us.

The scientific research will not be possible without the funding support from the National Science Foundation and the Office of Naval Research. Most computations in the dissertation were performed in the Institute for CyberScience at Penn State and the Center for High-Performance Computing at the University of Southern California. The staff members are always very helpful, and I want to thank them for their dedication to maintaining such high performance computer clusters.

Dedication

To my beloved family, and my friends

Chapter 1

Introduction

1.1 Background

Developments in ultracold atomic gas experiments have boosted the study of many-body interaction effects in bosonic systems [1, 2]. In particular, the ability to load Bose-Einstein condensates (BEC) in optical lattices has provided a unique opportunity to control the effective dimensionality and interactions of Bose gases. A setup that is of interest to us is that of a BEC loaded in a two-dimensional (2D) optical lattice, as a result of which it splits into an array of cigar-shaped Bose gases at very low temperatures [2]. For a sufficiently deep 2D optical lattice and low energies, each cigar-shaped Bose gas can behave as an effective 1D system [3, 4] that is described by the Lieb-Liniger model [5, 6] (plus an additional term to account for trapping potentials), see Fig. 1.1 for a schematic of the experimental setup (from Ref. [7]). The effective 1D interaction strength is determined by the three-dimensional (3D) scattering length and the transverse confinement provided by the lattice [8]. For sufficiently strong effective 1D interactions and sufficiently low 1D densities, these gases enter the so-called Tonks-Girardeau regime [9, 10], in which bosons behave as impenetrable particles (hard-core bosons) and can be mapped onto noninteracting fermions [11].

The Lieb-Liniger model has attracted much attention since its introduction more than 50 years ago [2, 12]. It is an integrable model whose exact solution, which can be obtained using the Bethe ansatz [5], provides insights into the universal behavior of 1D gapless systems. Its far-from-equilibrium dynamics has been recently scrutinized theoretically [13–18], after experiments showed that 1D

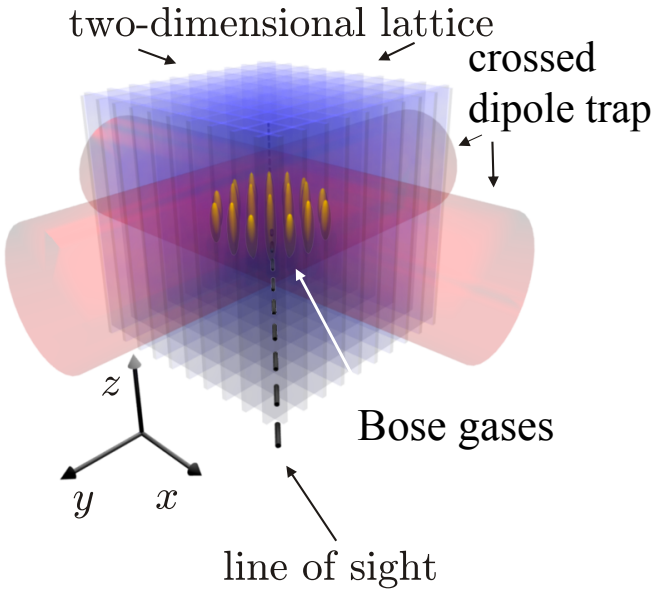

Figure 1.1: Schematic of an experimental setup creating a 2D optical lattice. The experiment begins with a BEC of ^{87}Rb atoms in the crossed-dipole trap. The pair of retro-reflected lattice beams in the $x-y$ plan are then slowly ramped up to form a very deep 2D optical lattice. Each grid line represents a cigar-shaped 1D Bose gas in the longitudinal direction. – Figure adapted from (Li *et al.*, 2013). –

Bose gases taken far from equilibrium relax to states in which observables are not described by traditional ensembles of statistical mechanics [19] and generalizations of the latter are needed [20, 21].

Despite the fact that the Lieb-Liniger model is Bethe ansatz solvable, the calculation of correlation functions is extremely challenging due to the complexity of the Bethe ansatz eigenfunctions. In the ground state, for example, the evaluation of one-particle correlations (of which the momentum distribution function is the Fourier transform) has only been possible numerically within algebraic Bethe ansatz [22], and through diffusion Monte Carlo simulations [23, 24]. At finite temperatures, they have been calculated using simulations within the stochastic gauge method [25]. Remarkably, the asymptotic behavior of the momentum distribution function $[m(k)]$, for large values of the momentum k (associated with short range correlations), has been determined analytically $[m(k) \propto k^{-4}]$ [26]. In the Tonks-Girardeau regime, the simplification introduced by the mapping to noninteracting fermions has enabled

the analytic calculation of one-particle correlations at zero and finite temperatures [27–34]. On the other hand, the 1D Bose-Hubbard model *is not* integrable, so correlations can only be computed numerically [2]. However, its Tonks-Girardeau limit is integrable and can be mapped onto the so-called XX chain [2], which is the isotropic limit of the XY chain introduced by Lieb, Shultz, and Mattis [35], and which can be mapped onto noninteracting fermions [2]. This way, it is possible to calculate analytically one-particle correlations of the Tonks-Girardeau gas in the presence of a lattice [36, 37].

In experiments with ultracold gases, a confining potential (that is, to a good approximation, harmonic) is needed to contain the gas. In the presence of such a confining potential, as in the Hubbard model, only the limit in which bosons are impenetrable (hence, mappable to noninteracting fermions) remains integrable. In this limit, the ground-state density and momentum distribution functions, as well as one-particle correlations, have been studied in the continuum [38–43] and in the lattice [44, 45]. In those studies, universal power laws with the same exponents as the ones known from homogeneous systems were found. At finite temperatures, a systematic study of one-particle observables has only been reported in the lattice [46], while, in the continuum, the momentum distribution function was recently calculated in Ref. [32] for trapped systems with five particles. For finite interaction strengths, for which trapped systems are not integrable anymore, quantum Monte Carlo simulations (with a lattice discretization) have been used to compute momentum distribution functions in the continuum and compare them with experimental results at relatively weak interactions, obtaining a good agreement between the two [47].

For the setup in Fig. 1.1, an additional (weaker) lattice can be added along the longitudinal direction, which has been of much interest in condensed matter physics [48]. Experiments in the presence of that additional lattice have allowed for the observation of the superfluid to Mott insulator transition in one dimension [49] and the lattice version of the Tonks-Girardeau regime [50]. The Mott insulator transitions are best understood for weak contact interactions and deep lattices, a regime that can be modeled using the one-band Bose-Hubbard model [48, 51]. The phase diagram of this model has been studied in great detail using a wide variety of computational techniques [52–56]. It is well established that the phase transition driven by changing the site occupancies (incommensurate transition)

belongs to the mean-field universality class, while the one with constant integer filling (commensurate transition) belongs to $(d+1)XY$ universality class [2].

One-band (or few-band) effective lattice models, such as the Fermi-Hubbard and t-J models for strongly interacting fermions [57, 58] and the Bose-Hubbard model for strongly interacting bosons [2, 59], have played a central role in our understanding of the interplay between quantum fluctuations, interactions, and lattice effects in a wide range of physical systems ranging from solid-state materials to optical lattices. Unfortunately, many-body interactions make it difficult to establish the limits of applicability of such models, as well as to explore how changes in the way effective parameters are calculated extend their relevance.

For bosons, beyond the one-band approximation, it is known that in one dimension an arbitrarily weak lattice can lead to the formation of a Mott-insulating phase in the strong interaction regime at integer fillings [60, 61]. This "pinning" transition is described by the (1+1) quantum sine-Gordon model [2, 62] and has been studied very recently [63, 64]. Multiband effects have also been seen in collapse and revival experiments in three dimensions, in which they were recast into renormalized multibody interactions [65, 66], and in theoretical studies of quench dynamics [67–69]. Together with other effects such as density-induced tunneling [70], as well as long-range interactions and tunneling [71], these studies have highlighted the necessity to go beyond the standard Bose-Hubbard model to describe many experiments (for a recent review, see Ref. [72]). These questions motivate us to study 1D systems of bosons with strong contact interactions in the presence of a lattice. We map out the exact phase diagrams for both weak and strong interaction strengths, and developed an effective approach to calculate the Hubbard parameters, which extends the validity of the Bose-Hubbard description to the strong interaction region at unit filling.

Another interesting question is the far-from-equilibrium dynamics of isolated quantum systems. Generally, nonequilibrium dynamics results in states in which observables can be described using equilibrium statistical mechanics, predicted by eigenstate thermalization hypothesis [73]. Nevertheless, there are many examples of intriguing outcomes of quantum dynamics. Some are the result of designing controllable dynamical protocols to create states of matter that do not exist in equilibrium, e.g., long-lived nonequilibrium states after short photoexcitation pulses [74, 75] and Floquet states [76, 77]. Others are the result of having current-

carrying states. Within the latter, recent studies have aimed at clarifying the role of (quasi-)local conserved quantities in transport in integrable systems [78–85], and generating interesting current-carrying states in closed quantum systems using inhomogeneous initial states [86–103]. Other remarkable dynamical phenomena that have recently attracted much attention are dynamical phase transitions [104–108] and discrete time crystals [109–111].

A subgroup of the far-from-equilibrium dynamics involves expansion dynamics of ultracold atoms in the presence of strong interactions. This is usually achieved by turning off confining potentials and letting atoms expand in optical lattices [112–115]. Of direct relevance to this thesis, theoretical studies of the expansion of hard-core bosons in one dimension predicted the occurrence of a dynamical fermionization of the momentum distribution [31, 89, 90] and of quasicondensation at finite momenta when the expansion begins from Mott insulating domains at unit filling [88, 90, 116, 117]. The latter was recently observed experimentally [115]. The effect of finite on-site (or nearest neighbor) interactions has been explored in bosonic (or spin) and fermionic systems in Refs. [82, 83, 91, 93, 98, 118–122], while changes induced by increasing dimensionality have been explored in Refs. [121, 123–125]. Another topic that has attracted much attention is the effect of multiple occupancies in the expansion in the presence of strong interactions [121, 126–130].

A common theme in the theoretical studies mentioned above is that the expansion always starts from initial pure states. It is in general unknown whether dynamical phenomena observed for pure states are robust enough to survive in experimentally realistic situations, in which initial states are expected to be in thermal equilibrium at nonzero (and sometimes not low) temperatures. Recently, a finite-temperature hydrodynamic approach [131] and an exact Fredholm determinant approach [33, 34] were developed to study breathing-mode oscillations and collective many-body bounces. The theoretical calculations were found to agree well with experimental results in Ref. [132]. Here, we introduce another exact lattice approach to study dynamics based on an existing finite-temperature equilibrium method [46].

Another important question involves understanding these emergent phenomena. An intriguing phenomenon is the emergence of coherence during the melting of initial Mott domains [88, 115]. It was pointed out in Ref. [133] that, for certain classes of quantum quenches involving pure states, there exist a local operator (an emergent

local Hamiltonian) of which the time-evolving state is an eigenstate. Namely, there exists an emergent eigenstate solution to the quantum dynamics. Whenever the time-evolving state is the ground state of the emergent local Hamiltonian, one can understand why ground-state-like correlations, such as those observed in Refs. [88, 115], can occur far from equilibrium. This is a typical behavior of gapless 1D systems in their ground states, which are well described by the Luttinger-liquid theory [134]. On the other hand, the emergent eigenstate solution also offers promising tools to engineer many-body states with ultracold atoms. Related ideas have been recently explored in the context of integrable Floquet dynamics [135] and counterdiabatic driving [136].

1.2 Overview of Chapters

In this thesis, we study properties of 1D bosons with contact interactions in the continuum. We apply the worm algorithm [137, 138] to study the effect of correlations for bosons with finite interaction strength. We obtain the ground-state phase diagrams of bosons within an external periodic potential at various interaction strengths, and compare them with the phase diagram of the Bose-Hubbard model. We develop an effective scattering theory in one dimension to calculate the Hubbard parameters, with which the Bose-Hubbard model can correctly describe our continuous setting in the strongly-interacting regime and at unity filling. In the infinite repulsion limit (i.e., the Tonks-Girardeau limit), we apply an exact numerical approach based on Bose-Fermi mapping on a lattice to study both equilibrium and non-equilibrium properties of the systems.

In Chapter 2, we review the key ingredients of the worm algorithm applied to the continuous-space path integral Monte Carlo (PIMC). We build from scratch the path integral configuration space, and introduce the simplest Monte Carlo solution using the primitive approximation. We explain the application of the pair-product approximation in practice to reduce the bias due to the finite time discretization $\Delta\tau$. We also discuss the physical meaning of the extended configuration space introduced in worm algorithm, and review in detail how the off-diagonal configurations can be used to construct the reduce one-body density matrix estimator.

In Chapter 3, we introduce the Lieb-Liniger model [5, 6] and its basic properties. Then we present an exact numerical study of the scaling of density and momentum

distribution functions of harmonically trapped 1D bosons with repulsive contact interactions at zero and finite temperatures. We use the PIMC with worm updates in our calculations at finite interaction strengths, and the Bose-Fermi mapping in the Tonks-Girardeau regime. We discuss the homogeneous case and, within the local density approximation, use it to motivate the scaling in the presence of a harmonic trap. For the momentum distribution function, we pay special attention to the high momentum tails and their k^{-4} asymptotic behavior.

In Chapter 4, we study phase diagrams of 1D bosons with contact interactions in the presence of a lattice. We use the worm algorithm in continuous space and focus on the incommensurate superfluid Mott-insulator transition. Our results are compared to those from the one-band Bose-Hubbard model. When Wannier states are used to determine the Bose-Hubbard model parameters, the comparison unveils an apparent breakdown of the one-band description for strong interactions, even for the Mott-insulating state with an average of one particle per site ($n = 1$) in deep lattices. We introduce an inverse confined scattering analysis to obtain the ratio U/J, with which the Bose-Hubbard model provides correct results for strong interactions, deep lattices, and $n = 1$.

In Chapter 5, we develop an exact approach to study the quench dynamics of hard-core bosons initially in thermal equilibrium in 1D lattices. This approach is motivated by the exact lattice method proposed for finite temperature in equilibrium [46]. The equal-time correlations can be calculated as the thermal average of the one-body density matrix operator in the Heisenberg picture. We apply this approach to study the sudden expansion of thermal states after confining potentials are switched off. We find that a dynamical fermionization of the momentum distribution occurs at all temperatures. This phenomenon is studied for low initial site occupations in a harmonic trap, for which the expansion of the cloud is self-similar. In this regime, the occupation of the natural orbitals allows one to distinguish hard-core bosons from noninteracting fermions. We also study the expansion of initial Mott insulating domains formed under an external linear potential at finite temperature, and show that the emergence of off-diagonal one-body correlations between hard-core bosons is suppressed gradually with increasing temperature. Surprisingly, the melting of the Mott domain is accompanied by an effective cooling of the system. We explain this phenomenon analytically using an equilibrium description based on an emergent local Hamiltonian proposed in Ref. [133].

Within the emergent eigenstate solution to quantum dynamics, one can construct a local operator, termed an emergent local Hamiltonian, of which the time-evolving state is an eigenstate. In Ref. [133], emergent local Hamiltonians were constructed for systems in which the pre-quench Hamiltonian is either the boost operator or the boost operator plus the final Hamiltonian. In Chapter 6, we show the existence of the emergent eigenstate solution for the expansion dynamics of Tonks-Girardeau gases in optical lattices after turning off power-law (e.g., harmonic or quartic) confining potentials, which are geometric quenches that do not involve the boost operator. For systems that are initially in the ground state and undergo dynamical fermionization during the expansion, we show that they remain in the ground state of the emergent local Hamiltonian at all times. On the other hand, for systems at nonzero initial temperatures, the expansion dynamics can be described by constructing a Gibbs ensemble for the emergent local Hamiltonian, which we call an emergent Gibbs ensemble.

Chapter 2

Path Integral Monte Carlo and the Worm Algorithm

This chapter is devoted to an introduction of the fundamentals of the worm algorithmic Monte Carlo technique introduced by N. V. Prokof'ev *et al* [137, 138]. We start with a review of important ingredients of the conventional PIMC method invented by D. M. Ceperley [139] (Sec. 2.1). We first construct the path integral configuration space in Sec. 2.1.2, and discuss a Monte Carlo (MC) solution under the primitive approximation in sec. 2.1.3. In Sec. 2.2, we construct a better action out of the interaction part of the Hamiltonian. For the case of bosons with contact interactions, the pair-product action is the best action to use [139]. Then, we move on to the discussion of worm algorithm in Sec. 2.3, and emphasize the advantages of the worm algorithm over the conventional PIMC. We pay special attention to the calculation of off-diagonal correlations, which is unique to the worm algorithm method, by explaining in detail the strategy to numerically construct the reduced one-body density matrix in Sec. 2.3.2.

2.1 Path Integral Monte Carlo

2.1.1 General Formulation

The MC method was introduced to effectively solve complex integrations. To show a simple and intuitive example, given the integral

$$\bar{f} = \int p(x) f(x) dx \ , \tag{2.1}$$

the MC way of calculating $\bar{f}$ is given by the following summation,

$$\bar{f}_{\rm MC} = \frac{1}{N} \sum_{\{x_i\}} f(x_i) \ , \tag{2.2}$$

where, x_i is sampled according to the distribution $p(x)$ with $\int p(x) = 1$, N is the number of points sampled.

In the quantum world, the distribution [the analog of $p(x)$] one cares about is set by the density matrix,

$$\hat{\rho} = e^{-\beta \hat{H}} \ , \tag{2.3}$$

where β is the inverse temperature, $\beta = 1/k_B T$, and $\hat{H}$ is the Hamiltonian (one-body or many-body) of the physical system under study. The job of the MC technique is to effectively simulate a distribution of $\hat{\rho}$ within a physical configuration space, e.g., real space. The expectation value of the physical observable $\hat{O}$ can be expressed by the following general formula,

$$\langle \hat{O} \rangle = {\rm Tr}[\hat{O}\hat{\rho}]/Z \ , \tag{2.4}$$

the normalization factor $Z = {\rm Tr}\hat{\rho}$ is the partition function.

A convenient basis to work with is the position basis, where individual particles are labeled by their positions. Under this basis expansion, the elements of the density matrix are non-negative and thus it avoids the sign problems in MC simulations [139]. Elements of $\hat{\rho}$ in the position basis can be expressed as,

$$\rho(R, R'; \beta) = \langle R | \, e^{-\beta \hat{H}} \, | R' \rangle \ , \tag{2.5}$$

where $R = \{r_1, ..., r_N\}$ is a set of positions of particles. $\rho(R, R'; \beta)$ can be interpreted as a propagator in Feynman's path integral formalism, by treating $i\beta$ as a virtual time. We can also write down the expression for the observables and partition function,

$$\begin{aligned} \langle \hat{O} \rangle &= Z^{-1} \int dR dR' \rho(R, R'; \beta) \, \langle R' | \, \hat{O} \, | R \rangle \\ Z &= \int dR \rho(R, R; \beta) \ . \end{aligned} \tag{2.6}$$

Since the density matrix involves exponentials of operators, one way to solve

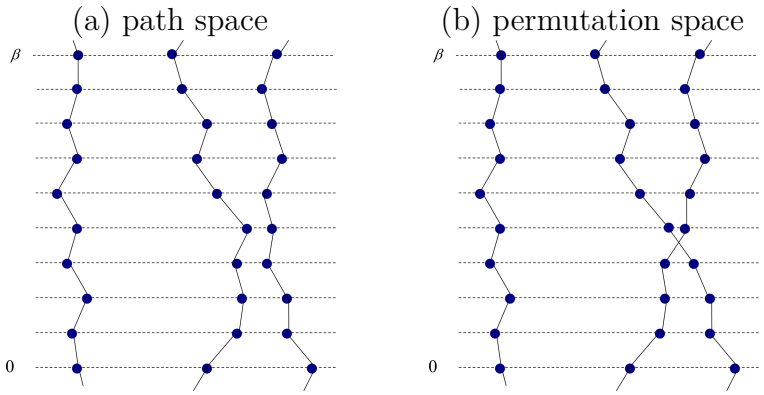

Figure 2.1: Example graphical views of two typical configuration spaces within the path integral formulation. The system contains three identical bosonic particles. (a) Configuration of three bosonic particles without permutations. (b) Configuration with permutation between particle 2 and 3.

Eq. (2.5) is to split β into P equal pieces $\Delta\tau = \beta/P$ (for large P). One can expand $\rho(R, R'; \Delta\tau)$ into a Taylor series and obtain a fair approximation depending on the cutting length of the series.

$$\rho(R_0, R_P; \beta) = \int D\{R\}\rho(R_0, R_1; \Delta\tau)\rho(R_1, R_2; \Delta\tau)...\rho(R_{P-1}, R_P; \Delta\tau)\ . \qquad (2.7)$$

Here, $D\{R\}$ is short for the product $dR_1 dR_2 ... dR_{P-1}$. Without an approximation for $\rho(R_{i-1}, R_i; \beta)$, Eq. (2.7) is still exact for any chosen value of the number of slices P.

2.1.2 Configuration Space

The kernel of the integral in Eq. (2.7) can be translated into easily understandable graphical representations. We use beads to represent positions of particles indicated by R_i at time slice i and bonds connecting particles at slice $i-1$ to particles at slice i to indicate the propagator $\rho(R_{i-1}, R_i; \Delta\tau)$. Fig. 2.1(a) shows an example of three identical bosonic particles. Since all the configurations in the partition function require $R_0 = R_P$, the beads positions at time $\tau = 0$ and $\tau = \beta$ should be equal, i.e., they should be merged to refer to the same time slice. As a result of the β periodicity, the world line configurations are closed loops on a $d+2$ dimensional cylinder [138].

By taking a further look at Eq. (2.7), one should notice that within each state

R_i, the position of individual particles are labeled and thus they are mutually distinguishable. To consider the indistinguishable nature of bosons, a permutation operation should be applied to the original wave function,

$$\hat{\mathcal{P}}\phi(R) = \frac{1}{N!}\sum_{\mathbf{P}}\phi(\mathbf{P}R) \ , \tag{2.8}$$

where $\mathbf{P}R = \{r_{P_1}, r_{P_2}, ..., r_{P_N}\}$ denotes a permutation of particle labels. Similarly, we can apply the permutation operator $\hat{\mathcal{P}}$ to the density matrix,

$$\hat{\mathcal{P}}\rho(R_0, R_M; \beta) = \frac{1}{N!}\sum_{\mathbf{P}}\rho(R_0, \mathbf{P}R_M; \beta) \ . \tag{2.9}$$

Consider the partition function in Eq. (2.6) again, when $R_0 = R_M$, a world line started at one bead position at time slice $\tau = 0$ could end up with another bead position at $\tau = \beta$, resulting in a closed world line that loops around the imaginary time interval multiple times before returning to its initial bead position. A graphical view of the example configuration resulting from permutation among particles is shown in Fig. 2.1(b).

2.1.3 Primitive Approximation

2.1.3.1 Introducing the Action

To proceed further, one is interested in constructing a working formula from Eq. (2.7). Here, we start with a benchmark example by applying the primitive approximation. With the primitive approximation, one can separate the original propagator into a product of kinetic and potential (including mutual interactions) part. The primitive approximation in stated as follows,

$$e^{-\Delta\tau\hat{H}} = e^{-\Delta\tau(\hat{T}+\hat{V})} = e^{-\Delta\tau\hat{T}}e^{-\Delta\tau\hat{V}}e^{-\frac{\Delta\tau^2}{2}[\hat{T},\hat{V}]} \approx e^{-\Delta\tau\hat{T}}e^{-\Delta\tau\hat{V}} \ . \tag{2.10}$$

In the limit of $\Delta\tau \to 0$ (or equivalently $P \to \infty$), the equality above becomes exact. Otherwise, it is obvious that the error is of the order $O(\Delta\tau^2)$. In the free particle basis, the kinetic propagator term is given by the free particle propagator with a

virtual time. The expression of the free propagator is shown below,

$$\begin{aligned}\rho_0(R_0, R_1; \Delta\tau) &= \left(\frac{1}{2\pi}\right)^d \int_k dk e^{ik(R_0-R_1)} e^{-i\hbar k^2 \Delta\tau/(2m)} \\ &= \left(\frac{m}{2\pi i\hbar\Delta\tau}\right)^{\frac{d}{2}} \exp\left[-\frac{m}{2i\hbar\Delta\tau}(R_0 - R_1)^2\right] .\end{aligned} \tag{2.11}$$

Taking $\Delta\tau \to i\Delta\tau/\hbar$ as the virtual time and $\lambda = \hbar^2/(2m)$, we get the free propagator in the path integral,

$$\begin{aligned}\rho_0(R_0, R_1; \Delta\tau) &= \langle R_0 | \, e^{-\Delta\tau \hat{T}} \, | R_1 \rangle \\ &= \left(\frac{1}{4\pi\lambda\Delta\tau}\right)^{\frac{Nd}{2}} \exp\left[-\frac{1}{4\lambda\Delta\tau}(R_0 - R_1)^2\right] .\end{aligned} \tag{2.12}$$

The potential (and interaction) term is diagonal,

$$\langle R_1 | \, e^{-\Delta\tau \hat{V}} \, | R_0 \rangle = e^{-\Delta\tau V(R_1)} \delta(R_0 - R_1) . \tag{2.13}$$

Thus we arrived at the expression for Eq. (2.7) under the primitive approximation,

$$\begin{aligned}\rho(R_0, R_P; \beta) = &\int D\{R\} (4\pi\lambda\Delta\tau)^{-dNP/2} \\ &\times \exp\left(-\sum_{m=1}^{P}\left[\frac{(R_{m-1} - R_m)^2}{4\lambda\Delta\tau} + \Delta\tau V(R_m)\right]\right) .\end{aligned} \tag{2.14}$$

A careful look at Eq. (2.14) reveals that it is composed of a complex Nd-dimensional integration of a kernel function. The kernel function is always non-negative given its exponential nature, thus it is safe to be solved with the MC technique without sign problem. One could further define the action as the negative log of the propagator $\rho(R_{m-1}, R_m; \Delta\tau)$ for a pair of time slices (R_{m-1}, R_m),

$$S^m = S(R_{m-1}, R_m; \Delta\tau) = -\ln[\rho(R_{m-1}, R_m; \Delta\tau)] , \tag{2.15}$$

then one immediately realizes that Eq. (2.7) can be interpreted as the path integration of the exponential of actions,

$$\rho(R_0, R_P; \beta) = \int D\{R\} \exp\left[-\sum_{m=1}^{P} S^m\right] . \tag{2.16}$$

Since the free propagator part is well formulated, we choose to split out its contribution to the action and denote it as the kinetic action K^m,

$$K^m = \frac{Nd}{2}\ln(4\pi\lambda\Delta\tau) + \frac{(R_{m-1} - R_m)^2}{4\lambda\Delta\tau} \,. \tag{2.17}$$

The rest of the action is called *inter-action*, denoted as U^m. Depending on the details of formulation and approximation made, different level of accuracies could be achieved for calculating U^m. Under the primitive approximation Eq. (2.10), the inter-action is given as,

$$U_1^m = \frac{\Delta\tau}{2}[V(R_{m-1}) + V(R_m)] \,. \tag{2.18}$$

The formulation above is chosen due to its symmetric nature. The superscript in U^m indicates the accuracy order with respect to $\Delta\tau$.

2.1.3.2 Energy Estimators

One should not confuse the actions defined above with energy estimators, which could be constructed from thermodynamics under specific ensemble assumptions. For example, in the canonical and grand-canonical ensemble, the total energy estimator is given as $E_T = -Z^{-1}\partial Z/\partial\beta$ and the kinetic energy is computed from $K_T = -m\beta^{-1}Z^{-1}\partial Z/\partial m$. The derivatives can be conducted directly on the path integral formulation of the partition function detailed in the previous subsections. Without making any assumption of the inter-action U^m, the relevant energy estimators are listed below,

$$\begin{aligned}
E_T &= \left\langle \frac{dN}{2\Delta\tau} - \frac{(R_{m-1} - R_m)^2}{4\lambda\Delta\tau^2} + \frac{\partial U^m}{\partial\Delta\tau} \right\rangle_m \\
K_T &= \left\langle \frac{dN}{2\Delta\tau} - \frac{(R_{m-1} - R_m)^2}{4\lambda\Delta\tau^2} + \frac{\lambda}{\Delta\tau}\frac{\partial U^m}{\partial\lambda} \right\rangle_m \\
V_T &= \left\langle \frac{\partial U^m}{\partial\Delta\tau} - \frac{\lambda}{\Delta\tau}\frac{\partial U^m}{\partial\lambda} \right\rangle_m \,.
\end{aligned} \tag{2.19}$$

The bracket with subscript m indicate an important sampling of different paths over the whole configuration space and average over different time slices. When

$\Delta\tau$ is small, the primitive approximation holds, thus U^m reduces to $\Delta\tau V(R_m)$,

$$\begin{aligned} K_T &= \left\langle \frac{dN}{2\Delta\tau} - \frac{(R_{m-1}-R_m)^2}{4\lambda\Delta\tau^2} \right\rangle_m \\ V_T &= \frac{1}{2}\left\langle V(R_{m-1}) + V(R_m) \right\rangle_m . \end{aligned} \tag{2.20}$$

It becomes computationally expensive to limit $\Delta\tau$ to be very small especially at very low temperature, simply because the number of time slices P becomes increasingly large. For moderately large $\Delta\tau$, the error within the primitive approximation increases linearly with $\Delta\tau$, leading to systematically biased estimators. With this in mind, a better strategy for constructing U^m should be considered. In addition, one should be aware that U^m also contains kinetic contributions at large $\Delta\tau$.

2.2 Constructing the Action

It is usually not possible to calculate the exact action directly. As pointed out when discussing the primitive approximation, due to the discrete nature of the β axis, different approximations can lead to systematic errors of different orders of $\Delta\tau$. Thus it is critical to have a good but inexpensive approximation to the exact action. A better approximation leads to faster convergence to the exact action when reducing $\Delta\tau$ and thus a much smaller number of slices P. The error of the action under the primitive approximation is proportional to $\lambda\Delta\tau^2$. Here we discuss a better approach for atoms with contact interactions, i.e., the pair-product action.

2.2.1 Pair-product Action

One can derive the Feynman-Kac formula by taking the $P \to \infty$ limit of the discrete path integral formula under the primitive approximation. Then the exact action for the interaction part can be written as an average over all free-particle paths,

$$e^{-U(R_0,R_F;\Delta\tau)} = \left\langle \exp\left[-\int_0^{\Delta\tau} V(R(t))dt \right] \right\rangle_{\mathrm{RW}} . \tag{2.21}$$

Then, considering a system with short-range pairwise interactions,

$$V(R) = \sum_{i<j} v(r_{ij}) \ , \tag{2.22}$$

and assuming that different particle pairs are uncorrelated with each other, Eq. (2.21) can be approximated with a product of averages over pairwise terms.

$$e^{-U} = \left\langle \prod_{i<j} x_{ij} \right\rangle \backsimeq \prod_{i<j} \langle x_{ij} \rangle \ . \tag{2.23}$$

The resulting action, named the pair-product action, is accurate up to order $\Delta\tau^2$.

$$U_2(R, R'; \Delta\tau) = \sum_{i<j} u_2(r_{ij}, r'_{ij}; \Delta\tau) \ . \tag{2.24}$$

2.2.2 Contact Interaction

Applying the pair-product action to 1D systems with contact interactions $v(r_{ij}) = \delta(r_i - r_j)$ is straightforward. The pair density matrix can be obtained directly from solving the time-dependent propagator of a particle in external delta potential [140, 141].

$$\rho(x, y; \Delta\tau) = \rho_0(x, y; \Delta\tau) - \frac{g}{2\lambda} \int_0^\infty du \exp\left(-\frac{g}{2\lambda} u\right) \rho_0(|x| + |y| + u, 0; \Delta\tau) \ . \tag{2.25}$$

This equation can be further simplified for numerical purposes introducing the error function.

$$\begin{aligned} \rho(x, y; \Delta\tau) = \rho_0(x, y; \Delta\tau) - \frac{g}{4\lambda} \mathrm{erfc}\left[\frac{|x| + |y| + g\Delta\tau}{\sqrt{4\lambda\Delta\tau}}\right] \\ \times \exp\left[\frac{g}{2\lambda}(|x| + |y|) + \frac{\Delta\tau g^2}{4\lambda}\right] \ . \end{aligned} \tag{2.26}$$

The complementary error function is defined as $\mathrm{erfc}[x] = 2/\sqrt{\pi} \int_x^\infty dt \exp(-t^2)$. Furthermore, a reduced mass $\mu = m/2$ is used here, hence $\lambda' = \hbar^2/(2\mu) = 2\lambda$.

Then the propagator related to the pair-product action is simplified as ρ/ρ_0:

$$\rho_\delta(x,y;\Delta\tau) = 1 - \frac{g}{2}\sqrt{\frac{\pi\Delta\tau}{\lambda'}}\exp\left[\frac{1}{4\lambda'\Delta\tau}(x-y)^2 + \frac{g}{2\lambda'}(|x|+|y|) + \frac{\Delta\tau g^2}{4\lambda'}\right] \times \mathrm{erfc}\left[\frac{|x|+|y|+g\Delta\tau}{\sqrt{4\lambda'\Delta\tau}}\right] . \tag{2.27}$$

To further simplify Eq.(2.27), one can define $s = (g/2)\sqrt{\Delta\tau/\lambda'}$, $z = 1/\sqrt{4\lambda'\Delta\tau}$, and $r = z(|x|+|y|)$, the propagator is [142]:

$$\rho_\delta(x,y;\Delta\tau) = 1 - \sqrt{\pi}s\exp[s(s+2r) + z^2(x-y)^2]\mathrm{erfc}[r+s] . \tag{2.28}$$

The pair action introduced in the previous section is related to the negative log of $\rho_\delta(x,y;\Delta\tau)$,

$$u_2(r_{ij}, r'_{ij};\Delta\tau) = -\ln\rho_\delta(r_{ij}, r'_{ij};\Delta\tau) . \tag{2.29}$$

Under the primitive approximation, the kinetic energy estimator K_T is unrelated to the inter-action U^m. Here, from the pair-production approximation, it is shown explicitly the contribution of U^m to both kinetic and interaction part of the energy estimators. In addition, the partial derivatives $\partial U^m/\partial\Delta\tau$ and $\partial U^m/\partial\lambda$ are both straightforward to calculate, thus one should always use the pair-product action in practice.

2.3 Worm Algorithm

The worm Algorithm [137, 138], introduced by N. Prokof'ev et al, is a big improvement over conventional PIMC. The worm algorithm improves the simulation efficiency by extending the configuration space of conventional PIMC to include additional configurations with one additional open world line (named a worm by convention). It seems unlikely that working with an enlarged configuration space can indeed be more efficient. The answer lies in the subsequent updates one can apply. In the conventional method, updates which generate highly correlated states are always exponentially more difficult to be accepted. This leads to ergodicity breaking with increasing system size. On the other hand, in the worm algorithm, it is much easier to reach highly correlated states by growing the worm and swapping

with its nearby world lines. The relative acceptance ratio of different updates can be controlled by several hyperparameters, including dimensionless parameter C which controls the relative statistics of open and close configuration spaces, the number of time slices P, and its cut/insert length $\bar{M}$.

The worm algorithm is not merely about efficiency and increased system sizes. It is also built on top of a grand canonical ensemble, thus supports exact computation of off-diagonal correlations.

2.3.1 Partition Function

It is worthwhile to further derive the partition function in a grand canonical ensemble. The section in the diagonal configuration space is given by $Z = \mathrm{Tr} e^{-\beta(\hat{H}-\mu\hat{N})}$, where the trace sums over all many-body eigenstates in different particle number sectors. After discretizing the time axis in a similar way, one gets the path integral representation of Z,

$$Z = \sum_{N=0}^{\infty} e^{\beta\mu N} \int D\{R\} A(\{R\}, \Delta\tau) e^{-U(\{R\})} \ , \tag{2.30}$$

where, μ is the chemical potential, $A(\{R\}, \Delta\tau)$ is a product of free propagators, $U(\{R\})$ stands for the inter-action. This part of the partition function is not that much different from the canonical counterpart, except that there is an additional summation over particle number sectors.

We denote the partition function for off-diagonal configurations Z', which is simply the configuration in Z with one additional open world line. Thus Z' could be constructed as follows,

$$Z' = C \sum_{j_{\mathcal{I}}, j_{\mathcal{M}}} \int dr_{\mathcal{I}} dr_{\mathcal{M}} g(r_{\mathcal{I}}, r_{\mathcal{M}}, \Delta\tau(j_{\mathcal{I}} - j_{\mathcal{M}})) \ . \tag{2.31}$$

Here, $g(r_{\mathcal{I}}, r_{\mathcal{M}}, \Delta\tau(j_{\mathcal{I}} - j_{\mathcal{M}}))$ is the product of Z with the propagator of the additional open world line. C is a dimensionless parameter, which controls the ratio between two sets of configurations. $\mathcal{M}$ and $\mathcal{I}$ is short for *Masha* and *Ira* respectively, which represent the start and end points of the worm. The names

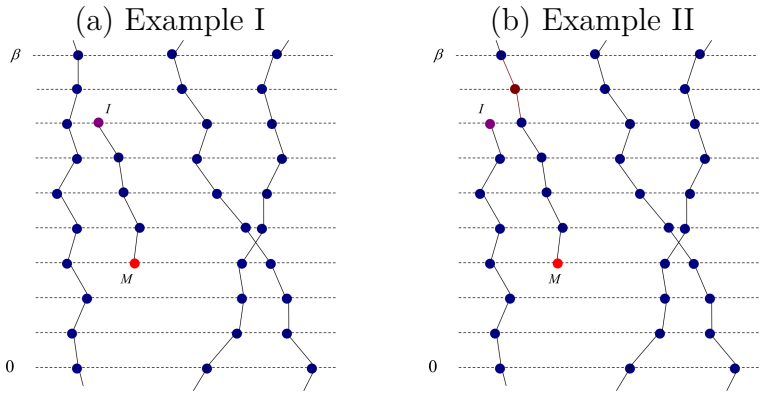

Figure 2.2: Example graphical views of two typical off-diagonal configurations. The system contains three identical bosonic particles. The diagonal configurations have already been shown in Fig. 2.1.

were given by the creators of the algorithm in Ref. [138].

$$\begin{aligned} \mathrm{prev}(\mathit{Masha}) &= 0 \\ \mathrm{next}(\mathit{Ira}) &= 0 \ . \end{aligned} \tag{2.32}$$

If we define the generalized partition function as $Z_W = Z + Z'$, then some simple statistical averages can be obtained immediately, such as the fraction of diagonal sectors,

$$\left\langle \delta^{(Z)} \right\rangle_{\mathrm{MC}} = Z/Z_W \ . \tag{2.33}$$

Taking into account the translational invariance in β and $r_{\mathcal{I}} - r_{\mathcal{M}}$, the fraction of off-diagonal sectors is

$$\left\langle \delta^{(G)} \right\rangle_{\mathrm{MC}} = \frac{CVP}{Z_W} \sum_{j=0}^{P-1} \int dr g(r, \Delta\tau j) \ . \tag{2.34}$$

The estimator for $g(r_{\mathcal{I}} - r_{\mathcal{M}}, \Delta\tau j)$ is also straightforward to obtain,

$$\frac{CVP}{Z_W} g(r_0, \Delta\tau j_0) = \left\langle \delta^{(G)} \delta_{j,j_0} \delta(r - r_0) \right\rangle_{\mathrm{MC}} \ . \tag{2.35}$$

2.3.2 Reduced Density Matrix Estimators

Here, we further elaborate on the construction of a working estimator for the Green function $G(r_{\mathcal{M}}, r_{\mathcal{I}}; t)$, which cannot be accessed by conventional PIMC method. To

simplify the problem, we focus on Green functions averaged over spatial translations and at time β, that is $\bar{G}(r_{\mathcal{I}} - r_{\mathcal{M}}, \beta)$. In this case, it is convenient to fix $r_{\mathcal{M}} = 0$ and $t_{\mathcal{M}} = 0$.

Practically, only off-diagonal configurations contribute to $\bar{G}(r, \beta)$. To save more computation time, as oppose to the sampling method in Eq. (2.35), one can choose to elongate the short worm $j_{\mathcal{I}} - j_{\mathcal{M}} < P$ (including $j_{\mathcal{I}} < j_{\mathcal{M}}$) to length P. For example, given an off-diagonal configuration, denoted $\mathcal{D}_{\xi}(r, j)$, where (r, j) is the position and time slice of *Ira* and ξ stands for all other variables of the configuration. To upgrade the worm, we randomly sample the rest of the path following the same strategy as in the *Advance* move (see Ref. [138] for details). More specifically,

$$\mathcal{D}_{\xi}(r, P) = \mathcal{D}_{\xi_0}(r_0, j) R_{jP}(r_0, r) \ . \tag{2.36}$$

Denote the added number of slices $M = P - j$, then the corresponding propagator is

$$R_{jP}(r_0, r) = e^{\Delta U + \mu \Delta\tau M} \prod_{\nu=1}^{M} \rho_0(r_{\nu-1}, r_{\nu}; \Delta\tau) \ . \tag{2.37}$$

Then $g(r, \Delta\tau P)$, as first appeared in Eq. (2.31), can be expressed as follows,

$$\begin{aligned} g(r, \beta) &= \int D\{\xi\} \mathcal{D}_{\xi_0}(r_0, j) R_{jP}(r_0, r) \\ &= \frac{1}{\bar{M}} \sum_{M} \int D\{\xi\} \mathcal{D}_{\xi_0}(r_0, j) R_{jP}(r_0, r) \delta_{M}^{(\bar{M})} \ , \end{aligned} \tag{2.38}$$

where $\xi = (\xi_0, r_1, r_2, ...r_{M-1})$. $\delta_{M}^{(\bar{M})}$ requests that $M < \bar{M}$, which allows one to sample the rest of the time slices only from the adjacent time slices. One additional question is that r is still a continuous variable while we would like it to be granulated into a set of predefined points $\{r_p\}$. Thus we can formally rewrite Eq. (2.38),

$$\begin{aligned} g(r_p, \beta) = &\sum_{M} \int d\xi_0 dr_0 \mathcal{D}_{\xi_0}(r_0, j) \delta_{M}^{(\bar{M})} \\ &\times \int dr \rho_0(r_0, r; \Delta\tau M) \delta_{r}^{(V_p)} \\ &\times \int dr_1 \dots dr_{M-1} \frac{\prod_{\nu=1}^{M} \rho_0(r_{\nu-1}, r_{\nu}; \Delta\tau)}{\rho_0(r_0, r_p; \Delta\tau M)} Q \ . \end{aligned} \tag{2.39}$$

The kernel Q in Eq. (2.39) can be easily derived from the construction,

$$Q = (\bar{M}V_p)^{-1}\frac{\rho_0(r_0, r_p; \Delta\tau M)}{\rho_0(r_0, r; \Delta\tau M)}e^{\Delta U+\mu\Delta\tau M} \ . \tag{2.40}$$

The method of sampling Q is also defined clearly in Eq. (2.39). The second line in Eq. (2.39) indicates that r is sampled according to a Gaussian distribution with mean r_0, and determine r_p according to the value of r sampled. The third line explains how the intermediate beads are sampled. The reasoning of this sampling method is explained in Ref. [138] and will not be further elaborated here. Taking the same analogy to Eq. (2.33) - (2.35), the reformulated MC sampling of $g(r, \Delta\tau j)$ is given as

$$\frac{CVP}{Z_W}g(r_p, \beta) = \left\langle \delta^{(G)}\delta_M^{(\bar{M})}\delta_r^{(V_p)}Q \right\rangle_{\text{MC}} \ . \tag{2.41}$$

Given the relationship with the reduced one-body density matrix $\bar{G}(r_p, \beta)$,

$$\bar{G}(r_p, \beta) = \frac{g(r_p, \beta)}{Z} \ . \tag{2.42}$$

Combined with Eq. (2.33), the reduce one-body density matrix can be sampled with the following method,

$$\bar{G}(r_p, \beta) = \frac{1}{CVP}\frac{\left\langle \delta^{(G)}\delta_M^{(\bar{M})}\delta_r^{(V_p)}Q \right\rangle_{\text{MC}}}{\left\langle \delta^{(Z)} \right\rangle_{\text{MC}}} \ . \tag{2.43}$$

Due to convenience in parameter setting, let us redefine

$$C = \frac{C_0}{VP\bar{M}} \ , \tag{2.44}$$

where $C_0 \sim O(1)$ to optimize the acceptance ratio. We also redefine $Q = \tilde{Q}(\bar{M}V_p)^{-1}$, then

$$\bar{G}(r_p, \beta) = \frac{1}{C_0 V_p}\frac{\left\langle \delta^{(G)}\delta_M^{(\bar{M})}\delta_r^{(V_p)}\tilde{Q} \right\rangle_{\text{MC}}}{\left\langle \delta^{(Z)} \right\rangle_{\text{MC}}} \ . \tag{2.45}$$

Eq. (2.45) can be numerically simulated directly. The way the numerator is sampled is elaborated in between Eq. (2.40) and Eq. (2.41). The denominator is the number of diagonal configurations.

Chapter 3

Universal Scaling of the Lieb-Liniger Gas

In this chapter, we study the density and momentum distribution functions of the Lieb-Liniger model in a harmonic trap at zero and finite temperature. We focus on the scaling properties of those quantities and in the high momentum tails of the momentum distribution function. The latter have remained elusive to quantum Monte Carlo simulations so far. The weight of the high momentum tail, which is known as Tan's contact, is a quantity that plays a central role in a set of universal thermodynamic relations known as Tan's relations [143–145]. The Tan's contact has been measured in experiments with 3D Bose-Einstein condensates [146].

In order to obtain accurate results for all the quantities above, for arbitrary interaction strengths, we use path integral quantum Monte Carlo [139] for continuous systems with worm updates [137, 138]. We also obtain results in the Tonks-Girardeau limit using the Bose-Fermi mapping in the lattice and working at very low fillings [44–46]. For completeness, in all cases, we also discuss the behavior of the quantities of interest in homogeneous systems, which helps motivate the scaling relations for the trapped systems.

This chapter is organized as follows. In Sec. 3.1, we introduce the Hamiltonian and numerical approaches used. We also discuss some of the checks done to test the accuracy of our calculations. In Secs. 3.2 and 3.3, we report a detailed study of density and momentum distribution functions, as well as one-particle correlations, of the Lieb-Liniger systems at zero and finite temperatures, respectively. In both sections, we discuss results for homogeneous and harmonically trapped systems.

3.1 Hamiltonian and Numerical Approaches

We consider 1D bosons with repulsive contact interactions in the presence of an external harmonic trap. The Hamiltonian can be written as

$$\mathcal{H} = \sum_j \left[-\frac{\hbar^2}{2m} \frac{\partial^2}{\partial x_j^2} + V(x_j) \right] + g_{1\mathrm{D}} \sum_{j<l} \delta(x_j - x_l) \ , \tag{3.1}$$

where m is the mass of the bosons, $g_{1\mathrm{D}}$ is the strength of the contact interaction, $V(x_j) = m\omega^2 x_j^2/2$, and ω is the frequency of the harmonic trap. The strength of the effective 1D contact interaction is usually written as $g_{1\mathrm{D}} = -2\hbar^2/ma_{1\mathrm{D}}$, where $a_{1\mathrm{D}} = -a_\perp(a_\perp/a_s - C)$ is the 1D scattering length, a_s is the 3D s-wave scattering length, $a_\perp$ is the length of the transverse confinement, and $C = 1.0326$ [8]. Another parameter frequently used to describe the interaction strength is $c = mg_{1\mathrm{D}}/\hbar^2$. In the absence of the trap, this Hamiltonian reduces to the Lieb-Liniger model, which essentially has only one tunable parameter $\gamma = c/\rho$, where ρ is the density. To relate γ with the effective scattering length $a_{1\mathrm{D}}$,

$$\gamma = \frac{2}{\rho a_{1\mathrm{D}}} \ . \tag{3.2}$$

Here, in order to simulate the Hamiltonian above in the continuum, we use a path integral quantum Monte Carlo method with worm updates (from now on referred to as the worm algorithm) [137, 138]. The configuration space in our simulation is built with discrete imaginary time world lines in a continuous position space. The worm algorithm operates both with diagonal and off-diagonal configurations by introducing one additional open world line in the configuration space. This makes it very efficient in simulating both diagonal observables (such as the energy, the density distribution, and the superfluid fraction) and off-diagonal observables (such as two-point one-particle correlation functions). In our calculations, the action for contact interactions is approximated by the pair-product action, see Chapter 2, and we always work in the grand canonical ensemble.

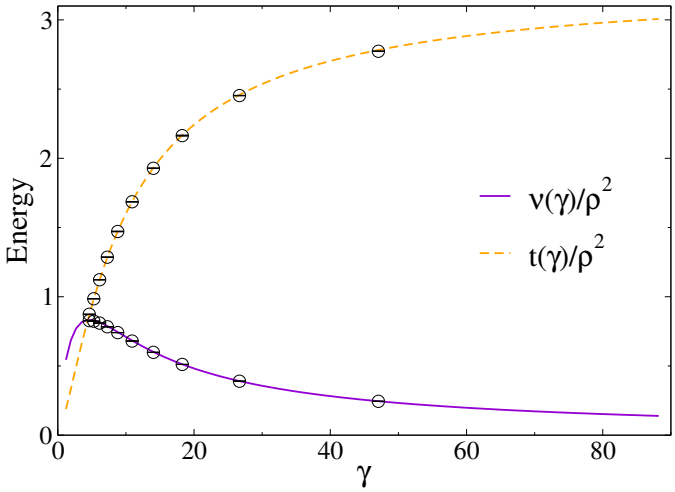

Figure 3.1: Worm algorithm results for the ground-state kinetic and interaction energies (see text) of the Lieb-Liniger model (circles) compared with the exact analytical results (lines) [5]. The statistical errors (shown within the circles) can be seen to be much smaller than the circle sizes. The average number of particles in the system is $N_b \approx 20$.

3.1.1 Energies

In Fig. 3.1, we compare results for the ground state kinetic $[K(\gamma) = \hbar^2 t(\gamma)/2m]$ and interaction $[U(\gamma) = \hbar^2 \nu(\gamma)/2m]$ energies from the worm algorithm simulations (for a finite system with $N_b \approx 20$ bosons) with the exact analytic results in the thermodynamic limit [5]. Average energies are obtained using the thermodynamic estimators reported in Chapter 2 (see also Ref. [139]). Figure 3.1 shows that, already for systems with $N_b \approx 20$, finite-size effects are negligible, and that the worm algorithm provides a very accurate estimation of observables in diagonal configuration space.

3.1.2 Luttinger Liquid Parameters

The ground state and low energy behavior of the Lieb-Liniger model is well described by Luttinger liquid theory. The Luttinger liquid Hamiltonian can be written as,

$$\mathcal{H}_{\rm LL} = \frac{\hbar}{2\pi} \int_0^L dx \left[v_N [\partial_x \hat{\theta}(x)] + v_J [\partial_x \hat{\phi}(x)] \right] , \tag{3.3}$$

It is composed of two bosonic fields, $\hat{\theta}(x)$ and $\hat{\phi}(x)$, representing density and phase oscillations. The two velocities v_N and v_J, density and phase stiffness [134], are determined by the parameters of the original microscopic model. The Luttinger parameter $K = \sqrt{v_J/v_N}$, controls the long-range behavior of correlation functions. The sound velocity $v = \sqrt{v_J v_N}$ indicates the propagation speed of density disturbance [2]. As already pointed out in Lieb's original paper [6], the sound velocity can be connected to the ground state energy by the following formula,

$$v = \frac{\hbar\rho}{m}\sqrt{3e(\gamma) - 2\gamma e'(\gamma) + \frac{\gamma^2}{2}e''(\gamma)}\ . \tag{3.4}$$

The Luttinger parameter K are related to v with the exact relation $K = \pi\hbar\rho/(mv)$, thus one can also obtain an exact expression for K,

$$K = \frac{\pi}{\sqrt{3e(\gamma) - 2\gamma e'(\gamma) + \frac{\gamma^2}{2}e''(\gamma)}}\ . \tag{3.5}$$

In addition, as pointed out in Ref. [5], the Bogoliubov approximation for the ground state energy produces very accurate expression for $\gamma \lesssim 10$,

$$K = \frac{\pi}{\sqrt{\gamma}}\left(1 - \frac{\sqrt{\gamma}}{2\pi}\right)^{-1/2} \quad \text{for} \quad \gamma \lesssim 10\ . \tag{3.6}$$

For $\gamma \gg 1$, one can obtain K from a strong coupling expansion of the energy [147].

$$\begin{aligned} K = 1 &+ \frac{4}{\gamma} + \frac{4}{\gamma^2} - \frac{16\pi^2}{3\gamma^3} + \frac{32\pi^2}{3\gamma^4} + \frac{64\pi^2(-5+3\pi^2)}{15\gamma^5} \\ &- \frac{32\pi^2(-20+39\pi^2)}{15\gamma^6} - \frac{256\pi^2(35-147\pi^2+15\pi^4)}{105\gamma^7} \\ &+ \frac{128\pi^2(140-1050\pi^2+341\pi^4)}{105\gamma^8} + \mathcal{O}(\gamma^{-9})\ . \end{aligned} \tag{3.7}$$

Fig. 3.2 shows a comparison of K from Eq. (3.6) and Eq. (3.7) to the PIMC simulations using the bipartite fluctuations $\mathcal{F}$ defined in Sec. 4.1.2.2.

The other quantity of interest is the superfluid fraction ρ_s/ρ. In Ref. [148], the superfluid fraction was proved to be a pure scaling function of LT/v_J under the

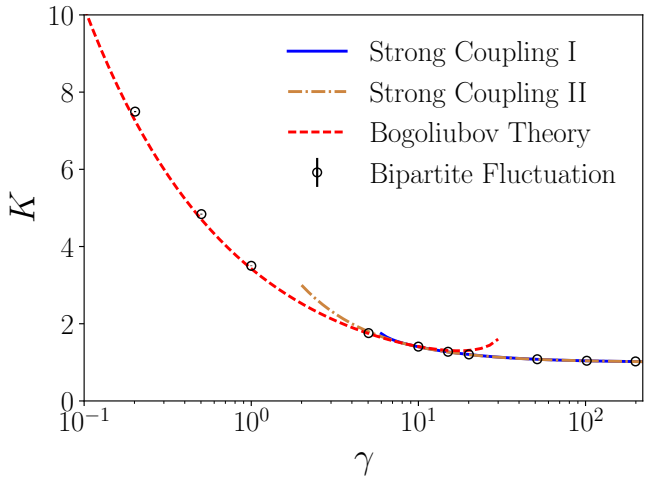

Figure 3.2: Luttinger liquid parameter K for the Lieb-Liniger model as a function of γ obtained from PIMC simulation of bipartite fluctuations $\mathcal{F}$ detailed in Sec. 4.1.2.2. The simulations are done with fixed number of particles $N = 60$. The red dashed line comes from Bogoliubov approximation. The solid and dash-dotted lines are results from strong-coupling expansions to different orders, $\mathcal{O}(\gamma^{-2})$ and $\mathcal{O}(\gamma^{-9})$ respectively.

Luttinger liquid approximation,

$$\frac{\rho_s}{\rho} = 1 - \frac{\pi v_J}{LT}\left|\frac{\theta_3''(0, e^{-2\pi v_J/(LT)})}{\theta_3(0, e^{-2\pi v_J/(LT)})}\right|, \tag{3.8}$$

where $\theta_3(z, q)$ is the Jacoby Theta function of the third kind, and we define $\theta_3''(z, q) = \partial_z^2 \theta_3(z, q)$. Due to the Galilean invariance of the model, $v_J = v_F$, where v_F is the Fermi velocity,

$$v_F = \frac{\hbar\pi\rho}{m}\,. \tag{3.9}$$

Fig. 3.3 shows the collapse of our numerical data for different γ's to the Luttinger liquid prediction in Eq. (3.8). It also makes apparent the transition from pure superfluid to a classical atomic gas when T is increased.

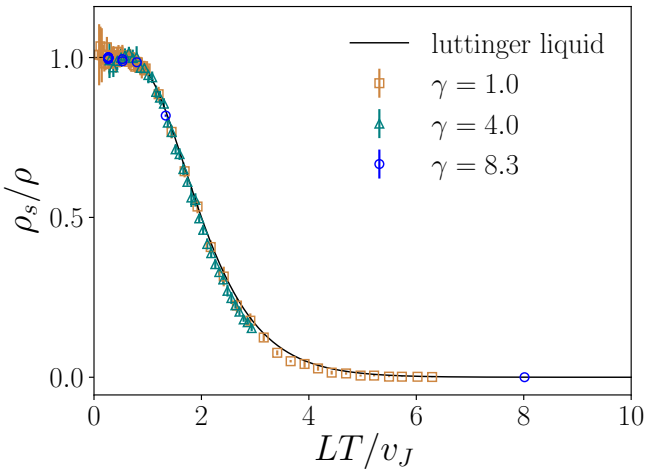

Figure 3.3: The superfluid fraction as a function of the dimensionless scaling variable LT/v_J. The solid line is the scaling function obtained from the Luttinger liquid approximation.

3.1.3 One-body Correlations

The observables on which we focus next, the density and momentum distribution functions, are calculated from the one-particle density matrix

$$g(x, y) = \langle \Psi^\dagger(x)\Psi(y) \rangle \ , \tag{3.10}$$

where $\Psi^\dagger(x)$ [$\Psi(x)$] is the bosonic field creation (annihilation) operator at position x. $g(x, y)$ is an example of an off-diagonal observable that can be efficiently calculated using the worm algorithm.

For improved statistics, in our calculations, we average $g(x, y)$ over all possible translations ($0 < x, y < L$) so that it becomes a function of $r = |x - y|$. For $r > 0$,

$$g(r) = \frac{1}{2L}\left[\int_0^L g(x, x + r)dx + \int_0^L g(y + r, y)dy\right] \ , \tag{3.11}$$

while, for $r = 0$,

$$g(0) = \frac{1}{L}\int_0^L g(x, x)dx \ . \tag{3.12}$$

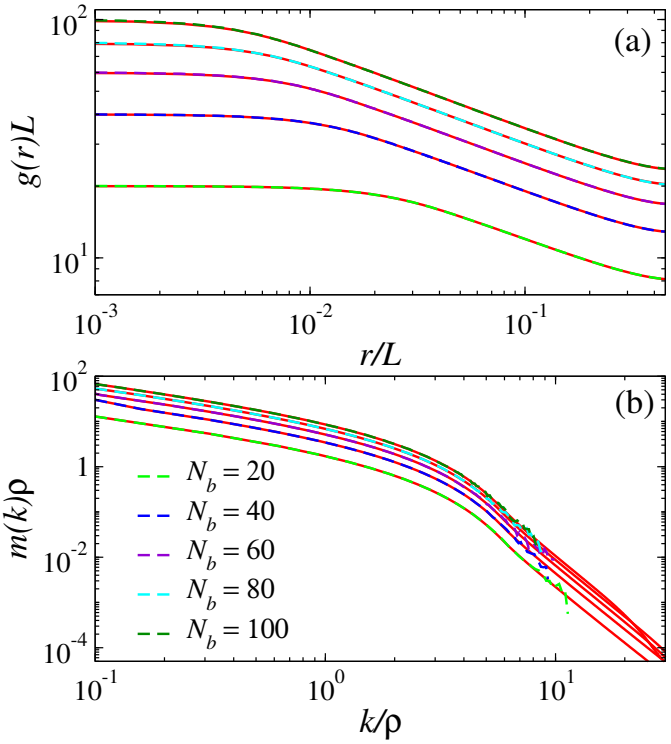

Figure 3.4: (a) Ground-state one-particle correlations and (b) momentum distribution functions of bosons for $\gamma = 8.33$. Results are reported for systems with the same density but different average number of particles. Dashed lines are the results obtained using the worm algorithm and solid lines the results obtained in numerical calculations via algebraic Bethe ansatz [22].

The Fourier transform of $g(r)$ gives the momentum distribution function

$$\begin{aligned} m(k) &\equiv \frac{1}{2\pi}\int_0^L dx \int_0^L dy\, e^{ik(x-y)} g(x,y) \\ &= \frac{L}{2\pi}\int_0^L \cos(kr) g(r) dr \ . \end{aligned} \tag{3.13}$$

In Fig. 3.4, we show results for $g(r)$ [Fig. 3.4(a)] and $m(k)$ [Fig. 3.4(b)] for the ground state of systems with $\gamma = 8.33$, the same density, and different average number of particles, and compare them with numerical results obtained via algebraic Bethe ansatz [22]. The results for $g(r)$ in both approaches are essentially indistinguishable in Fig. 3.4(a). The same is true for $m(k)$ in Fig. 3.4(b), except at the highest momenta. In the latter regime, $m(k)$ becomes very small and the statistical errors in the quantum Monte Carlo simulation become of the same order.

This is why it is a challenge to study the asymptotic behavior of $m(k)$ at high momenta. Experiments will suffer from exactly the same limitation as $m(k)$ will at some point become of the same order of the experimental noise. It is worthwhile to mention there exist methods to map out momentum distribution functions for all momenta in the unitary limit, see Ref. [149, 150] for further details. The results in Fig. 3.4 make apparent the accuracy of the worm algorithm for computing off-diagonal one-particle observables. Once translational invariance is broken, no analytical solution is available. To gauge the accuracy of the worm algorithm in that case we focus on the Tonks-Girardeau limit.

In that limit, the one-particle density matrix (and, hence, the momentum distribution function) in a lattice can be calculated exactly via the Jordan-Wigner transformation and making use of properties of Slater determinants, both at zero [44, 45] and finite temperature [46]. As we explain below, using this approach in the low-density limit in the lattice, one can efficiently compute one-particle properties in the continuum [45].

The Tonks-Girardeau Hamiltonian in the lattice can be written as

$$\mathcal{H}_{\mathrm{TG}} = -J\sum_i (b_i^\dagger b_{i+1} + \mathrm{H.c.}) + V_2 \sum_i i^2 n_i \ , \tag{3.14}$$

where $b_i^\dagger$ (b_i) is the creation (annihilation) operator of a hard-core boson at site i, $n_i = b_i^\dagger b_i$ is the site occupation operator, J is the hopping amplitude, and V_2 sets the strength of the harmonic trap. This Hamiltonian is obtained from the Bose-Hubbard Hamiltonian by taking the limit in which the onsite repulsion $U \to \infty$ [2].

The hard-core boson creation and annihilation operators satisfy standard bosonic commutation relations with the constraint $(b_i^\dagger)^2 = b_i^2 = 0$. Mapping the Tonks-Girardeau Hamiltonian (3.14) onto a spin-1/2 chain [151, 152], and then the spin-1/2 chain onto noninteracting fermions in 1D via the Jordan-Wigner transition, one gets

$$\mathcal{H}_F = -J\sum_i (f_i^\dagger f_{i+1} + \mathrm{H.c.}) + V_2 \sum_i i^2 n_i^f \ , \tag{3.15}$$

where $f_i^\dagger$ (f_i) is the creation (annihilation) operator of a spinless fermion at site i, and $n_i^f = f_i^\dagger f_i$ is the fermionic site occupation operator. The fermionic Hamiltonian (3.15) can be straightforwardly diagonalized. One-particle bosonic correlations can

then be obtained using properties of Slater determinants as discussed in Refs. [44–46]. We should stress that, within this lattice approach, the ground-state calculations are done in the canonical ensemble [44, 45], while finite-temperature ones are done in the grand-canonical one [46].

To establish the relation between the parameters in the lattice Hamiltonian and in the continuum, we notice that the single-particle energy spectrum of the spinless fermion model without a trap is $\varepsilon_k = -2J\cos(ka)$, where a is the lattice spacing. In the zero-density limit, the Fermi momentum $k_F \to 0$. As a result, the energy spectrum becomes quadratic in k as, up to a constant, we can write $\varepsilon_k = Ja^2k^2$. Thus, in the zero-density limit, the lattice model reduces to a continuum model with the effective mass given by $m = \hbar^2/(2Ja^2)$. In this limit, according to Eq. (3.14), the external trapping potential is

$$V(x) = V_2 \times (x/a)^2 \, . \tag{3.16}$$

Compared with a harmonic trap in continuum, where $V(x) = m\omega^2/2$, the trapping frequency is then given by $\omega = 2\sqrt{JV_2}/\hbar$, and so the harmonic oscillator length $a_{\rm HO} = \sqrt{\hbar/m\omega}$ can be written as $a_{\rm HO}/a = (J/V_2)^{1/4}$. Finally, in finite-temperature calculations in the lattice, the lattice temperature $T_{\rm latt}$ is usually defined as $JT_{\rm latt} = k_BT$, i.e., it is given in units of J. The temperature in units of trapping frequency in the continuum is related to the lattice temperature by the expression $k_BT/\hbar\omega = T_{\rm latt}\sqrt{J/V_2}/2$[1]. In the lattice, the momentum distribution function is defined as the discrete Fourier transform of the one-particle density matrix

$$m_k = \frac{1}{N}\sum_{jl} e^{ika(j-l)} b_i^\dagger b_j \, , \tag{3.17}$$

where N is the number of lattice sites. By comparing Eq. (3.13) and Eq. (3.17), one can see that the momentum distribution function in the continuum and in

[1] When one is applying the zero-density limit of the lattice model to mimic a continuous system without an external lattice potential. The lattice spacing a plays a role close to l_0 discussed in Appendix B. In this case, the tunneling $J = \hbar^2/(2ma^2)$ (according to $m = \hbar^2/(2Ja^2)$ detailed in Sec. 3.1.3) is the energy unit ϵ_0. This way, we are able to connect the lattice model to experimental results.

On the other hand, if the lattice model is applied to study a continuous system with underlying periodic lattice potential. Then a is related to the periodicity λ of the lattice. Then the tunneling parameter J in this case can be estimated from, e.g., Wannier functions.

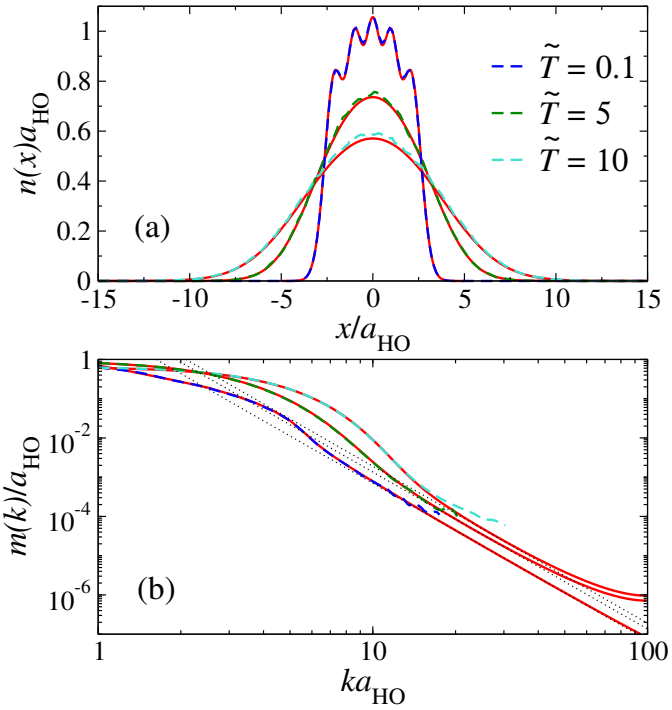

Figure 3.5: Density profiles (a) and momentum distribution functions (b) of the Tonks-Girardeau gas as calculated using the lattice approach (red solid lines) and in the continuum using the worm algorithm (dashed lines). The average number of particles is 5. Results are presented for different temperatures: $\tilde{T} \equiv k_B T/\hbar\omega$=0.1, 5, 10. Thin dotted lines indicate the k^{-4} asymptotic behavior of the momentum tails. The statistical errors in the worm algorithm are of the order of the fluctuations seen in the results. They are not reported for clarity.

the lattice are related by the expression $m_k = m(k)\delta k$, where $\delta k = 2\pi/L$ (with $L = Na$) is the discretization of k in the lattice model.

With the relations discussed so far at hand, we are ready to compare results for density and momentum distribution functions in the continuum and the lattice, which, as mentioned before, help us gauge the accuracy of the worm algorithm for diagonal and off-diagonal observables in the absence of translational invariance. In order to approach the Tonks-Girardeau limit in the continuum model, we choose a very small value of the 1D scattering length $a_{1D}/a_{HO} = 5.66 \times 10^{-3}$.

The scaled density $[n(x) = g(x, x)]$ and momentum distribution functions obtained in the lattice and the continuum are shown in Fig. 3.5 at various temperatures ($\tilde{T} \equiv k_B T/\hbar\omega$). The agreement between the results of both approaches is almost perfect at the lowest temperatures $\tilde{T} = 0.1$ and 5 (for $\tilde{T} = 0.1$ the system is essen-

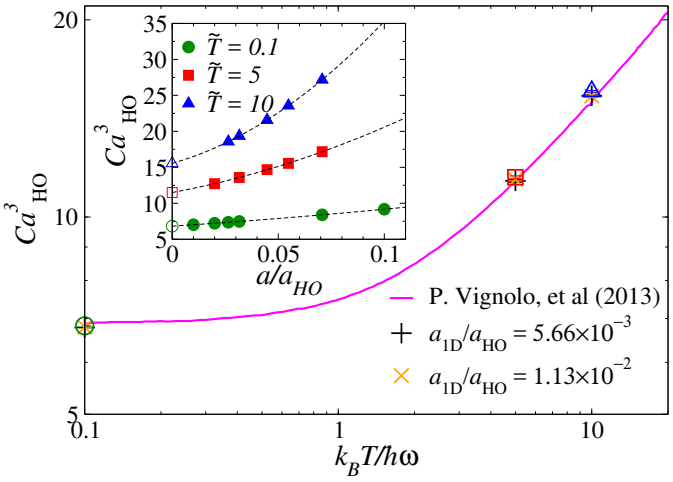

Figure 3.6: Tan's contact for the trapped systems in Fig. 3.5 compared with results in Ref. [32]. The contact from the worm algorithm simulation is obtained through the interaction energy using the expression $\mathcal{C}a^3_{\rm HO} = -a^3_{\rm HO}N_b\nu(\gamma)/(\pi a_{\rm 1D})$ [derived from Eq. (3.18)], where $\nu(\gamma)$ is the average interaction energy per particle [in units of $\hbar^2/(2m)$]. We calculated $\mathcal{C}a^3_{\rm HO}$ for two small values of $a_{\rm 1D}$ obtaining results that agree with the ones in Ref. [32]. The contact from the lattice calculation is obtained via a linear fit of the high momentum tails, and then extrapolated to the zero density limit via a quadratic fit to obtain the result for zero $a/a_{\rm HO}$ (see inset).

tially in the ground state). As the temperature increases, lattice effects become important and lead to visible differences when the lattice results are compared with the results in the continuum [see the discussion after Eq. (3.18)]. In the momentum distribution function [Fig. 3.5(b)], the worm algorithm at $\tilde{T} = 0.1$ and 5 already captures part of the k^{-4} momentum tails. For higher temperatures, such as $\tilde{T} = 10$ in Fig. 3.5(b), the k^{-4} regime is not visible in the worm algorithm calculation. This is understandable because, as the lattice calculation clearly shows, the k^{-4} tail starts at higher values of the scaled momentum [smaller values of the scaled $m(k)$] as the temperature increases.

3.1.4 Tan's Contact

We have studied the weight $\mathcal{C}$ (Tan's contact) of the k^{-4} momentum tails [$m(k) = \mathcal{C}\,k^{-4}$] using both methods. In the lattice approach, $\mathcal{C}$ is computed directly via linear fits of the momentum tails. In the worm algorithm calculation, the contact

$\mathcal{C}$ is calculated via the interaction energy estimator, using the relation [32]

$$\mathcal{C} = \frac{g_{1D} m^2}{\pi \hbar^4} \langle \mathcal{H}_{\text{int}} \rangle \ , \tag{3.18}$$

where $\mathcal{H}_{\text{int}}$ is the interaction part of Eq. (3.1). The results are shown in Fig. 3.6. The values of the contact obtained using the worm algorithm for two small values of the scattering length are consistent with the results in Ref. [32]. This indicates that such small values of a_{1D} allow us to obtain results in the Tonks-Girardeau limit. Using the lattice approach, the contact in the continuum is calculated by taking the low density limit by means of a quadratic fit (see the inset in Fig. 3.6). The results of such a fitting procedure are in agreement with those obtained using the worm algorithm and Ref. [32], as shown in the main panel in Fig. 3.6. Note that for the ground state calculation, lattice effects are negligible at the lowest densities studied.

3.2 Ground-State

3.2.1 Homogeneous Systems

3.2.1.1 Tonks-Girardeau Limit

In the Tonks-Girardeau limit, Tan's contact allows for a simple analytic expression that unveils how to scale the momentum distribution function (one-particle correlations) to achieve data collapse for high momenta (small distances). As indicated in Eq. (3.18), $\mathcal{C}$ is linearly related to the interaction energy. In the language of Ref. [5],

$$\mathcal{C} = \frac{N_b \rho \gamma \nu(\gamma)}{2\pi} \ , \tag{3.19}$$

where $\nu(\gamma) = \rho^2 \gamma de(\gamma)/d\gamma$, and $e(\gamma)$ is a monotonically increasing function of γ that saturates at $\pi^2/3$ when $\gamma \to \infty$ (for its definition, see Ref. [5]). For large values of γ, ν has the following asymptotic form: $\nu(\gamma) = 4\rho^2 e(\gamma)/(\gamma + 2)$. Thus, in the limit $\gamma \to \infty$, Tan's contact reduces to $\mathcal{C} = 2\pi L \rho^4/3$. Hence, $\tilde{\mathcal{C}} \equiv \mathcal{C}/L\rho^4 = 2\pi/3$. This means that if one plots $m(k)/L$ vs k/ρ, no matter the number of particles and the system size, the curves must collapse for high values of k. From Eq. (3.13), it then follows that the universal behavior of $m(k)$ for high values of k implies that,

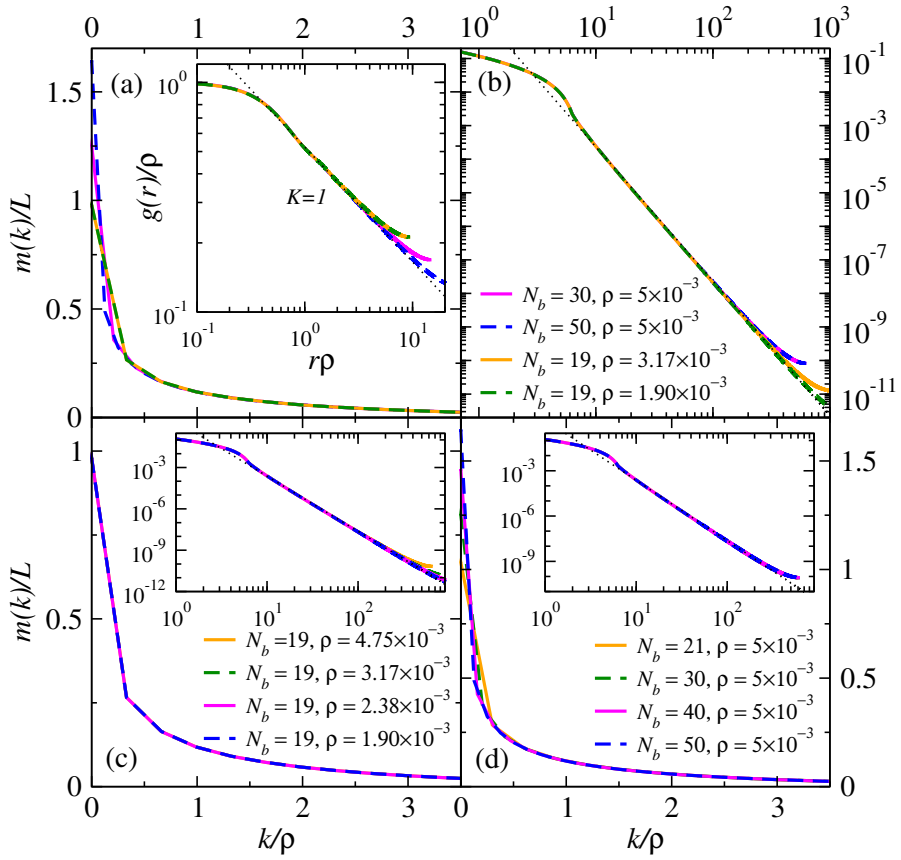

Figure 3.7: Scaled momentum distribution functions $m(k)/L$ in the Tonks-Girardeau limit as a function of the scaled momentum k/ρ. (a) Systems with different number of particles and densities, (b) same as (a) but in log-log scale, (c) systems with the same number of particles and different densities, (d) systems with different number of particles and the same density. Insets: (a) scaled average one-particle density matrix, (c) and (d) same as main panels but in log-log scale. Thin dotted lines indicate the asymptotic behavior discussed in the text. Here, and throughout this chapter, ρ in the lattice is given in units of the inverse lattice spacing a.

if one plots $g(r)/\rho$ vs ρr, the curves must collapse for small values of r. Results for $m(k)$ and $g(r)$, obtained using the *lattice approach* discussed in the previous section, are reported in Fig. 3.7

In Fig. 3.7(a), we plot $m(k)/L$ vs k/ρ for systems with different number of particles and densities. Figure 3.7(b) reports the same results but in a log-log scale. Both panels make apparent that, for intermediate and high momentum, all curves collapse onto a universal result. In the $k \to 0$ limit, $m(k=0)/L = m_{k=0} \propto \sqrt{N_b}$ because of the existence of quasi-long-range order [2] and, as such, only curves

with the same number of particles can collapse for low values of k. This can be better seen in Fig. 3.7(c), where, for the same number of particles, all momentum distribution curves collapse for all momenta. Differences can only be seen at the highest momenta because of finite-density effects in the lattice. On the other hand, as shown in Fig. 3.7(d), plotting results for the same density and different number of particles, again produce curves that collapse at intermediate and high momenta but differ for the lowest values of k. For systems with larger number of particles, the universal behavior can be seen to start at lower values of k. Consequently, irrespectively of the density in thermodynamically large system sizes, one expects the momentum distribution functions to become universal starting at infinitesimal values of k.

In the inset in Fig. 3.7(a), we plot results for $g(r)/\rho$ vs ρr for systems with different number of particles and densities. The plots can be seen collapse onto universal results, in which, at long distance, $g(r) \propto 1/\sqrt{r}$ [2]. The latter behavior can be understood within the bosonization approach [134], which predicts that $g(r) \propto 1/r^{1/(2K)}$ at long distances. In the Tonks-Girardeau limit, $K = 1$.

3.2.1.2 Finite Interaction Strength

For finite interaction strengths, particles can penetrate through one another and the systems tend to have lower kinetic energies (less particles in the high momentum tails) than in the Tonks-Girardeau limit. As a result, Tan's contact decreases with decreasing γ. From Eq. (3.19), $\mathcal{C}$ can be written as $\mathcal{C} = L\gamma^2 e'(\gamma)\rho^4/(2\pi)$. The scaled contact, $\tilde{\mathcal{C}} \equiv \mathcal{C}/L\rho^4 = \gamma^2 e'(\gamma)/(2\pi)$, is now *only* a function of γ. From this result it follows that, so long as γ is kept constant (no matter the system size and the number of particles in the system), the curves for $m(k)/L$ vs k/ρ will be universal for large values of k. This is the same scaling discussed for the Tonks-Girardeau regime, in which γ is constant ($\gamma = \infty$). Similarly, the curves for $g(r)/\rho$ vs ρr must be universal at short distances. Results for $m(k)$ and $g(r)$, obtained using the *worm algorithm*, are reported in Fig. 3.8.

In the main panels in Fig. 3.8, we plot the momentum distribution for $\gamma = 8.3$ [Fig. 3.8(a) and 3.8(b)] and for $\gamma = 1.0$ [Fig. 3.8(c) and 3.8(d)], in systems with different densities and average number of particles. Consistent with the previous discussion, the momentum distributions collapse for intermediate and high momentum. More importantly for experiments, with decreasing γ, the onset of the

k^{-4} behavior becomes less sharp (see also Fig. 3.7, and Fig. 5 in Ref. [22]). This makes the experimental identification of the k^{-4} tails increasingly difficult as one departs from the Tonks-Girardeau limit.

As $k \to 0$, the collapse obtained for intermediate and high values of k breaks down because of quasi-long-rage order. For finite values of γ, more particles have low momenta than in the Tonks-Girardeau limit. In particular, within the bosonization approach, the zero momentum occupation is predicted to be $m(k=0)/L \propto N_b^{1-1/(2K)}$, with $K \geq 1$ [134]. The insets in Figs. 3.7(a) and 3.7(c)

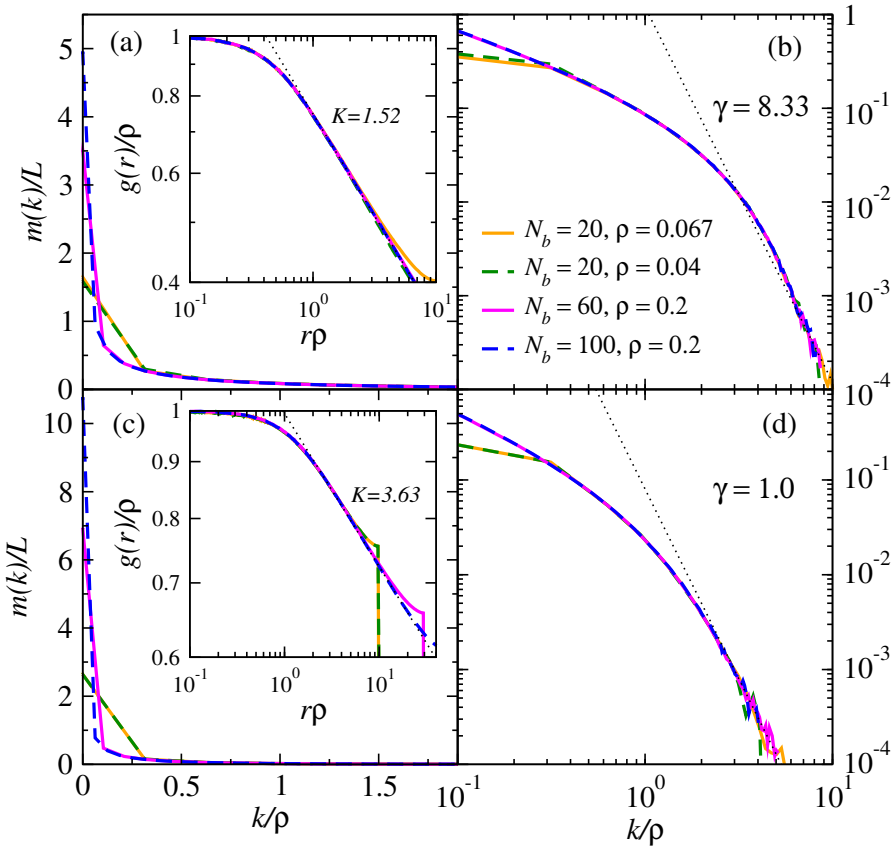

Figure 3.8: Scaled momentum distribution functions $m(k)/L$ vs the scaled momentum k/ρ for finite values of γ, plotted in [(a) and (c)] a linear scale and in [(b) and (d)] a log-log scale. Results are reported for [(a) and (b)] $\gamma = 8.33$ and [(c) and (d)] $\gamma = 1.0$. Insets: $g(r)/\rho$ vs ρr for the same systems as in the main panels. In all plots, thin dotted lines indicate the asymptotic behavior discussed in the text. A linear fit of the long distance behavior of the curves in the insets indicate that the Luttinger parameter is $K \approx 1.52$ for $\gamma = 8.33$ and $K \approx 3.63$ for $\gamma = 1.0$. Here, and throughout this chapter, ρ in the continuum is reported in an arbitrary unit.

depict $g(r)/\rho$ vs ρr for the same systems for which momentum distributions are shown in the main panels. The curves can be seen to collapse at short distances as expected. At long distances, $g(r) \propto 1/r^{1/(2K)}$ as predicted by the bosonization approach, with $K \approx 1.52$ for $\gamma = 8.3$ and $K \approx 3.63$ for $\gamma = 1.0$.

3.2.2 Trapped Systems

3.2.2.1 Tonks-Girardeau Limit

In order to generalize the scaling discussed in Sec. 3.2.1.1 to harmonically trapped systems, we need to find the replacement for ρ and L in the presence of a trap. Let us start by discussing how to scale density profiles in a harmonic trap. Since the density profiles of impenetrable bosons are the same as those of the non-interacting spinless fermions to which they can be mapped [2], we can focus on the noninteracting spinless fermions. The density profiles of the latter systems have been studied in detail in the past [153–155]. For a homogeneous Fermi system, the density is a linear function of the Fermi momentum k_F, $\rho = k_F/\pi$. The chemical potential μ in such systems is the Fermi energy $E_F = \hbar^2 k_F^2/(2m)$, so $\rho = \sqrt{2m\mu}/(\hbar\pi)$.

In a harmonic trap, the local chemical potential changes according to the relation

$$\mu(x) = \mu_0 - V(x) \ , \tag{3.20}$$

where μ_0 is the chemical potential at the center of the trap. Within the local density approximation (LDA), the density at each position in the trap is solely determined by the local chemical potential, through the relation obtained for homogeneous systems. Hence

$$n(x) = \frac{1}{\pi}\left(\tilde{\mu} - \frac{x^2}{a_{\rm HO}^4}\right)^{\frac{1}{2}} \ , \tag{3.21}$$

where $\tilde{\mu} = 2m\mu_0/\hbar^2$. The integral of Eq. (3.21) over the entire space is the number of particles N_b. It provides the following relation between $\tilde{\mu}$ and N_b, $\tilde{\mu} = 2N_b/a_{\rm HO}^2$. The density in the center of the trap is then $\tilde{\rho} = \sqrt{2N_b}/\pi a_{\rm HO}$, and the position in the trap at which the density vanishes is $\tilde{L} = \sqrt{2N_b}a_{\rm HO}$. Using these quantities, the density profile in the trap can be written as

$$n(x) = \tilde{\rho}\left[1 - \left(\frac{x}{\tilde{L}}\right)^2\right]^{\frac{1}{2}} \ . \tag{3.22}$$

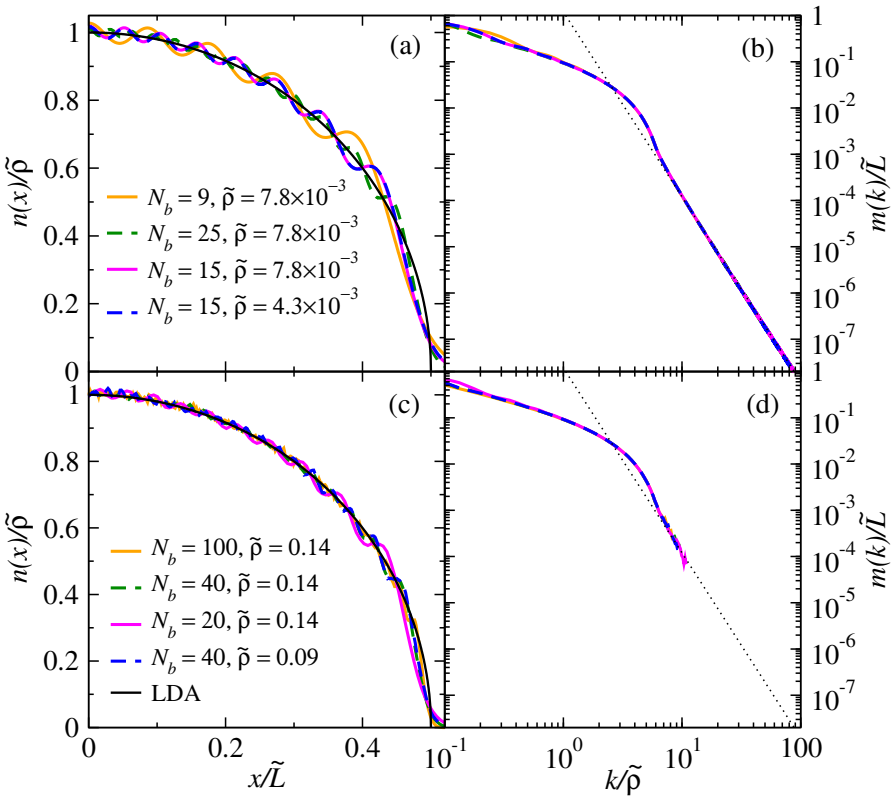

Figure 3.9: [(a) and (c)] Universal scaling of density and [(b) and (d)] momentum distribution functions in the Tonks-Girardeau limit. We report results from lattice calculations for [(a) and (b)] up to 25 bosons, and from the worm algorithm for [(c) and (d)] up to 100 bosons. In (a) and (c), we also report the LDA prediction for the density profiles. In (b) and (d), thin dotted line depict k^{-4} behavior.

By defining the scaled density $\tilde{n}(x) = n(x)/\tilde{\rho}$ and the scaled position $\tilde{x} = x/\tilde{L}$, one obtains

$$\tilde{n}(\tilde{x}) = (1 - \tilde{x}^2)^{\frac{1}{2}} \ . \tag{3.23}$$

Since the momentum distribution function at high momenta is determined by the average short-distance one-particle correlations, from the LDA and Eq. (3.23) one can advance that, using the scaling relations for homogeneous systems with $\rho \to \tilde{\rho}$ and $L \to \tilde{L}$, there will be data collapse for the momentum distribution function at high momenta.

In Fig. 3.9, we report results for density and momentum distribution functions in the Tonks-Girardeau limit obtained using the lattice approach and the worm algorithm. Given the constraint of very low site occupancies in the lattice, our

lattice calculations can only be done for significantly smaller numbers of particles than within the worm algorithm. The normalized density profiles in Figs. 3.9(a) and 3.9(c) exhibit the expected collapse, even for as few as nine bosons [Fig. 3.9(a)]. Data collapse can also be seen in the momentum distribution functions, except at very low momenta. The k^{-4} high momentum tails are apparent both in the lattice and worm algorithm results, though they are significantly better seen in the lattice calculation where much smaller values of $m(k)$, for higher values of k, can be computed.

We note that, using the relations we established in Sec. 3.1 between quantities in the continuum and in the lattice, one finds that the scaling properties of trapped systems in the continuum discussed so far are consistent with those discussed for lattice systems in Ref. [44, 45].

3.2.2.2 Finite Interaction Strength

For finite interaction strengths, the relation between the chemical potential and the density is not as simple as in the Tonks-Girardeau limit, where $\mu = \hbar^2\pi^2\rho^2/(2m)$. Instead, $\mu = \hbar^2\rho^2 f(\gamma)/(2m)$, where $f(\gamma) = 3e(\gamma) - \gamma e'(\gamma)$ [5]. This means that, using Eq. (3.20) and within LDA,

$$n^2(x) f[\gamma(x)] = n^2(0) f[\gamma(0)] - \frac{x^2}{a_{\rm HO}^4} \, . \tag{3.24}$$

The position in the trap at which the density vanishes is $L_{\rm LL} = \sqrt{f[\gamma(0)]}n(0)a_{\rm HO}^2$. Defining, as for the Tonks-Girardeau limit, $\tilde{n}(x) = n(x)/n(0)$ and $\tilde{x} = x/L_{\rm LL}$, and noticing that $\gamma(x) = mg/[\hbar^2 n(x)] = \gamma(0)/\tilde{n}(x)$, we obtain

$$\tilde{n}^2(\tilde{x}) f\left[\frac{\gamma(0)}{\tilde{n}(\tilde{x})}\right] = f[\gamma(0)](1-\tilde{x}^2) \, . \tag{3.25}$$

Equation (3.25) makes apparent that the scaled density profiles of systems with the same value of γ in the center of the trap must be identical. As in the Tonks-Girardeau limit, this result and the LDA allow one to advance a scaling collapse in the momentum distribution of trapped systems at high momenta [26].

However, the scaling above requires the knowledge of $n(0)$ and $L_{\rm LL}$, which can only be obtained numerically (or measured experimentally). We can predict another

universal way to scale densities and positions by noting that, from Eq. (3.25), it follows that

$$\tilde{n}(\tilde{x}) = h_0[1 - \tilde{x}^2, \gamma(0)] \, , \tag{3.26}$$

where $h_0(x, y)$ is an unknown function that can, in principle, be computed numerically (from now on we will call dummy functions of this kind as h_α, with $\alpha = 0, 1, \ldots$). Since $N_b = 2 \int_0^{L_{\rm LL}} n(x) dx = 2n^2(0) a_{\rm HO}^2 \sqrt{f[\gamma(0)]} \int_0^1 h_0[1 - \tilde{x}^2, \gamma(0)] d\tilde{x}$, we see that $n(0) = h_1[\gamma(0)] \sqrt{N_b}/a_{\rm HO} = h_2[\gamma(0)] \tilde{\rho}$, and $\tilde{\rho}$ is the density in the center of the trap in the Tonks-Girardeau limit. From this result for $n(0)$ it follows that $L_{\rm LL} = h_3[\gamma(0)] \tilde{L}$, where $\tilde{L}$ is the point at which the density vanishes in the Tonks-Girardeau limit. Hence, after fixing $\gamma(0)$, one can use exactly the same scaling for finite interaction strengths as the one used in the Tonks-Girardeau limit. We should stress that this is unique to bosons in the continuum. In the Bose-Hubbard model, one needs two parameters (the so-called characteristic density and the on-site interaction strength) to be kept fixed in order to be able to scale density profiles [156].

In Fig. 3.10, we show the scaled density [Figs. 3.10(a) and 3.10(c)] and momentum [Figs. 3.10(b) and 3.10(d)] profiles for systems with different numbers of particles, trapping frequencies, and 1D scattering lengths. Results are presented for $\gamma(0) \approx 9.3$ [Figs. 3.10(a) and 3.10(b)] and $\gamma(0) \approx 0.5$ [Figs. 3.10(c) and 3.10(d)]. The plots exhibit an excellent data collapse in the density profiles, and in the momentum distribution functions at intermediate and high momentum, as predicted by the analysis above. The high momentum k^{-4} tails are barely visible in Figs. 3.10(b) and 3.10(d). By comparing the results for $\gamma(0) \approx 9.3$ to those in the Tonks-Girardeau limit in Fig. 3.9, one can see that, even for that large value of $\gamma(0)$, the range and sharpness of the k^{-4} tails have decreased. This worsens as $\gamma(0)$ is further decreased and, as in the homogeneous case, poses an increasing experimental challenge for detecting the k^{-4} tails as one departs from the Tonks-Girardeau regime.

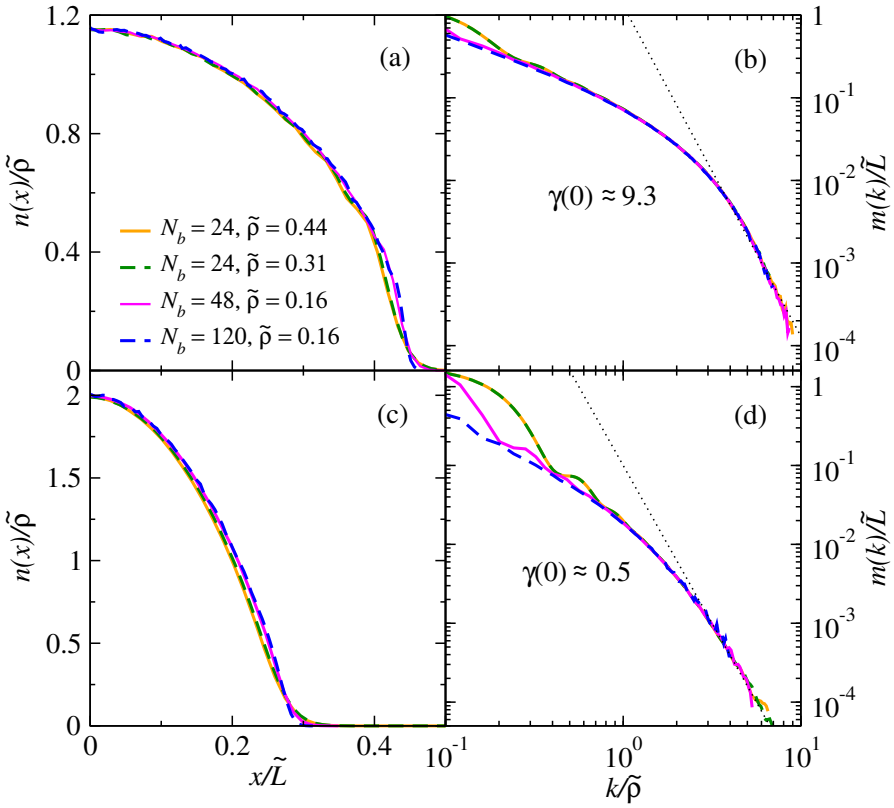

Figure 3.10: [(a) and (c)] Universal behavior of scaled density profiles and [(b) and (d)] momentum distribution functions for harmonically trapped systems with $\gamma(0) \approx 9.3$ in (a) and (b), and $\gamma(0) \approx 0.5$ in (c) and (d). In (b) and (d), thin dotted lines depict k^{-4} behavior.

3.3 Finite Temperature

3.3.1 Homogeneous Systems

3.3.1.1 Tonks-Girardeau Limit

At finite temperature, the long-distance behavior of one-particle correlation functions is qualitatively different from the one in the ground state. This because quasi-long-range order is destroyed by thermal fluctuations, i.e., the correlation functions decay exponentially with increasing distance [2]. As a result, the population of all momentum modes $m(k)/L$ becomes intensive. This means that, if the density and the temperature are kept constant, the momentum distribution function of systems with different number of particles should collapse (provided

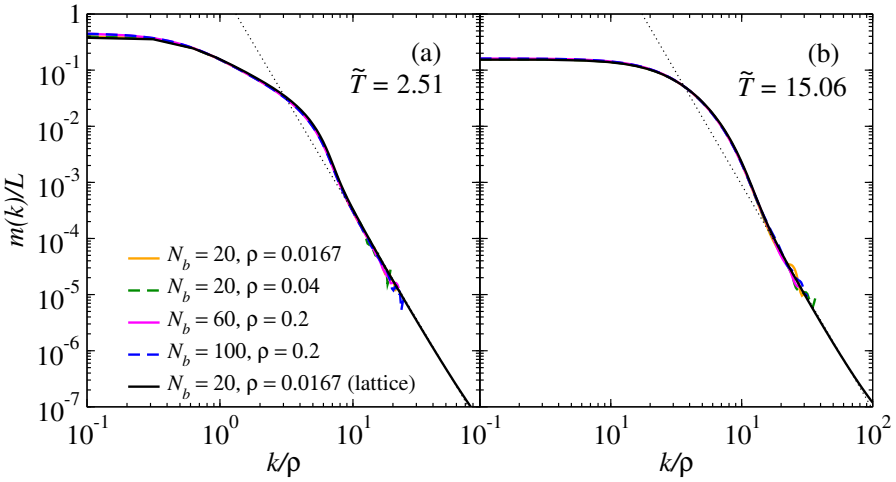

Figure 3.11: Finite temperature results for the scaled momentum distribution function of the homogeneous Tonks-Girardeau gas in systems with different average number of particles and densities. The scaled temperature in the plots is: (a) $\tilde{T} = 2.51$ and (b) $\tilde{T} = 15.06$. The black solid line in both panels was obtained using the lattice approach, while all other curves were obtained using the worm algorithm. Thin dotted lines depict k^{-4} behavior.

the system sizes are much larger than the correlation length). The curves with the same value of ρ in Figs. 3.11(a) and 3.11(b) show that this is indeed the case.

The question we would like to address here is how to scale the momentum profiles when the density and the temperature are changed in these systems. For that, as we did in Sec. 3.2.1.1, we look into Tan's contact in the limit $\gamma \to \infty$. As follows from the derivation in Appendix A, the Tan's contact takes the form [157–159]

$$\mathcal{C} = \frac{(2mk_BT)^2 L}{\hbar^4 2\pi} f_{1/2}\left(\frac{\mu}{k_BT}\right) f_{3/2}\left(\frac{\mu}{k_BT}\right) , \tag{3.27}$$

where $f_\nu(\cdot)$ is the Fermi-Dirac function (see Appendix A for its definition). From Eq. (A.7), one can see that $\mu/(k_BT)$ is a function of $2mk_BT/(\hbar^2\rho^2)$. Thus, one can define the scaled (dimensionless) temperature $\tilde{T} = 2mk_BT/(\hbar^2\rho^2)$. The scaled contact $\tilde{\mathcal{C}} = C/(L\rho^4)$ then has the form

$$\tilde{\mathcal{C}} = \frac{\tilde{T}^2}{2\pi} f_{1/2}\left(\frac{\mu}{k_BT}\right) f_{3/2}\left(\frac{\mu}{k_BT}\right) , \tag{3.28}$$

which is only a function of $\tilde{T}$. This means that, once $\tilde{T}$ is fixed, $m(k)/L$ vs k/ρ

is universal. The results in Figs. 3.11(a) and 3.11(b), in which we plot systems with different densities and temperatures but the same values of $\tilde{T}$, show that this is indeed the correct scaling. The k^{-4} momentum tails are clearly visible at high momenta. Two important features of those tails are apparent when comparing Figs. 3.11(a) and 3.11(b). The first one is that the weight of the tails (the contact) increases with increasing $\tilde{T}$, as discussed in Ref. [32]. The second one, probably more important for experiments, is that with increasing $\tilde{T}$ the values of $m(k)$ at which the tails start to develop become smaller. This means that the k^{-4} momentum tails are more difficult to observe experimentally as the temperature increases, despite the fact that Tan's contact becomes larger.

3.3.1.2 Finite Interaction Strength

For systems with a finite value of γ and finite temperatures one could advance, based on the results for the ground state (in which scaling collapse was found so long as γ was kept fixed) and on the results for finite temperature in the Tonks-Girardeau limit (in which scaling collapse was found so long as $\tilde{T}$ was kept fixed), that scaling collapse requires us to keep γ and $\tilde{T}$ constant. The results reported in Fig. 3.12 for a finite value of $\gamma = 8.33$, which parallel the results in the Tonks-Girardeau

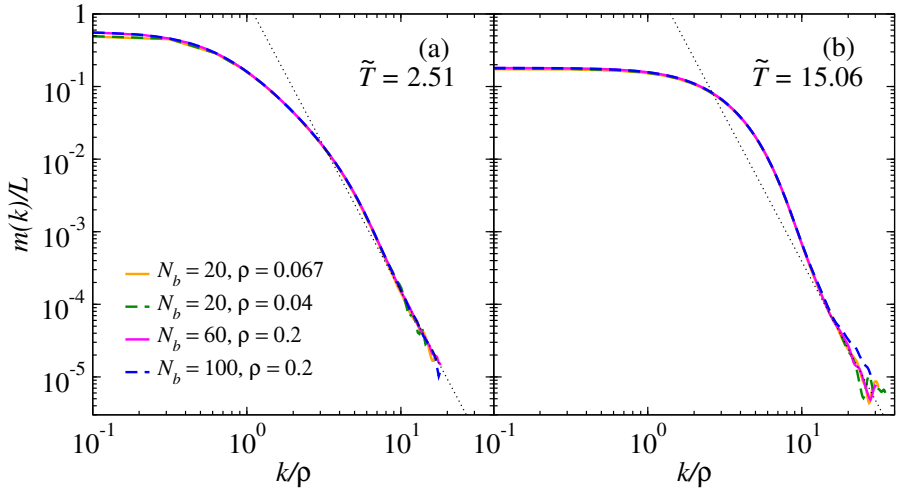

Figure 3.12: Finite temperature results for the scaled momentum distribution function of the homogeneous Lieb-Liniger gas with different average number of particles and densities at finite $\gamma = 8.33$. The scaled temperature in the plots is: (a) $\tilde{T} = 2.51$ and (b) $\tilde{T} = 15.06$. All results were obtained using the worm algorithm. Thin dotted lines depict k^{-4} behavior.

limit reported in Fig. 3.11, show that this is indeed the case. The behavior of the high momentum tails with increasing $\tilde{T}$ in Fig. 3.12 is qualitatively similar to that discussed in the Tonks-Girardeau limit.

While a close expression for Tan's contact for finite values of γ and finite temperatures is not available, a calculation up to order $1/\gamma$ (see Appendix A) reveals that $\tilde{\mathcal{C}} = C/(L\rho^4)$ can be written as [157–159]

$$\tilde{\mathcal{C}} = \frac{\tilde{T}^2}{2\pi} f_{3/2} \times \left[f_{1/2} + \frac{\tilde{T}^{1/2}}{\sqrt{\pi}\gamma} (2f_{1/2}^2 + f_{-1/2} f_{3/2}) \right] , \tag{3.29}$$

where by f_ν it is meant $f_\nu(\mu/k_BT)$. This further supports the correctness of the scaling used in Fig. 3.12.

3.3.2 Trapped Systems

3.3.2.1 Tonks-Girardeau Limit

As for the ground-state case, let us discuss how to scale density profiles in the Tonks-Girardeau limit at finite temperature. Dividing Eq. (3.20) by k_BT, we obtain

$$\frac{\mu(x)}{k_BT} = \frac{\mu(0)}{k_BT} - \frac{m\omega^2 x^2}{2k_BT} , \tag{3.30}$$

Using the LDA and the fact that, as discussed in the previous section, in homogeneous systems $\mu/(k_BT) = h_4(2mk_BT/\hbar^2\rho^2)$, we can rewrite Eq. (3.30) as

$$h_4 \left[\frac{\tilde{T}(0) n^2(0)}{n^2(x)} \right] = h_4[\tilde{T}(0)] - \frac{x^2}{a_{HO}^4 \tilde{T}(0) n^2(0)} , \tag{3.31}$$

where $\tilde{T}(0) = 2mk_BT/[\hbar^2 n^2(0)]$. Now, let us find the position $L_{\rm FT}$ in the trap at which the chemical potential vanishes. At zero temperature, the position at which the chemical potential vanishes is also the position at which the density vanishes. However, this is not the case anymore at finite temperature. For $\mu(x) = 0$, $h_4[2mk_BT/\hbar^2 n^2(x)] = 0$ and, using Eq. (3.31), $L_{\rm FT} = \sqrt{\tilde{T}(0) h_4[\tilde{T}(0)]}\, n(0) a_{HO}^2$. Defining $\tilde{x} = x/L_{\rm FT}$, Eq. (3.31) can be rewritten as

$$h_4 \left[\frac{\tilde{T}(0) n(0)^2}{n(x)^2} \right] = h_4[\tilde{T}(0)](1 - \tilde{x}^2) . \tag{3.32}$$

Defining $\tilde{n}(x) = n(x)/n(0)$, we see that Eq. (3.32) implies that

$$\tilde{n}(x) = h_5[1 - \tilde{x}^2, \tilde{T}(0)] \; . \tag{3.33}$$

At this point, we note that Eq. (3.33) has exactly the same form as Eq. (3.26), with $h_0 \to h_5$ and $\gamma(0) \to \tilde{T}(0)$. Using that $N_b = 2\int_0^\infty n(x)dx$, we get that $n(0) = h_6[\tilde{T}(0)]\tilde{\rho}$ and $L_{\rm FT} = h_7[\tilde{T}(0)]\tilde{L}$. This means that, once $\tilde{T}(0)$ has been fixed, a scaling as the one used for the ground state case will produce universal density profiles at finite temperature. In other words, for a fixed $\tilde{T}(0)$, $\tilde{\rho}$ and $\tilde{L}$ determine the average density in the system and an effective system size. Hence, given the fact that LDA is expected to work for sufficiently large system sizes at any finite

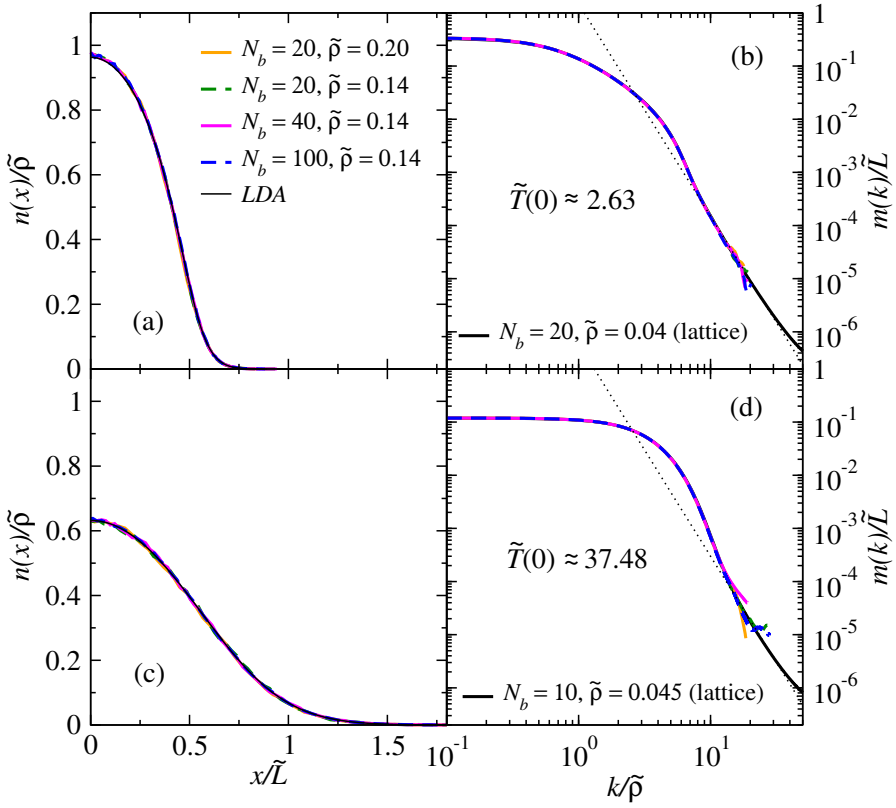

Figure 3.13: Finite temperature results for [(a) and (c)] the scaled density profiles and [(b) and (d)] momentum distribution functions of harmonically trapped Tonks-Girardeau gases with [(a) and (b)] $\tilde{T}(0) \approx 2.63$ and [(c) and (d)] $\tilde{T}(0) \approx 37.48$. In (a) and (c), black solid lines show the LDA predictions. In (b) and (d), the black solid lines show results of the lattice calculations. All other curves were obtained using the worm algorithm. In (b) and (d), thin dotted lines depict k^{-4} behavior.

temperature (because of finite correlation lengths), plots of $m(k)/\tilde{L}$ vs $k/\tilde{\rho}$ are expected to exhibit data collapse.

In Figs. 3.13(a) and 3.13(c), we show plots of $n(x)/\tilde{\rho}$ vs $x/\tilde{L}$ for systems with different average number of particles, densities in the center of the trap, and temperatures, but all with the same value of $\tilde{T}(0) \approx 2.63$ [Fig. 3.13(a)] and $\tilde{T}(0) \approx 37.48$ [Fig. 3.13(c)]. All the scaled density profiles exhibit the predicted data collapse and are in excellent agreement with the LDA prediction. In Figs. 3.13(b) and 3.13(d), we show the corresponding scaled momentum distribution functions, which also exhibit an almost perfect data collapse. The results for the momentum distribution functions exhibit an excellent agreement between the worm algorithm calculations and the lattice approach results. The latter allow us to reach smaller values of $m(k)/\tilde{L}$ (larger values of $k/\tilde{\rho}$) so that the k^{-4} momentum tails can be better resolved.

3.3.2.2 Finite Interaction Strength

The scaling of trapped systems with finite interaction strengths at finite temperature is the most challenging one. From the ground state analysis in the presence of a trap we know that $\gamma(0)$ needs to be kept fixed. From the finite temperature analysis of homogeneous systems we learned that γ and $\tilde{T}$ need to be fixed, while the finite temperature analysis of the trapped Tonks-Girardeau gas revealed that $\tilde{T}(0)$ needs to be fixed. Putting all this together we can advance that, for finite interaction strength, trapped systems at finite temperature will only exhibit scaling collapse if $\gamma(0)$ and $\tilde{T}(0)$ are fixed. We can also advance, from the analysis of trapped systems with finite interaction strength in the ground state and in the Tonks-Girardeau limit at finite temperature that using $\tilde{\rho}$ and $\tilde{L}$ will allow one to achieve the expected collapse.

In Fig. 3.14 we show results for the scaled momentum distribution function of trapped systems with the same value of $\gamma(0)$ and two values of $\tilde{T}(0)$. They all exhibit a nearly perfect collapse. The features observed in the momentum tails of the homogeneous case are also apparent here. Namely, Tan's contact increases with increasing temperature but at the same time the k^{-4} tails develop starting at higher values of k and smaller values of $m(k)$.

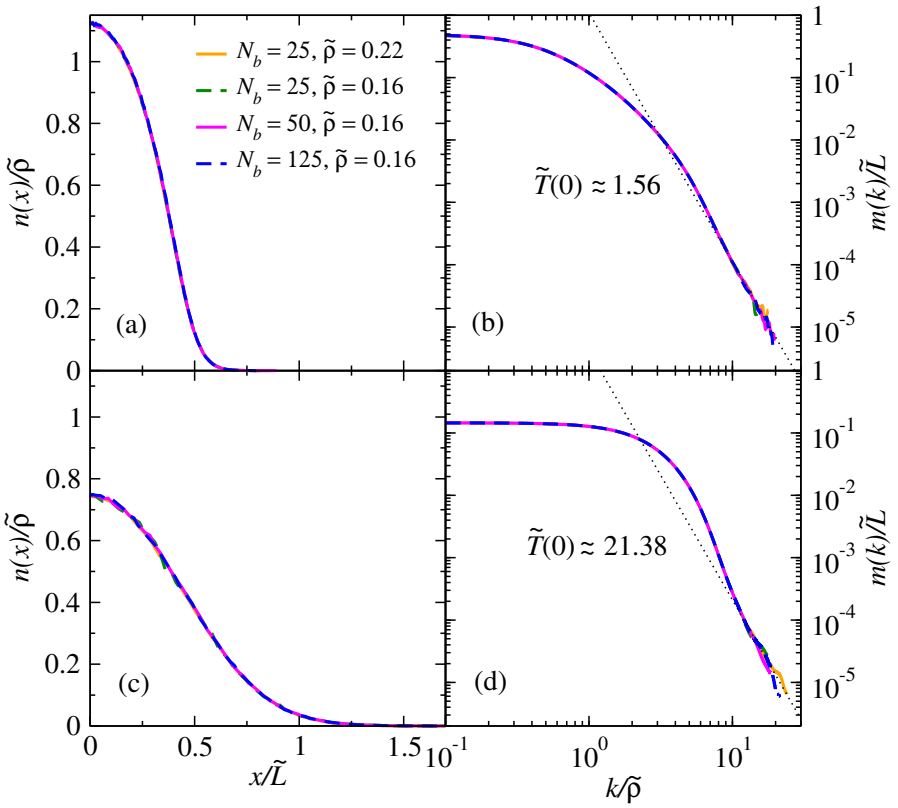

Figure 3.14: Finite temperature results for [(a) and (c)] the scaled density profiles and [(b) and (d)] momentum distribution functions of harmonically trapped Lieb-Liniger gases with [(a) and (b)] $\gamma(0) \approx 9.3$, and $\tilde{T}(0) \approx 1.56$ and [(c) and (d)] $\tilde{T}(0) \approx 21.38$. All curves were obtained using the worm algorithm. In (b) and (d), thin dotted lines depict k^{-4}.

Chapter 4

Multiband Effects and the 1D Bose-Hubbard Model

In this chapter, we focus on the incommensurate Mott insulator transition in continuous space. To study it, we use PIMC with worm updates [137–139], as detailed in Ref. [160]. We compute phase diagrams obtained by changing the lattice depth while keeping the contact interaction strength constant. We consider systems with fillings of up to two bosons per site. We show that for strong contact interactions, even for deep lattices and an average of one particle per site ($n = 1$), there are significant deviations from the Bose-Hubbard model predictions for the phase diagram when the parameters of that model are determined using Wannier functions. We introduce an inverse confined scattering analysis that allows one to restore the validity of the Bose-Hubbard model for strong interactions, deep lattices, and $n = 1$.

This chapter is organized as follows. We start with the model Hamiltonian in Sec. 4.1. We first introduce two limits of the Hamiltonian. In the weak interacting and deep lattice limit, the model reduces to one-band Bose-Hubbard model, with Hubbard parameters obtained from the Wannier functions, see Sec. 4.1.1. In the strong interacting and shallow lattice limit, the model can be described by the sine-Gordon Hamiltonian, and a pinning transition exists for $\gamma \gtrsim 3.5$. We study the commensurate transition through the analysis of the energy gaps and bipartite fluctuations. Then, we study the incommensurate transition in Sec. 4.2. We use two indicators to locate the transition between the superfluid and insulating phases, i.e., the superfluid fraction and the zero-momentum Matsubara Green's function. We found the results for the phase boundaries are biased due to finite imaginary

time discretization $\Delta\tau$, and the bias vanishes linearly with $\Delta\tau$. We then compare the energy gaps obtained using the continuous model to Bose-Hubbard predictions. In Sec. 4.5.1, we compare result of the gaps when the Hubbard parameters are determined using Wannier functions. We give a detailed review of the inverse confined scattering analysis in Sec. 4.4. We also discuss the method for calculating the multiband U by solving the two-body Schrödinger equation in a harmonic trap in Sec. 4.3. We show a comparison of the gaps with the multiband corrected Hubbard parameters in Sec. 4.5.2.

4.1 Model Hamiltonian

We consider bosons with repulsive contact interactions in the presence of an external periodic potential $V_{\text{ext}}(x) = V_0 \sin^2(k_L x)$:

$$\hat{H} = \sum_{i=1}^{N} \left[-\frac{\hbar^2}{2m} \frac{\partial^2}{\partial \hat{x}_i^2} + V_{\text{ext}}(\hat{x}_i) \right] + g_{1\text{D}} \sum_{i<j=1}^{N} \delta(\hat{x}_i - \hat{x}_j) \,, \tag{4.1}$$

where N is the number of particles, V_0 is the lattice depth, and $k_L = 2\pi/\lambda$, with λ being the lattice wavelength (the lattice spacing is then $a = \lambda/2$). We also define the unit of energy as the recoil energy $E_R = \hbar^2 k_L^2/(2m)$. In the absence of $V_{\text{ext}}(x)$, H reduces to the Lieb-Liniger model, which is integrable via the Bethe ansatz [6]. $g_{1\text{D}}$ is the strength of the contact interactions, which is related to the effective 1D scattering length $a_{1\text{D}}$ via $g_{1\text{D}} = -2\hbar^2/(m a_{1\text{D}})$, and to the Lieb-Liniger parameter γ via $\gamma = m g_{1\text{D}}/(\hbar^2 \rho)$ [2].

4.1.1 Weak Interaction and Deep Lattice

The full Hamiltonian for contact interacting bosons on a lattice is written here again for reference,

$$\hat{H} = \int dx \hat{\Psi}^\dagger(x) \hat{H}_0 \hat{\Psi}(x) + \frac{g_{1\text{D}}}{2} \hat{\Psi}^\dagger(x) \hat{\Psi}^\dagger(x) \hat{\Psi}(x) \hat{\Psi}(x) \,. \tag{4.2}$$

where $\hat{H}_0$ denotes a one-body Hamiltonian,

$$\hat{H}_0 = -\frac{\hbar^2}{2m} \frac{\partial^2}{\partial \hat{x}^2} + V_0 \sin^2(k_L \hat{x}) \,. \tag{4.3}$$

whose eigenstates are given by Mathieu functions, and reduce to plane wave states in the zero lattice depth limit. We label the one-body eigenstates with $\phi_q^n(x)$. Here, n is the band index and q labels discrete momentum. We can define Wannier orbitals belonging to the n^{th} band as,

$$\omega_n(x - x_i) = \frac{1}{\sqrt{L}} \sum_q e^{-iqx_i} \phi_q^n(x) \ . \tag{4.4}$$

If we project the Bose field operator $\hat{\Psi}$ ($\hat{\Psi}^\dagger$) on the basis of Wannier orbitals belonging to the lowest Bloch band, that is,

$$\hat{\Psi}(x) = \sum_i \hat{b}_i \omega_0(x - x_i) \ , \tag{4.5}$$

and assume the lattice is deep and interactions are weak, we obtain the Bose-Hubbard model,

$$\hat{H}_{\text{BH}} = -J \sum_i (\hat{b}_i^\dagger \hat{b}_{i+1} + \text{H.c.}) + \frac{U}{2} \sum_i \hat{b}_i^\dagger \hat{b}_i^\dagger \hat{b}_i \hat{b}_i + \sum_i (V_i - \mu) \hat{b}_i^\dagger \hat{b}_i \ . \tag{4.6}$$

The corresponding Hubbard parameters can be obtained from the Wannier functions,

$$\begin{aligned} J &= -\int dx \omega_0^*(x - x_i) \hat{H}_0 \omega_0(x - x_{i+1}) \ , \\ U &= g_{1\text{D}} \int dx |\omega_0(x)|^4 \ , \\ V_n &= \int dx \omega_0^*(x - x_i) \hat{H}_0 \omega_0(x - x_i) \ . \end{aligned} \tag{4.7}$$

Eq. (4.7) can be further simplified applying the definition of Wannier functions Eq. (4.4),

$$\begin{aligned} J &= -\frac{1}{L} \sum_p \cos(pa) \epsilon_0(p) \ , \\ U &= \frac{g_{1\text{D}}}{L^2} \int dx |\sum_p \phi_p^0(x)|^4 \ , \end{aligned} \tag{4.8}$$

where $\epsilon_0(p) = p^2/(2m)$ is kinetic energy of a free particle. For shallow lattices, U is usually overestimated and J underestimated.

4.1.2 Strong Interaction and Shallow Lattice

In the shallow-lattice limit, as mentioned before, $\hat{H}$ reduces to the $(1+1)$ sine-Gordon Hamiltonian [61, 62]. This model predicts that the pinning transition occurs for $\gamma > \gamma_c \approx 3.5$ or Luttinger parameter $K = 2$ [60]. Away from those limits, exact results for phase diagrams can be obtained using PIMC in continuous space [137–139]. In cubic lattices, related phase diagrams have been reported in Refs. [161, 162].

There are two common ways to locate the phase boundary of commensurate transition, one is to inspect the flow of Luttinger parameter K as the interaction strength $g_{1\mathrm{D}}$ (or effectively $a_{1\mathrm{D}}$) or the lattice depth V_0/E_R is changed along the transition line (with the same integer filling) [63, 64]. The other way is through the analysis of how the energy gap closes across the transition point [56].

4.1.2.1 Scaling Analysis of the Energy Gap

The commensurate transition is known to be of Berezinskii-Kosterlitz-Thouless (BKT) type [48], thus it is accompanied by an exponential closing of the single-particle energy gap

$$E_g \propto \exp\left[-\frac{b}{\sqrt{E_R(V_c^{-1}-V_0^{-1})}}\right] , \tag{4.9}$$

where the term in the exponential corresponds to the correlation length

$$\xi = \frac{b}{\sqrt{E_R(V_c^{-1}-V_0^{-1})}} . \tag{4.10}$$

b is independent of lattice depth V_0 and system size L. Due to the finite-size effect, one needs to study the scaling behavior of the gap based on the following ansatz [56],

$$LE_g(L) \times \left(1+\frac{1}{2\ln L + C}\right) = F\left(\frac{\xi}{L}\right) . \tag{4.11}$$

where, $F(\xi/L)$ is the scaling function. In general, C is an unknown constant [163]. In the system we study, $C \to \infty$, thus the logarithmic term in Eq. (4.11) vanishes. In the vicinity of the critical point within the superfluid region, $F(\xi/L)$ will be system size independent, due to the divergence of the correlation length ξ. Thus, one should observe the crossing of the rescaled gap $E_g^*(L) = LE_g(L)$ at the critical

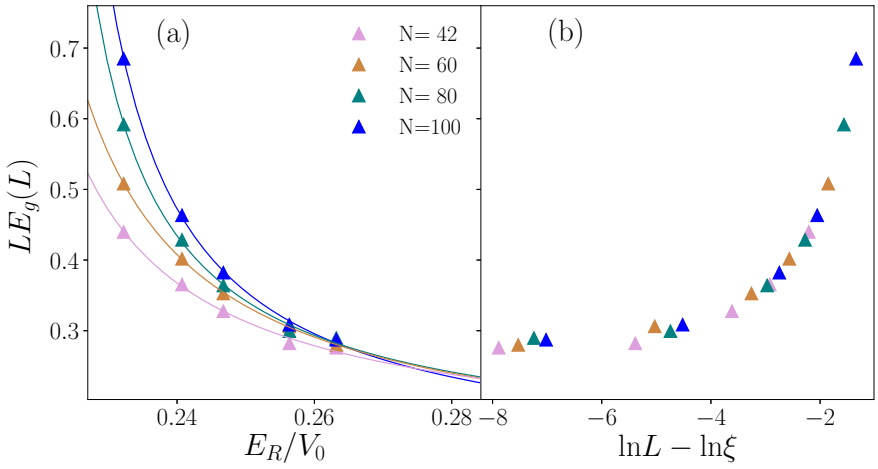

Figure 4.1: Finite-size scaling analysis of the energy gap for the commensurate transition at the tip of the first lobe ($n = 1$). The scattering length is kept fixed $a_{1D}/a = -2$ as the lattice depth is varied. The lines are fits to the data points following Eq. (4.10). The fitted values are $b = 1.217$ and $V_c/E_R = 3.648$.

point, an example is shown in Fig. 4.1(a). In addition, the curves $E_g^*(L)$ vs ξ/L (or equivalently $\ln L - \ln\xi$) should collapse onto a unique curve representing F. We can determine the critical point accurately by adjusting the parameters V_c and b. We are looking for the best collapse of the curves during the procedure [56]. An example of the collapse of data points is shown in Fig. 4.1(b). The energy gaps in Fig. 4.1(a) are calculated using the zero-momentum Green's function approach, which will be discussed in detail in Sec. 4.2.2.

4.1.2.2 Bipartite Fluctuations

A proven more efficient way of locating quantum critical points is through bipartite fluctuations [164, 165], defined in terms of particle numbers in our case,

$$\mathcal{F}_A = \langle \hat{N}_A^2 \rangle - \langle \hat{N}_A \rangle^2 \ . \tag{4.12}$$

Similar to all other entanglement measures, bipartite fluctuations $\mathcal{F}$ within a subsystem of length L_A exhibit a strict area law for gapped ground states $\mathcal{F}_{\text{gapped}} \propto L_A^{d-1}$, whereas for a gapless ground state, $\mathcal{F}_{\text{gapless}} \propto L_A^{d-1} \ln L_A$. Here, d is the dimension of the system. Due to the drastic difference in entanglement scaling, we are able to use $\mathcal{F}$ as an order parameter to locate quantum critical point. For the

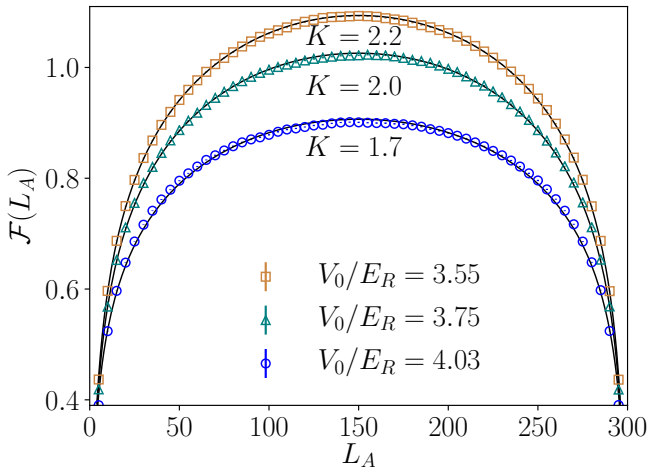

Figure 4.2: Bipartite fluctuations for systems at unit filling with $N = 60$ bosons and scattering length $a_{1D}/a = -2$. Results for three difference lattice depths are shown. They correspond to Luttinger parameters K crossing the critical point.

system with Hamiltonian Eq. (4.1) under study, bipartite fluctuations are described by the following formula for finite system size L,

$$\mathcal{F}(L_A) = \frac{K}{\pi^2} \ln \left[\frac{L}{\pi} \sin \left(\frac{\pi L_A}{L} \right) \right] + \text{Const.} , \tag{4.13}$$

thus one could obtain an accurate estimation of the Luttinger liquid parameter K by fitting the finite size formula [164].

To numerically calculate the bipartite fluctuations, we use the worm algorithm in the canonical ensemble (sampling in particle number conversed configuration space). Fig. 4.2 shows examples of $\mathcal{F}$ as a function subsystem size L_A. The lines, fitted according to Eq. (4.13), follow the simulated results, confirming the validity of the Luttinger liquid description of our model in the parameter region. As V_0/E_R further increases, the $\mathcal{F}$ curve flattens in the middle and the Luttinger liquid description breaks down. The fitted results of the Luttinger parameter K across the phase boundary is shown in Fig. 4.3. The critical point can be easily and accurately located from the fact that $K_c = 2$. The transition point for $a_{1D}/a = -2$ is $V_c/E_R = 3.75$ from bipartite fluctuations, which is consistent with $V_c/E_R = 3.648$ from the scaling analysis of the gap.

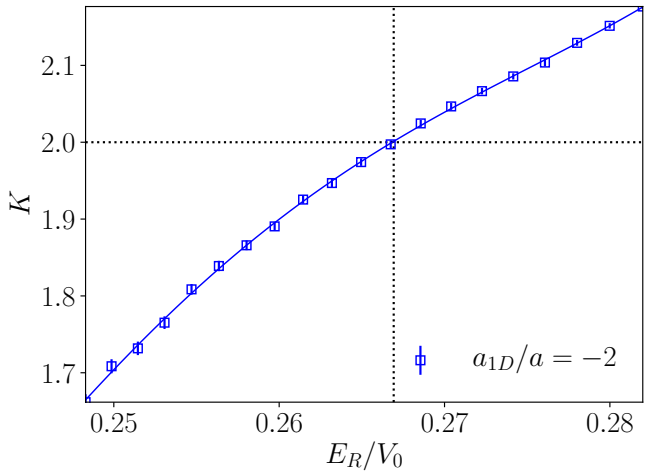

Figure 4.3: Luttinger liquid parameter K obtained from fitting the bipartite fluctuation curves in Fig. 4.2, with scattering length $a_{1D}/a = -2$ and varying lattice depth across the transition point. The critical value $V_0/E_R = 3.75$ by locating the point on curve where $K = 2$. The line is polynomial fit to the data points.

4.1.2.3 Commensurate Transition

As discussed in previous sections, both analyzing gaps and bipartite fluctuations can help study the commensurate transition. We report results of the phase diagram at commensurability $na = 1$ and 2 in Fig. 4.4. The result for $na = 1$ has been reported in Ref. [63, 64], and we recover their results here with different indicators. Both cases show significant deviations from the perturbative sine-Gordon theory with bare Luttinger parameters K. However, the PIMC result is consistent with the prediction of pinning transition. This indicates that the sine-Gordon theory only gives accurate predictions at zero lattice depth. Any finite lattice leads to a renormalization of the Luttinger parameter K. The agreement of the Bose-Hubbard prediction with the numerics at $na = 1$ is accidental. We show that this does not hold anymore at $na = 2$. In addition, at $V_0/E_R \to 0$, the Bose-Hubbard prediction is slightly different to the field theoretical prediction of the transition point at $\gamma_c \approx 3.5$.

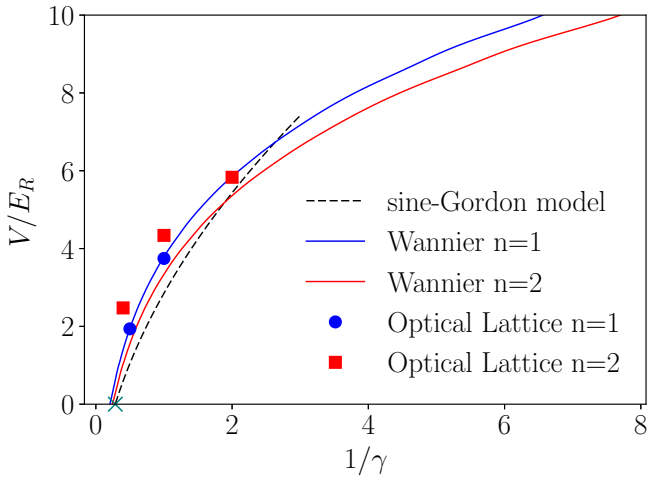

Figure 4.4: Phase diagram in the $\gamma - V_0$ plane at commensurability ($n = 1$ and $n = 2$). Solid circles and squares represent critical points from Monte Carlo simulation at filling 1 and 2 respectively. Lines are the Bose-Hubbard predictions using Wannier functions, as outlined in Sec. 4.1.1 and the critical values $(J/U)_c$ are from Ref. [56]. The dark-green cross indicates the critical interaction strength γ_c. The dashed line is the result of the bare sine-Gordon theory [60, 61].

4.2 Phase Diagrams

As mentioned before, we are interested in the phase diagrams obtained by changing the lattice depth while keeping a_{1D} (and hence γ) constant, as done in most optical lattice experiments [2, 59]. In order to obtain accurate phase boundaries of the model in the thermodynamic limit, one needs to choose carefully the numerical estimators (indicators) to study, taking into account both accuracy and computation complexity [164]. Here, we choose two indicators to locate the transition between the superfluid and insulating phases.

4.2.1 Superfluid Fraction

The superfluid density $\rho_s = mL\langle \hat{W}^2 \rangle / (\hbar^2 \beta)$ [139], where $\langle \hat{W}^2 \rangle$ is the winding-number estimator and L is the system size. In the thermodynamic limit, ρ_s is nonzero in the superfluid phase and vanishes in the Mott-insulating phase. In finite systems, ρ_s satisfies a scaling relation in the critical regime [166]: $\rho_s L^{\xi/\nu} = F(|\mu - \mu_c| L^{1/\nu})$, where the critical exponent $\xi = \nu(d + z - 2)$, $d = 1$ is the dimension,

and the correlation length exponents and dynamical critical exponents are $\nu = 1/2$ and $z = 2$, respectively, for the incommensurate transition. At the critical point, $\rho_s L^{\xi/\nu}$ is independent of the system size. Thus, one can obtain the transition point from the crossing of curves for different system sizes.

Figure 4.5 shows an example of such an analysis for the $n = 1$ lower boundary, for a lattice depth $V_0/E_R = 3.55$ and a scattering length $a_{1D}/a = -1$. For sufficiently large systems sizes, the transition point and its error can be obtained by taking the mean value and the standard deviation, respectively, of the series of crossing points between ρ_s for system size L_i and L_{i+1}, where $i = 1, 2, ...$ labels the system sizes simulated. For Fig. 4.5, this analysis gives $\mu_-/E_R = -0.1602 \pm 0.0002$.

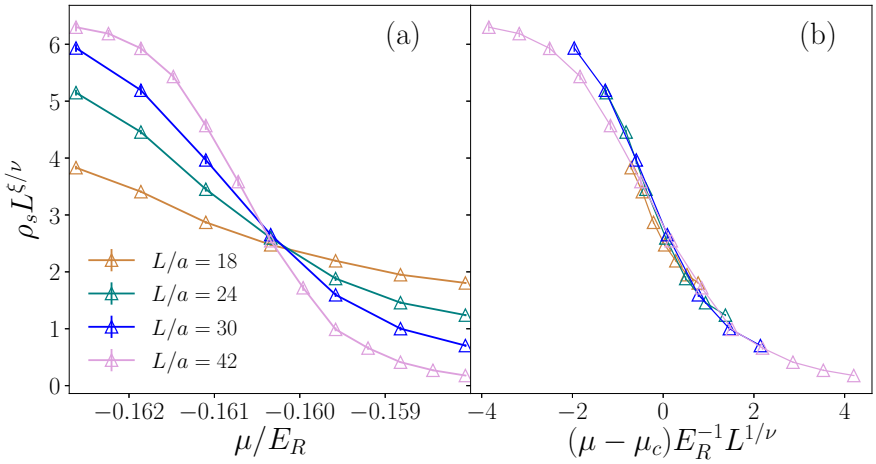

Figure 4.5: Finite-size scaling analysis of the superfluid density for the incommensurate transition at the lower boundary of the first lobe ($n = 1$). The lattice depth is $V_0/E_R = 3.55$ and the scattering length is $a_{1D}/a = -1$.

4.2.2 Zero-momentum Matsubara Green's Function

The other is the zero-momentum Matsubara Green's function. It requires the calculation of the momentum-space Green's function $G(p, \tau)$ [167]. Since the ground-state has zero total momentum, here we focus on $G(p = 0, \tau)$. In the vicinity of the transition point, within the Mott-insulating phase, $G(p = 0, \tau)$ decays exponentially with the imaginary time τ as $\tau \to \pm\infty$: $G(p = 0, \tau) \to Z_\pm \exp(\mp\epsilon_\pm \tau)$, where $\epsilon_\pm$ is the single-particle or -hole excitation energy. In the grand-canonical ensemble, $\epsilon_\pm$ is defined relative to the chemical potential μ with $\epsilon_\pm = |\mu - \mu_\pm|$, where $\mu_\pm$ gives

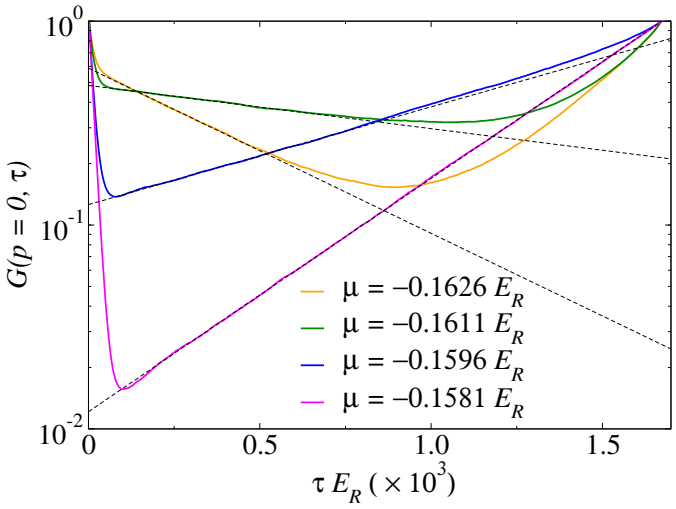

Figure 4.6: $G(p = 0, \tau)$ vs τ for different values of the chemical potential near the lower phase boundary of the Mott lobe with filling $n = 1$. The lattice depth is $V_0/E_R = 3.55$, the scattering length is $a_{1D}/a = -1$, and in all cases the system has $L/a = 42$.

the upper and lower boundaries of the Mott lobe.

To probe the robustness of the method, there are two issues that need to be addressed. The first one is, given a particular system size, how sensitive the result for μ_+ or μ_- (depending on the boundary of interest) is from the specific value of μ selected close to the boundary but within the Mott lobe. To check for this, we did simulations with different input chemical potentials but the same value of the lattice depth $V_0/E_R = 3.55$ and scattering length $a_{1D}/a = -1$. The results are reported in Fig. 4.6 for a system with $L/a = 42$. For all chemical potentials selected close to the Mott-insulator–superfluid boundary, one can identify the exponential behavior of the Matsubara Green's functions. From the fit of the exponent $\epsilon_- = \mu - \mu_-$, we obtain essentially the same value $\mu_-/E_R = -0.1607 \pm 0.0001$ for all values of μ used.

The second issue that needs to be addressed in the effect of the system having a finite extent. Figure 4.7 depicts results for the same lattice depths and scattering length as Fig. 4.7, $\mu = -0.1581 E_R$, and for different system sizes with $L/a = 24, 30, 42, 60$ lattice sites. The slope of the curves is essentially the same for the largest system sizes, which makes apparent that finite-size effects are negligible for $L/a \gtrsim 42$. All results reported in what follows were obtained for $L/a = 60$.

To determine critical points, it is less computationally demanding to use $G(p =$

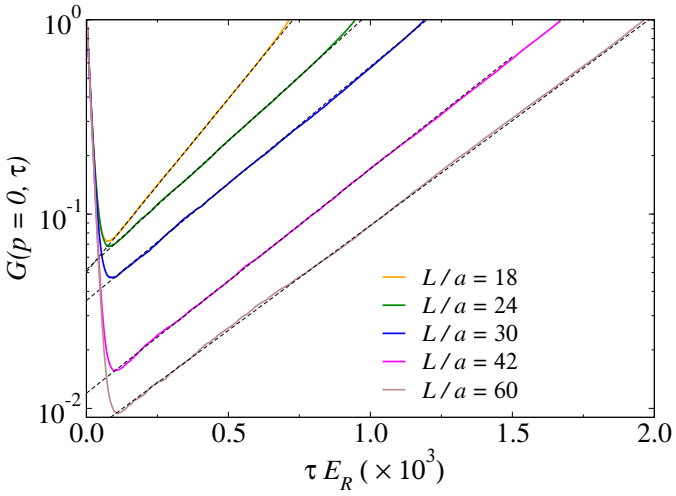

Figure 4.7: $G(p = 0, \tau)$ vs τ in systems with different number of particles and sites, but such that $n = 1$. The lattice depth is $V_0/E_R = 3.55$, the scattering length is $a_{1D}/a = -1$, and the chemical potential is $\mu = -0.1581 E_R$.

$0, \tau)$ than the finite-size scaling analysis of ρ_s. In the former approach one only needs to do a calculation for a sufficiently large system size for one value of μ close to the phase boundary to determine μ_+ or μ_-, while in the latter multiple simulations with different values of μ and L are needed to locate the crossing point. We then use $G(p = 0, \tau)$ for constructing the phase diagrams, while the scaling of ρ_s is mainly used to check results of the former approach.

4.2.3 Mott Lobes at $n = 1$ and $n = 2$

In Fig. 4.8, we report the phase diagrams obtained for three values of a_{1D} and for Mott-insulating states with one particle ($n = 1$, main panel) and two particles ($n = 2$, inset) per lattice site. Note that, contrary to the usual way in which phase diagrams are reported, in Fig. 4.8 we plot the phase boundaries in terms of $\mu - \mu_0^c$, where μ_0^c is the critical chemical potential for the vacuum boundary as obtained in our simulations (it is independent of a_{1D}). This allows us to reduce a small chemical potential bias introduced by the finite discretization $\Delta\tau$ of imaginary time in our PIMC approach. Such a bias vanishes linearly with $\Delta\tau$, and for the small but finite values of $\Delta\tau$ used in our simulations, it is negligible when chemical potential differences are reported (see Sec. 4.2.4). In Fig. 4.8, open symbols depict points obtained using $G(p = 0, \tau)$, while the four solid symbols for $a_{1D} = -a$ depict

points obtained with the scaling of ρ_s. The latter can be seen to lead to results indistinguishable from those from $G(p = 0, \tau)$. Figure 4.8 shows that, as expected, the Mott lobes grow with increasing γ. Also, the lower boundary of the $n = 1$ Mott lobe becomes independent of γ for deep lattices. All Mott lobes studied here have a finite extent because $\gamma < \gamma_c$.

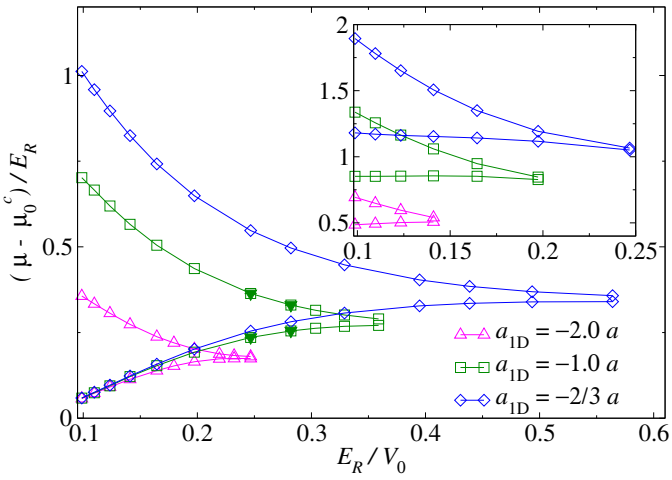

Figure 4.8: Mott lobes for one particle ($n = 1$, main panel) and two particles ($n = 2$, inset) per site. The lobes are obtained at fixed effective 1D scattering length $a_{1D}/a = -2.0,\ -1.0,\ -2/3$ (for $n = 1$, $\gamma = 1, 2$, and 3, respectively). The points are obtained from the zero-momentum Green's function (open symbols) and the scaling of the superfluid density (solid symbols). μ_0^c is the chemical potential at the vacuum boundary for each value of V_0 (determined from the zero-momentum Green's function). Lines between symbols are to guide the eye.

4.2.4 Phase Boundary Scaling from Finite Time Discretization

In our PIMC approach, imaginary time needs to be discretized. For translational invariant systems, this discretization introduces an error in the calculated physical observables that vanishes as $\Delta\tau^2$ [139]. When calculating the critical chemical potential for the superfluid to Mott insulator transition in the presence of an optical lattice, the error introduced by the imaginary time discretization vanishes linearly with $\Delta\tau$.

In Fig. 4.9(a), we plot how the error for determining the lowest boundary of the $n = 1$ Mott insulator in the Tonks-Girardeau limit ($|a_{1D}|/a \ll 1$) scales

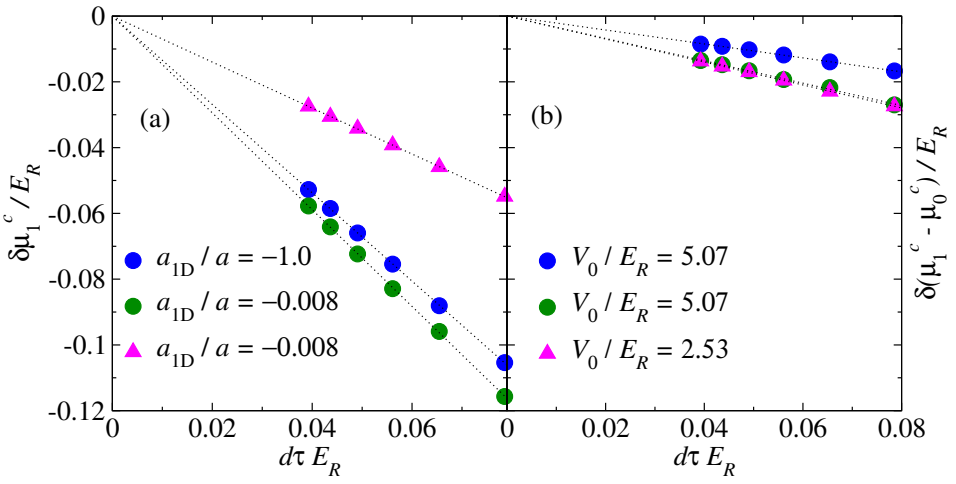

Figure 4.9: Scaling of the critical chemical potential at the lower phase boundary of the $n = 1$ Mott lobe as a function of the imaginary time discretization $\Delta\tau$, for the Tonks-Girardeau limit $a_{1D}/a = -0.008$ and for $a_{1D}/a = -1$ ($\gamma = 2$). Panel (a) shows the scaling of $\delta\mu_1^c$ and panel (b) shows the scaling of $\delta(\mu_1^c - \mu_0^c)$. See the text for the definitions of $\delta\mu_1^c$ and $\delta(\mu_1^c - \mu_0^c)$.

with $\Delta\tau$ for $L/a = 60$ (the system size used throughout the text). We define $\delta\mu_1^c \equiv \mu_1^c(\Delta\tau) - \mu_1^c(\Delta\tau = 0)$, where $\mu_1^c(\Delta\tau = 0)$ is obtained from a linear fit to the data. The linear scaling is apparent in the plots. We have compared $\mu_1^c(\Delta\tau = 0)$ to the prediction of a band-structure calculation for free fermions μ_f^c. Since the two should agree as $\gamma \to \infty$, this comparison provides a way to check the correctness of $\mu_1^c(\Delta\tau = 0)$. We have found that $\mu_f^c - \mu_1^c(\Delta\tau = 0) < 0.004E_R$, in all cases analyzed. Deeper lattices lead to larger errors, as one needs prohibitively smaller values of $\Delta\tau$ to reach the appropriate scaling regime. Figure 4.9(a) also shows results for $\gamma = 2$ ($a_{1D} = -1.0a$) and $V_0 = 5.07E_R$. The scaling is still linear but, when compared with the Tonks-Girardeau limit, the magnitude of the prefactor is smaller, i.e., the error decreases as the contact interaction strength decreases.

Since doing such an scaling analysis for all points in the phase diagrams reported in the main text is computationally prohibitive for us, instead of reporting $\mu_1^c(\tau)$ (or any other boundary), we have reported differences with respect to the chemical potential at the vacuum boundary obtained also from PIMC simulations: $\mu_0^c(\tau)$. In Fig. 4.9(b) we show how $\delta(\mu_1^c - \mu_0^c) \equiv [\mu_1^c(\Delta\tau) - \mu_0^c(\Delta\tau)] - [\mu_1^c(\Delta\tau = 0) - \mu_0^c(\Delta\tau = 0)]$ scales with $\Delta\tau$. One can see that while the scaling is still linear, and nearly independent of the lattice depth, the error due to a finite value of $\Delta\tau$ in

$\mu_1^c(\Delta\tau) - \mu_0^c(\Delta\tau)$ is significantly smaller (and negligible in the scale of the plots in the main text) than the one in $\mu_1^c(\Delta\tau)$, specially for deep lattices. The error is further reduced with reducing the contact interaction strength. In Fig. 4.9(b), the error for $a_{1\mathrm{D}} = -1.0a$ is almost one-half of the error in the Tonks-Girardeau limit.

4.3 Multiband Renormalized On-site Interaction

The on-site interaction energy U in the one-band Bose-Hubbard model represents the energy of repulsion for particles on the same lattice sites, calculated with the zeroth band Wannier functions. However, interactions tends to promote particles to higher bands to avoid overlaps between single particle wave functions. For a single-site problem, one can obtain the ground-state wave function by solving the many-body interacting Hamiltonian (see Appendix D for detailed formulations). In general, we can write the complete Hilbert space in a many-particle Fock basis, defined as $|N(n)\rangle = |n_0, n_1, ...\rangle$ where n_α denotes population of the αth orbital. The ground state of the non-interacting Hamiltonian is $|\Psi_0(n)\rangle = |n, 0, 0, \ldots\rangle$, in which all particles occupy the lowest single-particle orbital. On the hand, when interaction presents, the many-body ground state is a superposition of local Fock states,

$$|\Psi_{\mathrm{GS}}(n)\rangle = \sum_N c_N(n)\,|N(n)\rangle \ . \tag{4.14}$$

For Hamiltonian with only two-body interaction terms, such as the one-band Bose-Hubbard model in Eq. (4.6), the ground state energy E_n^{MO} can be directly related to the two-body interactions U_2,

$$E_n^{\mathrm{MO}} = \frac{U_2}{2} n(n-1) \ . \tag{4.15}$$

For more general cases with m-body interactions,

$$\begin{aligned} E_n^{\mathrm{MO}} = &\frac{U_2}{2} n(n-1) + \frac{U_3}{6} n(n-1)(n-2) \\ &+ \frac{U_4}{24} n(n-1)(n-2)(n-3) + \ldots \ . \end{aligned} \tag{4.16}$$

The renormalized wave functions and occupations of higher bands is particle number dependent and has been observed experimentally via analyzing quantum phase

revivals after a sudden quench of the lattice depth [65].

In a simplified case involving two particles with contact interaction in an external harmonic trap, the Schrödinger was solved analytically by T. Busch *et al.* [168]. In Busch's method, the two-body Hamiltonian can be decomposed in two independent Hamiltonians by introducing the center of mass and relative coordinates (R, r). Using $a_{\mathrm{HO}} = \sqrt{\hbar/m\omega}$ and $\hbar\omega$ as the units of length and energy, respectively, one has

$$\begin{aligned} \hat{\tilde{H}}_R &= -\frac{1}{4}\partial^2_{\tilde{R}} + \hat{\tilde{R}}^2 \ , \\ \hat{\tilde{H}}_r &= -\partial^2_{\tilde{r}} + \frac{1}{4}\hat{\tilde{r}}^2 + \tilde{g}_{1\mathrm{D}}\delta(\hat{\tilde{r}}) \ , \end{aligned} \tag{4.17}$$

where $\tilde{g}_{1\mathrm{D}} = -2a_{\mathrm{HO}}/a_{1\mathrm{D}}$. The eigenfunctions of $\hat{\tilde{H}}_R$ are the harmonic oscillator eigenfunctions $\phi_n(\tilde{R})$. The Hamiltonian of the relative motion $\hat{\tilde{H}}_r$ can also be solved analytically. The eigenfunctions with even parity are given by the Tricomi's confluent hypergeometric function $U(a, b, z)$

$$\psi_n(\tilde{r}) \propto e^{-\tilde{r}^2/4} U\left(\frac{1}{4} - \frac{\tilde{E}_n}{2}, \frac{1}{2}, \frac{\tilde{r}^2}{2}\right) \ . \tag{4.18}$$

$\tilde{E}_n$ is the corresponding eigenenergy determined by the following relation

$$-\frac{\tilde{g}_{1\mathrm{D}}}{2} = \frac{\Gamma\left(-\frac{\tilde{E}_n}{2} + \frac{3}{4}\right)}{\Gamma\left(-\frac{\tilde{E}_n}{2} + \frac{1}{4}\right)} \ , \tag{4.19}$$

where, $\Gamma(x)$ is the Gamma function. The ground state wavefunction of the two interacting particles in the harmonic trap is then $\Psi_{\mathrm{GS}}(\tilde{r}, \tilde{R}) = \phi_0(\tilde{R})\psi_0(\tilde{r})$, and the on-site repulsion is computed as: $U = \langle \Psi_{\mathrm{GS}} | \hat{H}_{\mathrm{int}} | \Psi_{\mathrm{GS}} \rangle$. In Fig. 4.10(a), we plot U/E_R vs V_0/E_R obtained as explained above and compare it to the results obtained using Wannier functions. It is apparent that one-band approximation overestimates all Hubbard interactions in the strongly interacting regime, see $a_{1\mathrm{D}}/a = -1.0$ and $-2/3$ for example.

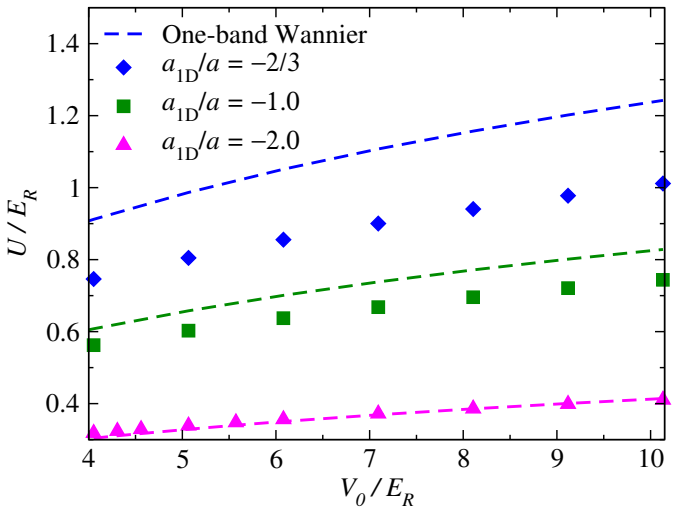

Figure 4.10: On-site repulsion U computed using the ground state of two interacting particles in a harmonic potential (symbols), and one-band Wannier functions (lines).

4.4 Inverse Confined Scattering Analysis

4.4.1 1D Scattering Length

As in Refs. [8, 169], we define the 1D analog of the three-dimensional scattering length a_{3D}. For a translationally invariant system, the scattering wave function for two bosons with total momentum zero can be written as (in the principal domain $x_1 > x_2$ and asymptotic limit $x_1 - x_2 \to \infty$)

$$\Psi^{(2)}_{\infty}(x_1, x_2) = e^{i\theta_{\text{lattice}}(q)}\psi(x_1, q)\psi(-x_2, q) + e^{-i\theta_{\text{lattice}}(q)}\psi(x_2, q)\psi(-x_1, q) \quad \text{for} \quad x_1 - x_2 \to \infty \,, \tag{4.20}$$

where $\psi(x, q)$ is the plane-wave eigenfunction with positive momentum q and energy $\epsilon(q)$, and by definition $\psi(-x, q) = \psi(x, -q)$. For any nonvanishing interaction, the scattering phase $\theta_{\text{lattice}}(q)$ is finite and goes asymptotically to zero as momentum q approaches zero. The scattering length a_{1D} characterizes the first nontrivial term in the Taylor expansion of the scattering phase in powers of the Bloch vector q,

$$a_{1D} = -\lim_{q \to 0^+} \theta_{\text{lattice}}(q)/q \,. \tag{4.21}$$

This definition gives the effective scattering length a_{1D} of the Lieb-Liniger model, which was introduced previously. Discretizing the Lieb-Liniger Hamiltonian, one obtains the Bose-Hubbard model and its corresponding scattering length $a_{BH} = -4Ja/U$ [170, 171].

When an external lattice is added, the propagating part of the two-body wave function has the same form as Eq. (4.20), but with $\psi(x, q)$ being a Bloch-state eigenfunction and $\epsilon(q)$ being its corresponding eigenenergy. For q different from half-integer multiples of the lattice wave vector k_L, $\psi(x, q)$ and $\psi(-x, q)$ can be shown to be linearly independent. The idea is to obtain U/J by comparing the exact low-energy scattering amplitude from the Bose-Hubbard model (a_{BH}) and that of the continuum model (a_{CM}) in Eq. (4.1). Our approach is different from the one followed in Refs. [172, 173], where scattering analyses were carried out for Feshbach resonances.

4.4.2 Properties of the Bosonic Scattering Solutions

The full bosonic scattering wave function $\Psi^{(2)}(x_1, x_2)$ with zero center-of-mass (COM) Bloch momentum yields the following properties.

1. Outside the interaction line $x_1 = x_2$, $\Psi^{(2)}(x_1, x_2)$ must be an eigenstate of the two-body free Hamiltonian

$$\hat{H}_{0,2\text{-b}} = \hat{H}_0(\hat{x}_1) + \hat{H}_0(\hat{x}_2) \ , \tag{4.22}$$

   with a real eigenenergy $E_{2\text{-b}} = 2\epsilon(q)$.

2. Due to the bosonic symmetry requirement, $\Psi^{(2)}(x_1, x_2)$ must be symmetric with respect to the particle permutation

$$\Psi^{(2)}(x_1, x_2) = \Psi^{(2)}(x_2, x_1) \ . \tag{4.23}$$

3. The full two-body Hamiltonian

$$\hat{H}_{2\text{-b}} = \hat{H}_{0,2\text{-b}} + g_{1D}\delta(\hat{x}_1 - \hat{x}_2) \ , \tag{4.24}$$

   remains invariant under translation $x_i \to x_i + a$, for $i = 1, 2$. Thus the set of

eigenstates of $\hat{H}_{2\text{-b}}$ must be reducible to $\Psi^{(2)}(x_1, x_2)$, such that

$$\Psi^{(2)}(x_1 + a, x_2 + a) = \exp\left[i\frac{\mathcal{L}(x_1 + x_2)}{2}\right]\Psi^{(2)}(x_1, x_2) \ . \tag{4.25}$$

That means, they must be a Bloch form along the COM axis. The asymptotic form Eq. (4.20) fixes the COM Bloch vector $\mathcal{L} = 0$, thus

$$\Psi^{(2)}(x_1 + a, x_2 + a) = \Psi^{(2)}(x_1, x_2) \ . \tag{4.26}$$

4. The full two-body Hamiltonian Eq. (4.24) is invariant under inversion, $x_i \to -x_i$ for $i = 1, 2$. Thus the set of eigenstates of $\hat{H}_{2\text{-b}}$ must be reducible to states of a definite parity. Specially, the asymptotic form Eq. (4.20) imposes even parity,
$$\Psi^{(2)}(-x_1, -x_2) = \Psi^{(2)}(x_1, x_2) \ . \tag{4.27}$$

5. Observe that the one-body free Hamiltonian $\hat{H}_0$ is time-reversal invariant, i.e., purely real. This property implies that if a Bloch state $\psi(x, q)$ is an eigenstate of $\hat{H}_0$ with an eigenvalue $\epsilon(q)$, then its complex conjugate $\psi^\dagger(x, q)$ is also an eigenstate, corresponding to the same eigenvalue. If q is not a half-integer multiple of the lattice wave vector k_L, $\psi(x, q)$ and $\psi^\dagger(x, q)$ can be shown to be linearly independent. Since $\hat{H}_0$ is a second-order differential operator, it can only support no more than two linearly independent eigenstates. Thus, $\psi^\dagger(x, q)$ and $\psi(-x, q)$ (as mentioned before) are linearly dependent. Moreover, when $\psi(x, q)$ is chosen in such a way that $\psi(0, q)$ is a real function, then
$$\psi^\dagger(x, q) = \psi(-x, q) \ . \tag{4.28}$$

Without a loss of generality, we assume that

$$\psi(0, q) = 1 \ . \tag{4.29}$$

All this was a lengthy prelude to an assertion that when the Bloch states are normalized in such a way that the condition Eq. (4.29) holds, the asymptotic

eigenstate Eq. (4.20) becomes purely real

$$\Psi^{(2)}(x_1, x_2) = \text{real} \ . \tag{4.30}$$

6. The contact interaction between particles imposes a jump condition

$$\begin{aligned} &\Psi^{(2)}(R+\frac{r}{2}, R-\frac{r}{2})\Big|_{r\to 0^+} = \Psi^{(2)}(R+\frac{r}{2}, R-\frac{r}{2})\Big|_{r\to 0^-} \ , \\ &\partial_r\Psi^{(2)}(R+\frac{r}{2}, R-\frac{r}{2})\Big|_{r\to 0^+} = \partial_r\Psi^{(2)}(R+\frac{r}{2}, R-\frac{r}{2})\Big|_{r\to 0^-} \\ &-\frac{2}{a_{1\mathrm{D}}}\Psi^{(2)}(R+\frac{r}{2}, R-\frac{r}{2})\Big|_{r\to 0} \ . \end{aligned} \tag{4.31}$$

This jump condition leads to the following boundary condition in the principal domain $x_1 > x_2$,

$$\partial_r\Psi^{(2)}(R+\frac{r}{2}, R-\frac{r}{2})\Big|_{r\to 0^+} = -\frac{1}{a_{1\mathrm{D}}}\Psi^{(2)}(R, R) \ . \tag{4.32}$$

Here and below, $R = (x_1 + x_2)/2$ and $r = x_1 - x_2$ are the COM and relative positions of the particles.

4.4.3 Evanescent Part of the Scattering Wave Function

The asymptotic form Eq. (4.20) is not the only non-divergent at infinity, periodic (with frequency multiples of π/a), even and real eigenstate of the free two-body Hamiltonian Eq. (4.22) in the principal domain ($x_1 > x_2$). There is also a localized part of the two-body wave function. It has a total two-body energy $2\epsilon(q)$ but complex one-body energies $\varepsilon(\eta)$ and $\varepsilon(-\eta) \equiv \varepsilon(\eta)^\star$, where

$$\varepsilon(\eta) = \epsilon(q) + i\eta \ \text{ for } \ \eta > 0 \ . \tag{4.33}$$

For each $\varepsilon(\eta)$, one can find two linearly independent (assuming that the Bloch vector is not a half-integer-multiple of π/λ) Bloch eigenstates of the one-body Hamiltonian Eq. (4.3), labeled $\chi[x, k(\eta)]$ and $\chi[x, -k(\eta)] \equiv \chi[-x, k(\eta)]$. They are related by a mirror reflection, where $k(\eta)$ is a Bloch momentum and $\chi[x, k(\eta)]$ is a Bloch state corresponding to it. The (boson) symmetric localized part of the

two-body wave function has the form (in the principal domain $x_1 > x_2$)

$$\begin{aligned}\chi^{(2)}(x_1, x_2, \eta) \equiv \chi[x_1, k(\eta)]\chi[x_2, k(-\eta)] + \chi[-x_1, k(-\eta)]\chi[-x_2, k(\eta)] \\ \text{for } \; x_1 > x_2 \; \text{ and } \; \eta > 0 \; .\end{aligned} \tag{4.34}$$

In general, there are two possible choices of the Bloch momentum $k(\eta)$ for each energy. For simplicity, we require that the imaginary part

$$\mathrm{Im}[k(\eta)] > 0 \; \text{ for } \; \eta > 0 \; . \tag{4.35}$$

For $\eta < 0$, it can be shown that complex conjugate energies produce complex conjugate momenta, thus

$$k(-\eta) = k^*(\eta) \; \text{ for } \; \eta < 0 \; . \tag{4.36}$$

In addition, without loss of generality, we can fix the overall magnitude of the Bloch states using

$$\chi[0, k(\eta)] = 1 \; \text{ for } \; \forall \eta \; . \tag{4.37}$$

Notice that the state in Eq. (4.34) obeys all conditions listed in Sec. 4.4.2, and no other relative coefficients between the two constituent terms are needed. This must be in contrast to the asymptotically non-vanishing part of the scattering solution Eq. (4.20), where the factors constituting the terms are the same function of different variables, and more freedom in combining the terms exists.

We assume that the Bloch vector of the center-of-mass motion vanishes, and, as a result, the two-body scattering state is a periodic function of the center-of-mass coordinate. This leads, in turn, to the requirement that the real part of the corresponding Bloch momentum be a half-integer of k_L, i.e.,

$$\begin{aligned}\mathrm{Re}[k(\eta_l)] = \frac{l}{2}\frac{\pi}{a} \\ \text{for } \; l > 0 \; \text{ and } \; \eta_l > 0 \; , \;\; \eta_{l+1} > \eta_l \; .\end{aligned} \tag{4.38}$$

It can be shown that each two-body state $\chi^{(2)}(x_1, x_2, \eta_l)$ constitute a non-divergent at infinity, periodic (with frequency multiples of π/a), even with respect to the COM coordinate R, and real eigenstate of the free two-body Hamiltonian Eq.(4.22) outside of the interaction line $x_1 = x_2$. The jump of the gradient of the wave

function on the $x_1 = x_2$ will be cured by the δ-function coming from the interactions.

4.4.4 Equation for the Lattice Scattering Length

The full two-body scattering state can then be written as a combination of the propagating and localized components,

$$\Psi^{(2)}(x_1, x_2) = \Psi^{(2)}_{\infty}(x_1, x_2) + \sum_{l=1}^{\infty} A_l \, \chi^{(2)}(x_1, x_2, \eta_l) \; . \tag{4.39}$$

$\Psi^{(2)}(x_1, x_2)$ is an eigenstate of the two-body Hamiltonian with a real eigenvalue outside of the interaction line $x_1 = x_2$. Next, we define

$$\begin{aligned} \Psi^{(2)}_{+,\infty}(R, r) &\equiv \psi(R + \frac{r}{2}, q)\psi(R - \frac{r}{2}, -q) \\ \Psi^{(2)}_{-,\infty}(R, r) &\equiv \psi(R - \frac{r}{2}, q)\psi(R + \frac{r}{2}, -q) \; , \end{aligned} \tag{4.40}$$

of which we need

$$\begin{aligned} \Psi^{(2)}_{+,\infty}(R) &\equiv \lim_{q \to 0^+} \Psi^{(2)}_{+,\infty}(R, r)\Big|_{r=0} \\ \Psi'^{(2)}_{+,\infty}(R) &\equiv \lim_{q \to 0^+} \partial_r \Psi^{(2)}_{+,\infty}(R, r)\Big|_{r=0} \; . \end{aligned} \tag{4.41}$$

The jump boundary condition in Sec. 4.4.2 imposes the following relationship between a_{CM} and the coefficients A_l of the expansion (4.39):

$$\Psi^{(2)}_{+,\infty}(R) a_{\mathrm{CM}} = \lim_{q \to 0^+} \frac{\Psi'^{(2)}_{+,\infty}(R)}{iq} a_{\mathrm{1D}} - \sum_{l=1}^{\infty} \left[\chi^{(2)}_l(R) + a_{\mathrm{1D}} \chi'^{(2)}_l(R) \right] \tilde{A}_l \; , \tag{4.42}$$

where

$$\begin{aligned} \chi^{(2)}_l(R) &= \lim_{q \to 0^+} \chi^{(2)}(R + \frac{r}{2}, R - \frac{r}{2}, \eta_l)\Big|_{r=0} \\ \chi'^{(2)}_l(R) &= \lim_{q \to 0^+} \partial_r \chi^{(2)}(R + \frac{r}{2}, R - \frac{r}{2}, \eta_l)\Big|_{r=0} \; , \end{aligned} \tag{4.43}$$

and $\tilde{A}_l = \lim_{q \to 0^+} iA_l/(2q)$. Since all functions of R in Eq. (4.42) have at least a periodicity of π/k_L (and are even), a way to solve that equation numerically is to use Fourier expansions. For a given number $l_{\max}$ of terms in the sum in Eq. (4.39), one needs to keep the same number of terms in the Fourier expansion of

all the functions. As a result, one obtains an inhomogeneous $(l_{\max}+1)\times(l_{\max}+1)$ system of linear algebraic equations, the solution of which gives $a_{\rm CM}(l_{\max})$. We then extrapolate the results to $l_{\max}\to\infty$ to obtain $a_{\rm CM}$.

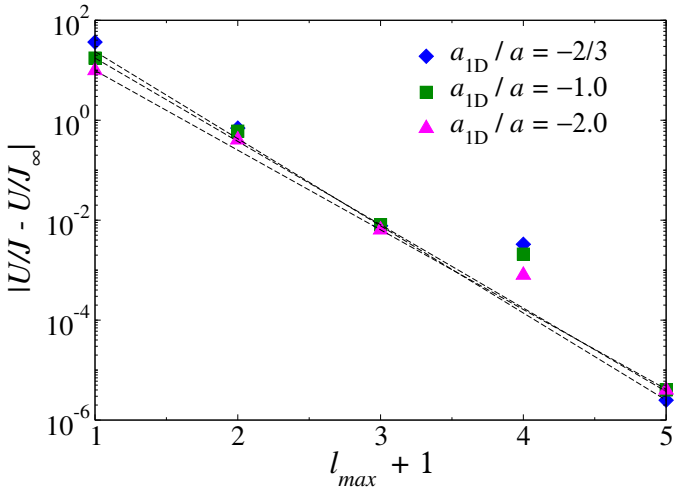

Figure 4.11: Examples of exponential fits to the solution of U/J as a function of $l_{\max}$ for different scattering lengths $a_{1D}/a=-2.0,\ -1.0,\ -2/3$. The three values of $U/J(\infty)$ in the figure were obtained from exponential fits to the points with $l_{\max}+1=1$, 3, and 5.

The Fourier expansion of all functions in Eq. (4.42) leads to the linear algebraic equations,

$$M\vec{V}=\vec{B}\ , \tag{4.44}$$

where

$$\begin{aligned} M_{m,n} &= \Psi^{(2)}_{+,\infty}(m)\delta_{n,0}+[\chi^{(2)}_n(m)+a_{1D}\chi'^{(2)}_n(m)](1-\delta_{n,0})\ ,\\ V_n &= a_{\rm CM}(l_{\max})\delta_{n,0}+\tilde{A}_n(1-\delta_{n,0})\ ,\\ B_m &= \lim_{q\to 0^+}\frac{\Psi'^{(2)}_{+,\infty}(m)}{iq}a_{1D}\ . \end{aligned} \tag{4.45}$$

We have use the following definition for the Fourier coefficients of any function $\Phi(R)$:

$$\Phi(m)=\sqrt{\frac{2}{a}}\int_0^a\cos(mk_LR)\Phi(R)dR\ . \tag{4.46}$$

In the previous expressions $m,n=0,1,2,...,l_{\max}$. Up to even odd effects, the solution $a_{\rm CM}(l_{\max})$ approaches exponentially fast to its asymptotic value with

increasing $l_{\max}$, see Fig. 4.11 for an example of the exponential scaling of U/J with increasing $l_{\max}$ with effective interaction strength between particle $a_{1D}/a = -1.0$.

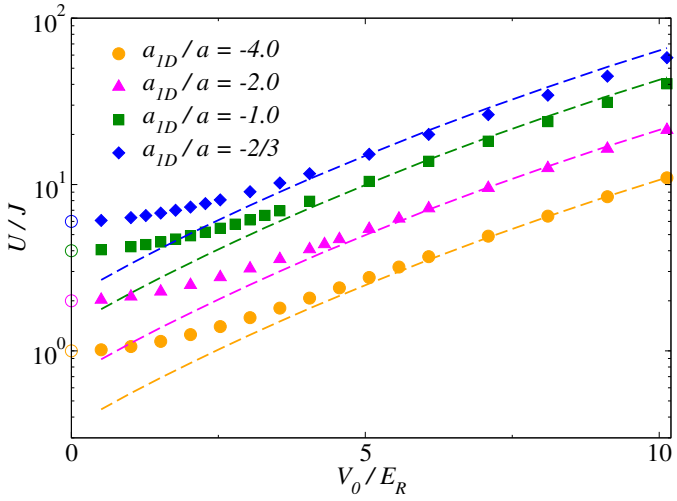

Figure 4.12: Comparison between U/J as obtained from the Wannier functions (dashed lines) and from the two-particle scattering analysis (solid symbols, consistent with those in the main panel). Open circles for $V_0/E_R = 0$ show the no-lattice asymptotic limit from scattering theory.

In Fig. 4.12, we compare U/J as obtained from the scattering and Wannier analyses for the same values of a_{1D}/a as in the main panels, as well as for $a_{1D}/a = -4$. For weak interactions ($a_{1D}/a \lesssim -2$) and deep enough lattices ($V_0/E_R \gtrsim 5$), one can see that the results from both approaches are nearly indistinguishable. On the other hand, for $a_{1D}/a > -2$ one can see that the Wannier analysis increasingly overestimates U/J as the lattice depth and a_{1D} are increased. This can be intuitively understood because interactions make the wave function of two particles in a site increasingly rigid to deformation as the lattice depth is increased. In that strongly interacting regime, the Wannier function calculations are not reliable even for deep lattices. As expected, independent of the value of a_{1D}, U/J from the inverse scattering analysis strongly deviates from the Wannier predictions for weak lattices. In the limit of vanishing lattice depth, the former predicts $U/J = -4a/a_{1D}$.

4.5 Diagrams of Energy Gaps

4.5.1 Gap and the One-band Bose-Hubbard Model

Having determined the phase diagrams, we compare the predictions of the PIMC simulations with those from the one-band Bose-Hubbard model. We first compare the phase diagrams in the Bose-Hubbard model setting, as shown in Fig. 4.13. As the interaction strengths are increased, one obtains increasingly compressed Mott lobes, in consistent with the effective multiorbital Hamiltonian prediction in Ref. [68].

In order to minimize the number of parameters that need to be computed for the comparison, we focus on the Mott gap: $E_g = \mu_+ - \mu_-$. As a first estimation, U and J are calculated within the one-band approximation using maximally localized Wannier states [174, 175]. The Bose-Hubbard phase diagram [55] is then translated into the parameters in the continuum. The results for $n = 1$ and $n = 2$ are presented in Figs. 4.14(a) and 4.14(b), respectively, and are compared to the PIMC results derived from Fig. 4.8.

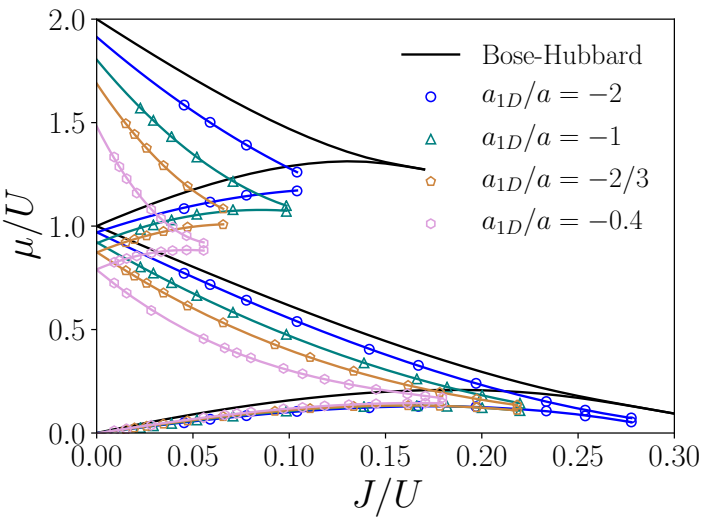

Figure 4.13: Phase diagrams in the picture of a one-band Bose-Hubbard model. The open symbols depict the results from PIMC simulations for $a_{1D}/a = -2.0, -1.0, -2/3, -0.4$. The lines connecting the open symbols are polynomial fits to guide an eye. The black lines come from the standard Bose-Hubbard prediction.

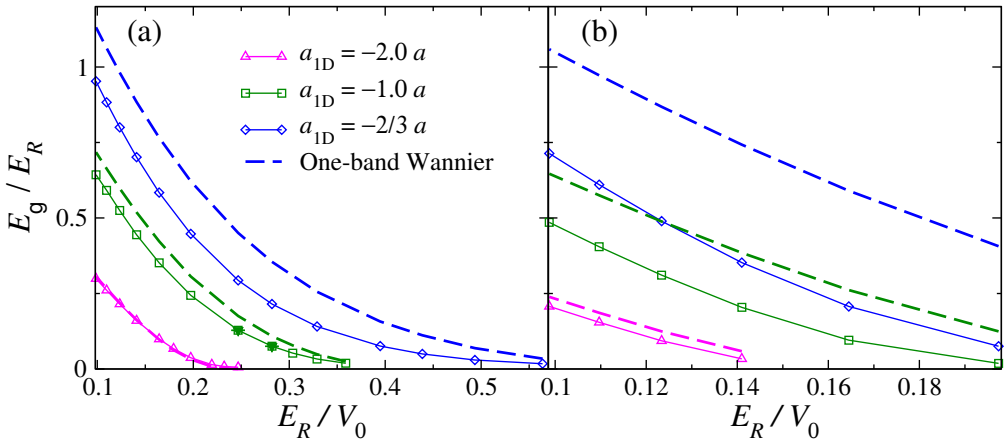

Figure 4.14: Mott gaps at fillings (a) $n = 1$ and (b) $n = 2$ vs E_R/V_0 for $a_{1D}/a = -2.0,\ -1.0,\ -2/3$. The open symbols depict the results from PIMC simulations. The dashed lines depict the Hubbard model prediction [55] translated into the continuum using U and J as obtained from maximally localized Wannier functions [174, 175].

For $a_{1D}/a = -2.0$ and $n = 1$ ($\gamma = 1$), the gap predicted by both approaches is nearly indistinguishable for all lattice depths. The same is expected to be true for even smaller values of a_{1D}, so we focus on higher fillings and higher values of a_{1D}. For $n = 2$ and $a_{1D}/a = -2.0$ ($\gamma = 1/2$), already a small deviation can be seen between the gap obtained from PIMC and the Hubbard model prediction. Striking differences, on the other hand, can be seen for $\gamma = 2$ and 3, particularly for the deepest lattices and $n = 2$. Counterintuitively, in Fig. 4.14(a), the gap predicted by the Hubbard model becomes increasingly larger than the exact one as the lattice depth is increased (the one-band prediction worsens as the lattice depth is increased). This suggests that, with increasing V_0, the one-band approximation leads to an increasing overestimation of U/J and hence of the gap (we will come back to this point later). Hence, our results show that, for $\gamma \gtrsim 1$, the closest agreement between the exact solution and the Hubbard model prediction is obtained for the weakest lattices, for which the one-band approximation is most uncontrolled.

4.5.2 Hubbard Model from Inverse Scattering Approach

When using Wannier functions, the fact that one neglects the effect of interactions is what leads to the overestimation of U/J inferred from Fig. 4.14. In order to account for interactions in the calculation of U/J, so that the values of U/J are the

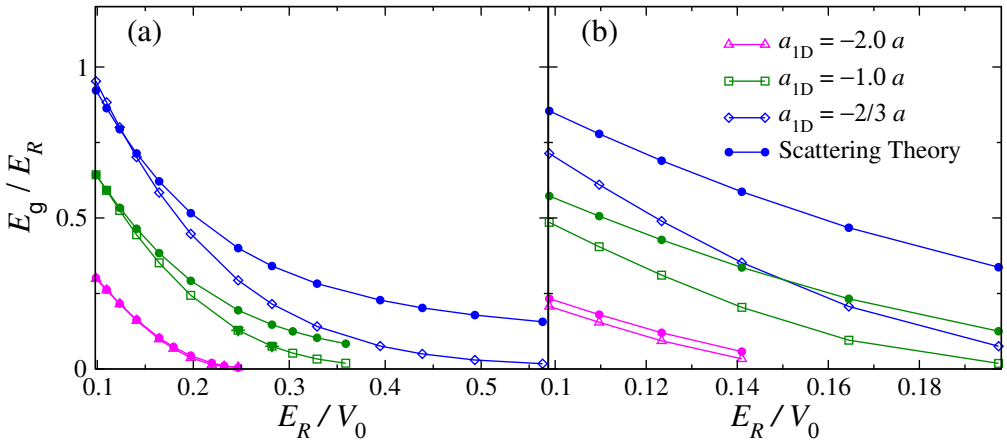

Figure 4.15: Mott gaps at fillings (a) $n = 1$ and (b) $n = 2$ vs E_R/V_0 for $a_{1D}/a = -2.0,\ -1.0,\ -2/3$. The open symbols depict the results from PIMC simulations. Solid symbols depict the Hubbard model prediction [55] translated into the continuum using U/J from the two-particle scattering analysis explained in the text and U obtained from the exact solution of two interacting bosons in a harmonic trap.

appropriate ones in the limit of deep lattices, we use the inverse scattering approach. In the main panels of Fig. 4.15, we show the Bose-Hubbard model predictions for the phase diagram translated into the continuum using the scattering analysis results for U/J and U obtained using the ground-state wave function of two interacting bosons in a harmonic trap [168]. For $n = 1$ [Fig. 4.15(a)] and $\gamma = 1$, there is almost no visible difference from the Wannier results. On the other hand, for $\gamma = 2$ and deep enough lattices, the Hubbard model with the improved values of U/J and U correctly predicts the value of the gap. For the deepest lattices for $\gamma = 3$, we find a small deviation between the gaps predicted by PIMC and by the Bose-Hubbard model. Its most likely origin is the failure of the harmonic potential to correctly predict U. Further studies are needed to find more accurate ways to determine U. For $n = 2$ and $a_{1D}/a \gtrsim -2$, the Bose-Hubbard results are clearly inadequate independent of how U/J and U are calculated.

Chapter 5

Sudden Expansion of 1D Hard-core Bosons

In this chapter, we explore finite-temperature effects in the expansion of hard-core bosons in 1D lattices. We introduce an exact approach to study dynamics based on an existing finite-temperature equilibrium method [46]. We find that the dynamical fermionization of the momentum distribution of hard-core bosons, originally discussed in the expansion from the ground state [31, 89, 90], occurs at all temperatures. For this effect, we focus on initial states with low site occupations, for which the cloud expands in a self-similar way. In contrast to the momentum distribution, the natural orbital occupations λ_η remain unchanged during the expansion and display the universal η^{-4} tail known from equilibrium calculations [44]. This means that, during the expansion, the natural orbital occupations allow one to distinguish hard-core bosons from noninteracting fermions.

We also study the expansion from initial Mott insulating domains. We show that while one-body correlations are enhanced during the dynamics, they are suppressed as the initial temperature is increased. The enhancement of such correlations is reminiscent of the dynamical quasicondensation shown to occur in pure states [88]. Nonzero temperatures have an effect in the expanding systems that is similar to that in systems in equilibrium [46], namely, power-law correlations are replaced by exponential ones. Surprisingly, we find that those systems appear to cool down during the melting of the Mott domains. They are effectively in local thermal equilibrium with temperatures that decrease with time. We explain this analytically using an emergent local Hamiltonian [133]. The cooling can be intuitively understood to be the result of energy being transferred from internal energy to center-of-mass

motion. We construct the corresponding reference Hamiltonian [93, 176] in order to illustrate this picture.

This chapter is organized as follows. In Sec. 5.1, we introduce the numerical approach developed to study dynamics of finite-temperature initial states. We study the effect of temperature in the fermionization of the momentum distribution during the expansion in Sec. 5.2. Section 5.3 is devoted to investigate the melting of an initial Mott insulating domain created in thermal equilibrium in the presence of a linear potential. We present a detailed discussion of the emergent local Hamiltonian solution in Sec. 5.3.2, and of the intuitive understanding of the effective cooling in terms of a reference Hamiltonian in Sec. 5.3.3.

5.1 Model and Method

Hard-core bosons provide an effective description of the Bose-Hubbard model in the limit of infinite on-site repulsion [2]. The hard-core boson Hamiltonian reads

$$\begin{aligned} &\hat{H} = \hat{H}_0 + \hat{H}_V \\ &\hat{H}_0 = -J\sum_l (\hat{b}_{l+1}^\dagger \hat{b}_l + \text{H.c.}), \quad \text{and} \quad \hat{H}_V = V_\alpha \sum_l l^\alpha \hat{n}_l \ , \end{aligned} \tag{5.1}$$

where $\hat{H}_0$ models nearest-neighbor hoppings with amplitude J, and $\hat{H}_V$ models a confining potential. The hard-core boson creation ($\hat{b}_l^\dagger$) and annihilation ($\hat{b}_l$) operators satisfy standard bosonic commutation relations with the constraint $(\hat{b}_l^\dagger)^2 = \hat{b}_l^2 = 0$. In $\hat{H}_V$, α denotes the exponent of the power-law potential, e.g., $\alpha = 2$ stands for the traditional harmonic confinement. In what follows, we set $J = k_B = \hbar = 1$ and the lattice spacing $a = 1$. Hamiltonian (5.1) can be mapped onto the spin-1/2 XX model via the Holstein-Primakoff transformation and then onto non-interacting spinless fermions via the Jordan-Wigner transformation [152, 177]

$$\hat{b}_l^\dagger = \hat{f}_l^\dagger \prod_{\beta=1}^{l-1} e^{-i\pi \hat{f}_\beta^\dagger \hat{f}_\beta} \ , \ \hat{b}_l = \prod_{\beta=1}^{l-1} e^{i\pi \hat{f}_\beta^\dagger \hat{f}_\beta} \hat{f}_l \ . \tag{5.2}$$

The corresponding fermionic Hamiltonian shares the same form with that of the hard-core bosons (up to a possible boundary term) with $\hat{b}_l^\dagger$ ($\hat{b}_l$) replaced by $\hat{f}_l^\dagger$ ($\hat{f}_l$), signaling the Bose-Fermi duality in 1D [11]. This means that hard-core bosons and fermion share the same thermodynamic properties for diagonal (site-occupation

related) observables, while nontrivial differences appear in off-diagonal one-body observables.

5.1.1 Finite Temperature Equilibrium Approach

We first review the finite temperature equilibrium lattice approach [46]. This approach is different from the ground state one [44, 45], in the sense that the ground state approach works in the canonical ensemble. In the finite temperature approach, in order to maintain the power law scaling of the computation complexity, we work in the grand-canonical ensemble. To avoid the particle-number dependence of the boundary term after the mapping, we restrict our analysis to open chains [46]. One the other hand, the canonical ensemble implementation at finite temperature scales exponentially with system size and particle number, and the difference of these two ensemble predictions turns out to be negligible already for small system sizes [46].

In the grand-canonical formalism, the hard-core boson one-body density matrix can be written in terms of the equivalent fermionic representation as

$$\rho_{ij} = \mathrm{Tr}\left[\hat{b}_i^\dagger \hat{b}_j \hat{\rho}_{\mathrm{GE}}\right] = \mathrm{Tr}\left[\prod_{\alpha=1}^{i-1} e^{-i\pi \hat{n}_\alpha^f} \hat{f}_i^\dagger \hat{f}_j \prod_{\beta=1}^{j-1} e^{i\pi \hat{n}_\beta^f} \hat{\rho}_{\mathrm{GE}}\right] , \tag{5.3}$$

where,

$$\hat{\rho}_{\mathrm{GE}} = \frac{1}{Z} \exp\left(-\frac{\hat{H}_f - \mu \hat{N}}{T}\right) , \tag{5.4}$$

is the grand-canonical density matrix,

$$Z = \mathrm{Tr}\left[\exp\left(-\frac{\hat{H}_f - \mu \hat{N}}{T}\right)\right] , \tag{5.5}$$

is the partition function and $\hat{H}_f$ the corresponding fermion Hamiltonian. A numerical evaluation of ρ_{ij} in Eq. (5.3) can be carried out using the fact that the trace of exponentials of bilinear forms in fermionic creation and annihilation operators over

Fock space can be written as [46, 178][1]

$$\mathrm{Tr}\left[\exp\left(\sum_{ij}\hat{f}_i^\dagger X_{ij}\hat{f}_j\right)\exp\left(\sum_{kl}\hat{f}_k^\dagger Y_{kl}\hat{f}_l\right)\cdots\right]=\det\left[I+e^X e^Y\cdots\right]\ . \tag{5.7}$$

A direct implementation of this property allows one to calculate the partition function as

$$Z=\det\left[I+\exp\left(-\frac{H_f-\mu I}{T}\right)\right]=\prod_\alpha\left[1+\exp\left(-\frac{E_\alpha-\mu}{T}\right)\right]\ , \tag{5.8}$$

where, H_f is the matrix representation of $\hat{H}_f$ and E_α are its eigenenergies. For the off-diagonal matrix elements, ρ_{ij} with $i\neq j$, one can write [46]

$$\hat{f}_i^\dagger\hat{f}_j=\exp\left(\sum_{kl}\hat{f}_k^\dagger A_{kl}\hat{f}_l\right)-1\ , \tag{5.9}$$

where matrix A has only one nonzero element $A_{ij}=1$. Thus, substituting $\hat{f}_i^\dagger\hat{f}_j$ in Eq. (5.3) results in the need to evaluate two determinants, one involving $e^A=I+A$ and the other one involving I. The strings arising from the Jordan-Wigner transformation contribute a diagonal matrix O_i (O_j) with the first $i-1$ ($j-1$) diagonal elements equal to -1 and the rest equal to 1. Hence, after some simplification, one obtains the off-diagonal terms of the one-body density matrix

$$\begin{aligned}\rho_{ij}=\frac{(-1)^{i-j}}{Z}\times\Big\{&\det\left[U_f^\dagger O_j(I-A)O_iU_f+e^{-(E_f-\mu I)/T}\right]\\&-\det\left[U_f^\dagger O_jO_iU_f+e^{-(E_f-\mu I)/T}\right]\Big\}\ ,\end{aligned} \tag{5.10}$$

where E_f is a diagonal matrix of eigenenergies $H_fU_f=U_fE_f$. Since the exponential term $e^{-(E_f-\mu I)/T}$ involves elements that are both exponentially large and exponentially small, it has been isolated from other matrices to avoid stability

[1] A general proof of Eq. (5.7) is given in Ref. [178]. For simplicity, one could start with just one exponential and transform $\hat{f}_i$ to $\hat{f}_\nu$, in which basis the kernel matrix X is diagonal,

$$\mathrm{Tr}\left(e^{\sum_{ij}\hat{f}_i^\dagger X_{ij}\hat{f}_j}\right)=\mathrm{Tr}\left(e^{\sum_\nu\hat{f}_\nu^\dagger X_\nu\hat{f}_\nu}\right)=\mathrm{Tr}\prod_\nu e^{\hat{f}_\nu^\dagger X_\nu\hat{f}_\nu}=\prod_\nu\left(1+e^{X_\nu}\right)=\det\left(1+e^X\right)\ . \tag{5.6}$$

The same should be true for a product of matrix exponentials, by choosing the basis where the matrix $e^Xe^Y\cdots$ are diagonal.

problems during the matrix multiplication. For the diagonal terms ρ_{ii}, one should notice that Eq. (5.9) is not applicable. Instead, one should consider

$$\exp\left(-i\pi \hat{f}_i^\dagger \hat{f}_i\right) = 1 - 2\hat{f}_i^\dagger \hat{f}_i \ . \tag{5.11}$$

Hence, matrix A in Eq. (5.10) should be replaced with B with only one nonzero element $B_{ii} = -2$. In this case, the inverse of $(I + B)$ is still itself. However, a prefactor from $\det[I + B] = -1$ should be added to the first determinant of Eq. (5.10), together with a global factor of $-1/2$. As a remark, one can prove that the method presented above is equivalent to keeping the same format as Eq. (5.10), that is the same A with now $A_{ii} = 1$. In this case, one should also realize the subsequent changes, e.g., $\det[I + A] = 2$ and $(I + A)^{-1} \neq (I - A)$.

Another, more efficient, way to obtain ρ_{ii} follows from the fact that ρ_{ii} is identical for non-interacting fermions and hard-core bosons (See Appendix C for a proof). For noninteracting fermions one has

$$\rho_{ii} = 1 - \left[I + e^{-(H_I - \mu I)/T}\right]^{-1}_{ii} \ . \tag{5.12}$$

This is the equivalent of Eq. (17) in Ref. [46] after correcting a typographical error. As a side note, $N = \sum_i \rho_{ii}$ gives the particle number in the system.

When temperature is low, the matrices in the determinants of Eq. (5.10) have matrix elements that are exponentially large and exponentially small. Thus, to calculate the determinants, one has to multiply exponentially large matrix elements with exponentially small ones, leading to instability issue in calculating determinants. To overcome this issue, a stabilization method is used [179].

5.1.2 Time-Evolving Initial Thermal States

We generalize the equilibrium lattice approach in Sec. 5.1.1 to study the time evolution of finite-temperature initial states. Specifically, we consider sudden quenches from an initial Hamiltonian $\hat{H}_I$ to Hamiltonian $\hat{H}_F$ at $\tau = 0$. Again, we use the grand-canonical ensemble, for which we devise a computational approach that has a computation time that scales polynomially with system size. The

equal-time one-body density matrix after time τ of the evolution can be written as

$$\begin{aligned}\rho_{ij}(\tau) &= \mathrm{Tr}\left[e^{i\hat{H}_F\tau}\hat{b}_i^\dagger\hat{b}_j e^{-i\hat{H}_F\tau}\hat{\rho}_I\right] \\ &= \mathrm{Tr}\left[e^{i\hat{H}_F\tau}\prod_{\alpha=1}^{i-1}e^{-i\pi\hat{n}_\alpha^f}\hat{f}_i^\dagger\hat{f}_j\prod_{\beta=1}^{j-1}e^{i\pi\hat{n}_\beta^f}e^{-i\hat{H}_F\tau}\hat{\rho}_I\right] ,\end{aligned} \tag{5.13}$$

where $\hat{\rho}_I = \hat{\rho}_{\mathrm{GE}}$ is the density matrix of the initial thermal state. Eq. (5.13) can be further simplified as Eq. (5.3), which results in

$$\begin{aligned}\rho_{ij}(\tau) = \frac{(-1)^{i-j}}{Z}\Big\{&\det\left[U_I^\dagger e^{iH_F\tau}O_j(I-A)O_i e^{-iH_F\tau}U_I + e^{-(E_I-\mu I)/T}\right] \\ &- \det\left[U_I^\dagger e^{iH_F\tau}O_jO_i e^{-iH_F\tau}U_I + e^{-(E_I-\mu I)/T}\right]\Big\} ,\end{aligned} \tag{5.14}$$

where $H_IU_I = U_IE_I$ ($H_FU_F = U_FE_F$), with E_I (E_F) being the diagonal matrix with the sorted eigenenergies of the initial (final) Hamiltonian. The matrix representation of the time evolution operator $e^{-i\hat{H}_F\tau}$ can be obtained as $e^{-iH_F\tau} = U_Fe^{-iE_F\tau}U_F^\dagger$. We want to emphasize that the exponential term $e^{-(E_I-\mu I)/T}$ is again isolated from the other matrices to maintain stability of matrix multiplications. The diagonal matrix elements ρ_{ii} can be calculated in a similar fashion detailed in sec. 5.1.1. The time-dependent implementation of Eq. (5.12) is

$$\rho_{ii}(\tau) = 1 - \left[e^{iH_F\tau}\left(I + e^{-(H_I-\mu I)/T}\right)e^{-iH_F\tau}\right]_{ii}^{-1} . \tag{5.15}$$

5.2 Fermionization

As mentioned before, due to the Bose-Fermi mapping, diagonal observables are identical in hard-core and spinless fermion systems [11]. Off-diagonal ones, such as two-point one-body correlations, on the other hand, are different. This leads to starkly different behaviors of the momentum distribution of hard-core bosons and fermions. In the ground state, the former exhibit quasicondensation at zero momentum (the occupation of the zero momentum mode scales with $\sqrt{N}$, where N is the number of bosons in the system) [2]. This cannot occur with noninteracting fermions because of the Pauli exclusion principle. In addition, the hard-core boson momentum distribution function exhibits high-momentum tails that decay

as k^{-4} [26, 39, 44]. Such tails are not present in the fermionic counterpart, in which the Fermi momentum cuts off the distribution. Studies of the momentum distribution of hard-core bosons during expansion dynamics have revealed that it approaches the momentum distribution of the fermionic system to which they can be mapped [31, 89, 90]. This has been explained in terms of a dynamical phase that appears during the expansion, and which results in an asymptotic momentum distribution of the hard-core bosons that is identical to the momentum distribution of the fermions in the external harmonic confinement [31]. Here, we show that such dynamical fermionization also occurs if the initial state is at nonzero temperature.

5.2.1 Momentum distribution

To study the dynamics, we start from a harmonically trapped system in thermal equilibrium. For sufficiently large systems, the initial state is characterized by the characteristic density $\tilde{\rho} = N/R$ and the temperature T, where $R = (V_\alpha)^{-1/\alpha}$ is the length scale introduced by the confining potential ($\alpha = 2$ for the harmonic trap). We are interested in the momentum distribution during the expansion after turning off the harmonic trap, which we calculate as [44–46]

$$n_k(\tau) = \frac{1}{R} \sum_{jl} e^{ik(x_j - x_l)} \rho_{jl}(\tau) \ . \tag{5.16}$$

In the thermodynamic limit and finite site occupations, a scaling solution with constant $[\tilde{\rho},\ T,\ \tau/N]$ characterizes the system [46, 89]. In the low-site-occupation limit, the lattice system maps onto a continuous system and a scaling solution with a reduced number of parameters $[T/\tilde{\rho},\ \tau\tilde{\rho}/N]$ exists. This is discussed in Ref. [160] for the equilibrium case. (Note that the characteristic density defined here is different from the one defined in Ref. [160], where the systems of interest were in the continuum.)

In this section, we focus on systems with low site occupations, so that they can be well described using scaling results from systems in the continuum. A previous study for the ground state indicates this is the case for $\tilde{\rho} \lesssim 0.2$ [89]. Analytic expressions for the time-dependent one-body density matrix during the expansion starting from the ground state in the continuum were derived in Ref. [31] and were recently generalized to finite-temperature situations in Refs. [33, 34]. From the

scaling transformation, the equal-time one-body density matrix $g(x, y; \tau)$ can be related to the initial one $g(x, y; 0)$ by the expression

$$g(x, y; \tau) = \frac{1}{f} g\left(\frac{x}{f}, \frac{y}{f}; 0\right) \exp\left(-\frac{i}{f}\frac{\dot{f}}{\omega}\frac{x^2 - y^2}{2a_{\mathrm{HO}}^2}\right) , \tag{5.17}$$

where the scaling parameter is $f(\tau) = \sqrt{1 + (\omega\tau)^2}$ for the expansion in the absence of a trap and $a_{\mathrm{HO}} = \sqrt{\hbar/m\omega}$ is the initial trapping length in the continuum. The parameters ω and m can be conveniently transformed into their lattice counterparts via $\hbar\omega = 2\sqrt{V_2 J}$ and $m = \hbar^2/(2Ja^2)$.

Since $\omega \propto R^{-1}$, one can observe that $\omega N/\tilde{\rho} = \mathrm{Const}$, thus $f = \sqrt{1 + \mathrm{Const} \times \tilde{\tau}^2}$ only depends on $\tilde{\tau} = \tau\tilde{\rho}/N$. In addition, it has been proven in Chapter 3, for Lieb-Liniger gas in thermal equilibrium, $g(x, y; 0)/\sqrt{\tilde{\rho}}$ vs $|x - y|\sqrt{\tilde{\rho}}$ follows a universal scaling solution given the effective temperature $\tilde{T} = T/\tilde{\rho}$. Thus it is sufficient to conclude that $|g(x, y; \tau)|$ in Eq. (5.17) follows the scaling solution with effective parameters $[\tilde{T},\ \tilde{\tau}]$. On the other hand, $\dot{f}/\omega$ depends also only on $\tilde{\tau}$,

$$\dot{f}/\omega = \omega\tau f^{-1} \propto \tilde{\tau} f^{-1} . \tag{5.18}$$

However, the only term left in the exponential $(x^2 - y^2)/(2a_{\mathrm{HO}}^2)$ is not the only function of the scaled positions $x\sqrt{\tilde{\rho}}$ and $y\sqrt{\tilde{\rho}}$. Thus $g(x, y; \tau)$ overall does not follow a universal scaling solution.

Figure 5.1 shows an example of the dynamics for an initial state with $\tilde{\rho} = 0.1$ and $T = 0.02$. During the early stages of the expansion [main panel in Fig. 5.1(a)], the peak in n_k at $k = 0$ is rapidly suppressed. This is followed by a redistribution of n_k (slower at high momenta) to fully match the corresponding momentum distribution of fermions. In contrast, the dynamics of the site occupations is self-similar, as expected from Eq. (5.17), and as shown in the main panel of Fig. 5.1(b) and its inset. The inset in Fig. 5.1(a) shows the difference between the initial momentum distribution at $T = 0.02$ and the ground state result. It highlights the effect of having a nonzero initial temperature in n_k.

In order to demonstrate, quantitatively, that the momentum distribution of hard-core bosons indeed approaches that of noninteracting fermions, we compute the relative difference $\delta n_k(\tau) = \sum_k |n_k(\tau) - n_k^f| / \sum_k n_k^f$, where n_k^f is the momentum distribution of the fermions [89]. In Fig. 5.2, we report results for systems with

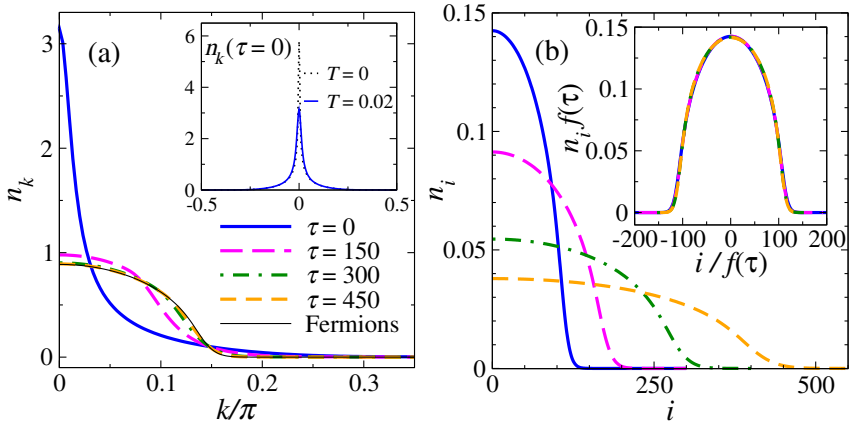

Figure 5.1: (a) Momentum (n_k) and (b) site (n_i) occupations for $N = 25$ hard-core bosons during the expansion in a lattice. The system is initially prepared in a harmonic trap with characteristic density $\tilde{\rho} = 0.1$ and temperature $T = 0.02$. The inset in panel (a) shows a comparison between n_k at $\tau = 0$ for $T = 0.02$ and $T = 0$, and highlights the effect of $T \neq 0$. The inset in panel (b) makes apparent the self-similar behavior of the site occupations n_i during the expansion.

$N = 25$ and $N = 50$ particles. In all cases, one can see that $\delta n_k(\tau)$ decreases with time. Note the data collapse for nonzero initial temperature when $\delta n_k(\tau)$ is plotted vs τ/N, so we expect that the results will not change if the number of particles is further increased while keeping the characteristic density constant. It is also apparent in the figure that the results for $\tilde{\rho} = 0.1$ [Fig. 5.2(a)] are qualitatively similar to those for $\tilde{\rho} = 0.32$ [Fig. 5.2(b)], which means that the behavior observed is robust to changes in $\tilde{\rho}$, for small enough $\tilde{\rho}$.

Next, we analyze at which times the relative difference reaches a given small value, say $\delta n_k = 0.05$ as marked by horizontal dotted lines in Fig. 5.2, as a function of the temperature of the initial state. The results of this analysis are reported in Fig. 5.3(a). They show that the rescaled time decreases, rather slowly but maybe exponentially, with increasing T. (The initial differences between the momentum distribution of hard-core bosons and fermions also decreases with increasing T.) Of more direct relevance to experiments is how the ratio between the cloud size at the time at which $\delta n_k = 0.05$ and the initial cloud size (R_F) changes with increasing T. Results for this quantity, using the full width at half maximum as a measure of the cloud size, are presented in Fig. 5.3(b). That figure shows that R_F decreases with increasing T, i.e., the fermionization of the momentum distribution of hard-core bosons may be easier to observe experimentally in systems that are initially at

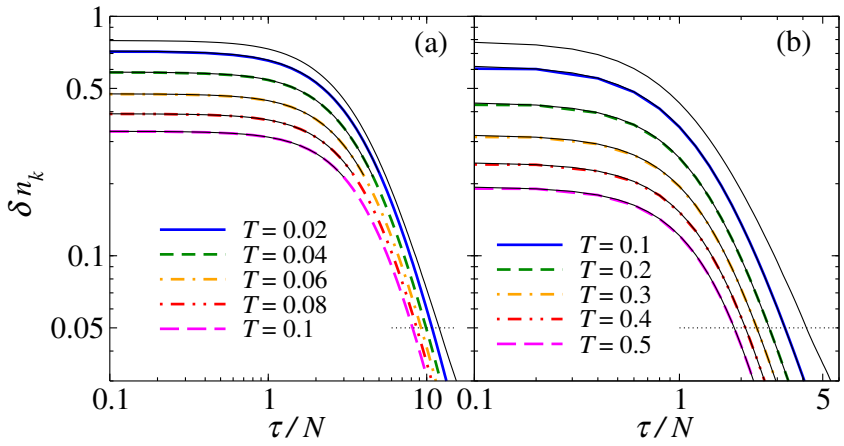

Figure 5.2: Decrease of the relative difference δn_k during the expansion for different initial characteristic densities: (a) $\tilde{\rho} = 0.1$ and (b) $\tilde{\rho} = 0.32$. Overlapping thick (color) and thin (black) lines show results for $N = 25$ and $N = 50$, respectively, and different values of T. The topmost black line depicts the ground state result for $N = 50$. Horizontal dotted lines mark $\delta n_k = 0.05$. The values of τ/N vs T for $\delta n_k = 0.05$ are reported in Fig. 5.3.

finite temperature.

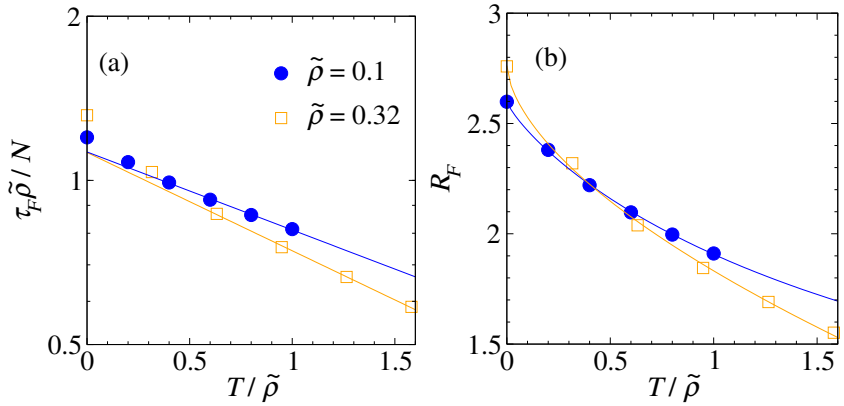

Figure 5.3: (a) Time τ_F at which $\delta n_k = 0.05$ (see Fig. 5.2) as a function of the effective temperature $T/\tilde{\rho}$. The solid lines are exponential fits to the numerical results. (b) Ratio R_F between the full width at half maximum (FWHM) at τ_F and the FWHM at $\tau = 0$ as a function of $T/\tilde{\rho}$. The solid lines are a guide to the eye.

5.2.2 Natural orbitals and one-body correlations

While the dynamical fermionization of the momentum distribution may lead one to conclude that the one-body correlations of hard-core bosons are approaching those of a system of noninteracting spinless fermions, this is not the case. This becomes clear if one studies the population of the natural orbitals, which are the eigenfunctions of the one-body density matrix [180]

$$\sum_j \rho_{ij}(\tau)\phi_j^\eta(\tau) = \lambda_\eta(\tau)\phi_i^\eta(\tau) \; . \tag{5.19}$$

In Fig. 5.4(a), we show the natural orbital occupations at different times. It is remarkable that they almost do not change for small and intermediate values of η (the lowest natural orbital occupation, λ_0, slightly increases), and that they are very different from those of a system of noninteracting fermions. All that happens during the expansion of hard-core bosons is that the tails $\lambda_\eta \propto \eta^{-4}$, known to occur in equilibrium [44], extend to larger values of η. These changes can be attributed to the presence of the underlying lattice. [In the continuum limit ($\tilde{\rho} \to 0$), $\lambda_\eta(\tau)$ is time independent.] Hence, the natural orbital occupations allow one to distinguish hard-core bosons from noninteracting fermions. Figure 5.4(b) shows the natural

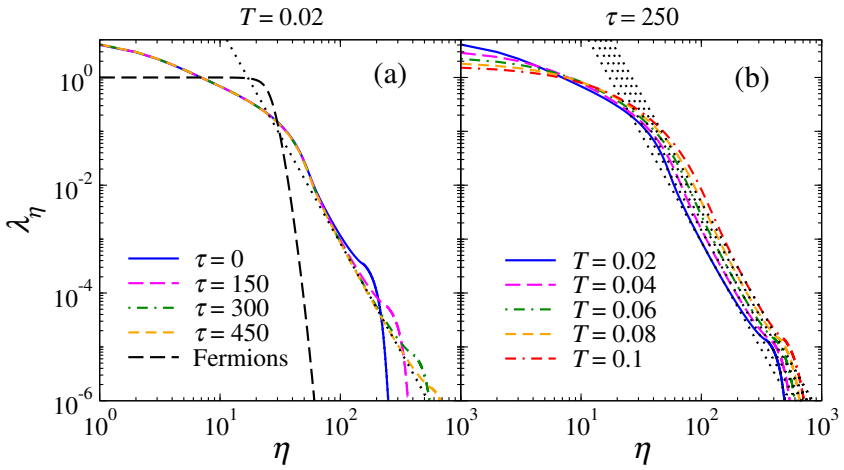

Figure 5.4: (a) Natural orbital occupations for the same initial parameters and times for which momentum and site occupations are reported in Fig. 5.1. The black dashed line depicts the natural orbital occupations of the noninteracting fermions, which do not change with time. (b) Natural orbital occupations at $\tau = 250$ for different initial temperatures T. All black dotted lines are η^{-4} fits to the tails.

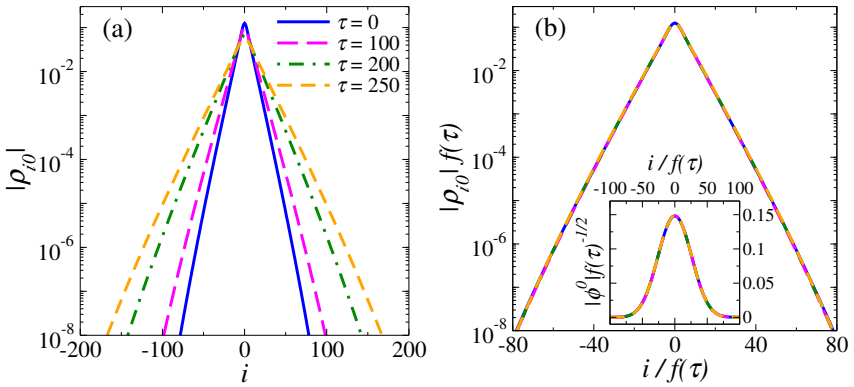

Figure 5.5: (a) One-body density matrix at different times for $N = 25$, $\tilde{\rho} = 0.1$, and $T = 0.1$. (b) Scaled results for the one-body density matrix (main panel), and the lowest natural orbital wavefunction (inset).

orbital occupations for different initial temperatures after the same expansion time. As in the initial state, as T increases, the population of the lowest natural orbitals decreases and the population of the tails increases, i.e., the prefactor of the η^{-4} tails increases. This is similar to the behavior of the momentum distribution of hard-core bosons in thermal equilibrium in the continuum, for which the prefactor of the k^{-4} momentum tails also increases with temperature [32, 160].

The fact that the natural orbitals remain (mostly) unchanged during the expansion follows from the scaling solution of one-body correlations in Eq. (5.17). In Fig. 5.5(a), we show how one-body correlations decay away from the center of our lattice system at different times. Figure 5.5(b) shows that both, the one-body correlations as well as the lowest natural orbital, are well described by the scaling solution.

5.3 Quasicondensation

5.3.1 Dynamics from a linear potential

For the symmetric expansion starting from an initial pure Fock state with one particle per site, it was shown in Ref. [88] that one-body quasi-long-range correlations develop dynamically and lead to the emergence of quasicondensates at finite momentum $k = \pm\pi/2$. Our goal in this section is to understand what happens when the initial state is not a pure state but a mixed thermal equilibrium state.

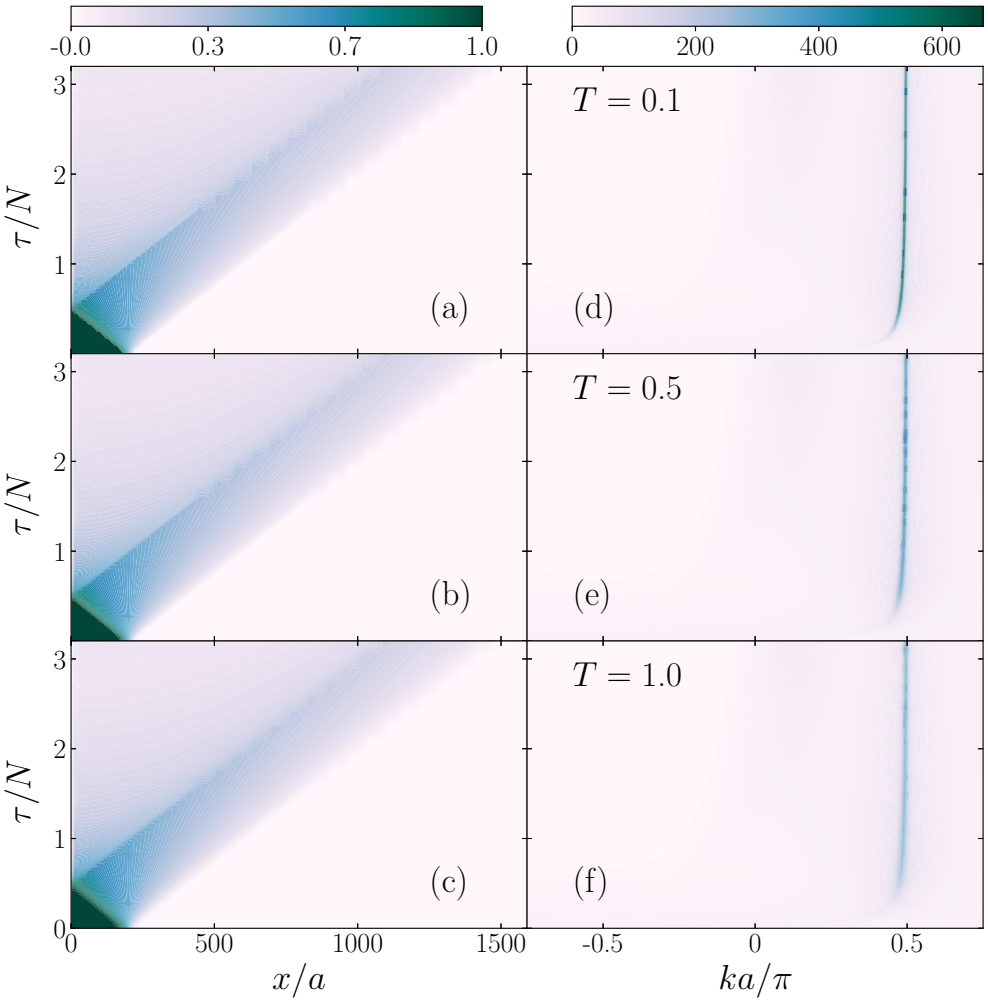

Figure 5.6: Contour plots of the density profiles (a)-(c) and momentum distributions (d)-(f) as functions of the expansion time. Panels (a)-(c) [or (d)-(f)] correspond to initial temperatures $T = 0.1$, $T = 0.5$, and $T = 1.0$, respectively. These systems contain $N = 200$ particles and, initially, $V_1 = 0.125$. Open boundaries are considered to, after the linear potential is turned off, constrain the expansion of the Mott domain to the right.

During the melting of a Mott insulator, while there are sites in the center with occupation one, the symmetric expansion can be described as two independent expansions to the left and to the right.

Here we focus on the expansion of finite-temperature Mott domains in one direction after turning off the confining potential. We construct them as thermal equilibrium states in the presence of a linear potential ($\alpha = 1$). For this potential, which has been studied in multiple works in the literature [101, 133, 176, 181], we

obtain an analytic understanding of the effective cooling observed during the free expansion dynamics. We note that these systems are not parity symmetric as the ones considered in the previous section in the harmonic potential.

In Fig. 5.6, we show (color) contour plots of the site occupations and momentum distributions as functions of time for three initial temperatures of the Mott domains. The site occupation profiles make apparent that the expansion is ballistic. For all temperatures, one can see that a peak emerges in the momentum distribution. The height of the peak increases with time and its position approaches $k = \pi/2$ [133]. As the temperature increases, from Fig. 5.6(d) to 5.6(f), the peak becomes wider and its height decreases. The emergence of the peak during the expansion indicates that the system develops off-diagonal one-body correlations. They appear to weaken as the initial temperature is increased.

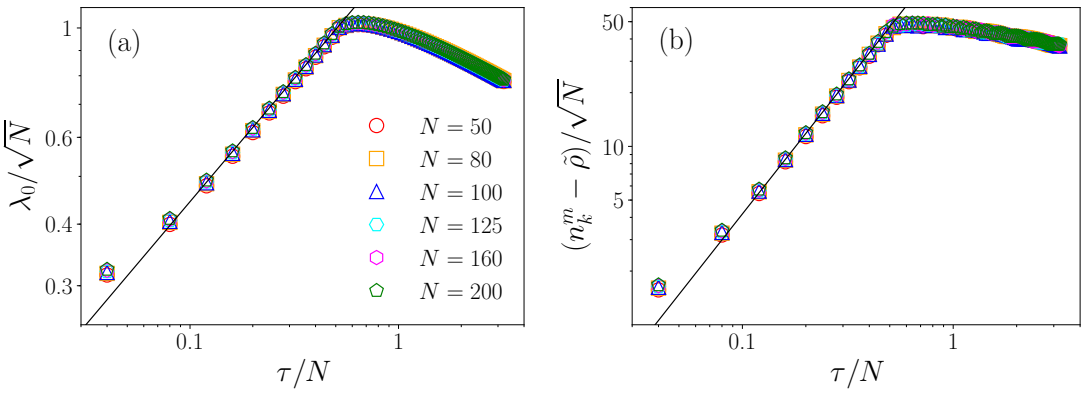

Figure 5.7: Scaling behavior of (a) the lowest natural orbital occupations and (b) the highest occupied momentum modes $(n_k^m - \tilde{\rho})/\sqrt{N}$ as functions of τ/N from initial ground state of Hamiltonian Eq. (5.1) with linear traps and $\tilde{\rho} = 25$. Results for different system sizes with the same initial characteristic densities $\tilde{\rho}$ are shown. The black lines are fits to the plots with powers 0.5 and 1.5 respectively.

During the melting of a perfect Mott insulator with one particle per site, which is the $T = 0$ and $V_1 = \infty$ limit of our setup, the lowest natural orbital (the highest occupied one) exhibits occupations $\lambda_0(\tau) \propto \sqrt{\tau}$ [88, 90]. It reaches a maximum shortly after no sites with occupation one remain in the system, and then starts to decrease slowly. For initial ground state with a finite superfluid ring, as shown in Fig. 5.7(a), $\lambda_0(\tau)$ starts with a slow increase and $\lambda_0(\tau) \propto \sqrt{\tau}$ for large τ. The maximum values reached depend on the number of particles: $[\lambda_0]_{\max} \propto \sqrt{N}$ and occur at a time that increases linearly with N [88, 90]. This

means that at $T = 0$ there exists a scaling solution to $\lambda_0(\tau)/\sqrt{N}$ as a function of τ/N. The same power-law growth can be recovered in the highest occupied momentum mode, by removing the contribution from the Mott domain to the momentum distribution, which is included in the Fourier transformation of diagonal terms of the one-body density $\sum_i \rho_{ii}/R = N/R = \tilde{\rho}$. With an overall increase of number of particle in the superfluid domain proportional to $\sqrt{1 + (V_1\tau)^2}$, the growth of the scaled momentum peak $n_k^m(\tau) - \tilde{\rho} \propto \sqrt{\tau[1 + (\tilde{\rho}\tau/N)^2]}$. For initial large $\tilde{\rho}$, as the case shown in Fig. 5.7(b), a similar scaling solution exists for $n_k^m(\tau) - \tilde{\rho}$, with $(n_k^m(\tau) - \tilde{\rho})/\sqrt{N} \propto (\tau/N)^{3/2}$. The universal behaviors break down at nonzero temperature. However, in the early times of the expansion, $\lambda_0(\tau) \approx \text{const}\sqrt{\tau}$ and $(n_k^m(\tau) - \tilde{\rho}) \approx \text{const}\sqrt{\tau}$.

In Fig. 5.8, we plot $[n_k^m]_{\max}$ [Fig. 5.8(a)] and $[\lambda_0]_{\max}$ [Fig. 5.8(b)] vs N for different initial temperatures. As in the previous section, when N is increased V_1 is decreased so that $\tilde{\rho} = NV_1$ remains constant in the initial state. At $T = 0$, $[n_k^m]_{\max}$ and $[\lambda_0]_{\max}$ display a power-law increase with N at large N (with exponent 1/2). For nonzero initial temperatures, $[n_k^m]_{\max}$ and $[\lambda_0]_{\max}$ still can be seen to increase with N. One can wonder whether this growth is consistent with the growth of $n_{k=0}$ and λ_0 in the initial thermal equilibrium state. In Fig. 5.8, we also report results for the latter quantities in a box trap at half-filling at the initial temperatures of the systems that undergo the expansion. For $T = 0$, the equilibrium results closely follow those of the dynamics for large N. However, for nonzero temperature, both $n_{k=0}$ and λ_0 in equilibrium exhibit a much slower growth and saturate for large N. This indicates that if an effective thermal equilibrium description of the expansion is possible, it will likely involve lower temperatures than those of the initial state.

5.3.2 Emergent eigenstate solution

In the thermodynamic limit, an exact description of the dynamics discussed in the previous subsection can be obtained using the emergent local Hamiltonian introduced in Ref. [133]. There it was shown that the time-evolving state generated by the expansion of the ground state of Hamiltonian (5.1), with $\alpha = 1$ (linear potential), is the ground state of the following emergent Hamiltonian

$$\hat{\mathcal{H}}(\tau) = -\mathcal{A}(\tau) \sum_l (e^{i\varphi(\tau)} \hat{f}_{l+1}^\dagger \hat{f}_l + \text{H.c.}) + V_1 \sum_l l\, \hat{n}_l \tag{5.20}$$

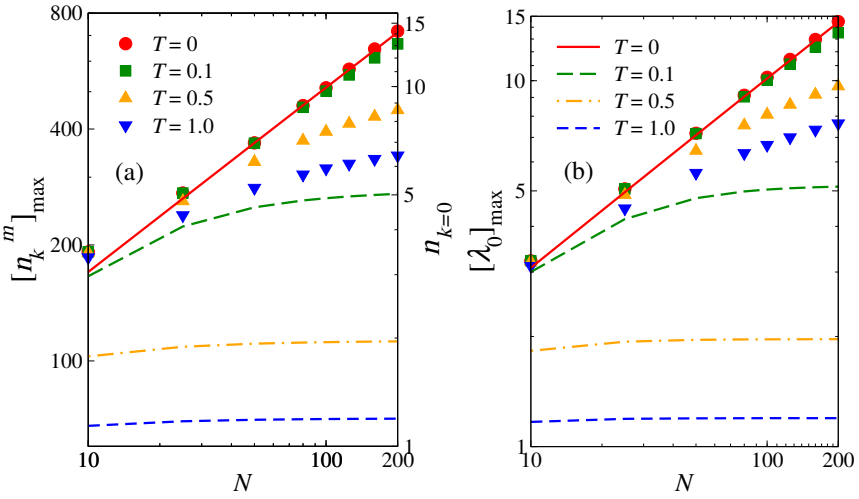

Figure 5.8: Maximal values (a) $[n_k^m]_{\max}$ and (b) $[\lambda_0]_{\max}$ during the expansion (symbols) as a function of the number of bosons in the system. The calculations are done for initial states with constant $\tilde{\rho} = 50$, and different $T = 0.1$, 0.5 and 1.0. We also report the occupation of: (a) the zero-momentum mode $n_{k=0}$ (labels on the right), and (b) the lowest natural orbital λ_0, in homogeneous lattices with open boundary conditions at half-filling (lines) at the same initial temperatures of the systems that undergo expansion.

where the effective hopping amplitude is

$$\mathcal{A}(\tau) = J\sqrt{1 + (V_1\tau)^2}\,, \tag{5.21}$$

and the time-dependent phase is

$$\varphi(\tau) = \arctan\left(V_1\tau\right)\,. \tag{5.22}$$

The same applies to excited states, so long as they contain a region with site occupation one in the left edge of the system and zero in the right one. Hence, the emergent local Hamiltonian can be used to describe finite-temperature initial states if the temperature is not too high. The regime of validity extends to higher temperatures with increasing the initial value of V_1.

The description in terms of the emergent Hamiltonian (5.20) makes apparent why an effective cooling is taking place in the system. The initial temperature sets which eigenstates of the initial Hamiltonian are involved in the dynamics. Hence, T does not depend on τ in the emergent local Hamiltonian description. On the

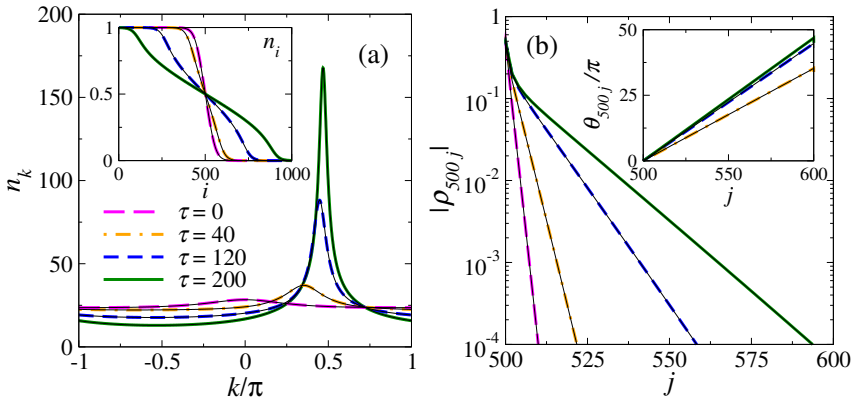

Figure 5.9: Comparison between the emergent local Hamiltonian description [lines in the legend in panel (a)] and the exact results from the dynamics (thin continuous lines). The calculations were done in a system with $N = 500$, an initial potential with $V_1 = 0.05$, and $T = 1.0$, and results are reported for four times. (a) Momentum distributions (main panel) and site occupation profiles (inset). (b) Absolute values of one-body correlations measured from site 500 (main panel) and the corresponding phases (inset).

other hand, the effective hopping amplitude $\mathcal{A}(\tau)$ increases with time. This results in a ratio between T and $\mathcal{A}(\tau)$ that decreases with time. One can think of the time evolving state as a thermal equilibrium state with temperature

$$T_{\rm eff}(\tau) = T/\sqrt{1 + (V_1\tau)^2}\ . \tag{5.23}$$

in the following effective Hamiltonian:

$$\hat{\mathcal{H}}_{\rm eff}(\tau) = -\sum_l (e^{i\varphi(\tau)}\hat{f}^\dagger_{l+1}\hat{f}_l + {\rm H.c.}) + V_1(\tau)\sum_l l\,\hat{n}_l\ , \tag{5.24}$$

where $V_1(\tau) = V_1/\mathcal{A}(\tau) = V_1/\sqrt{1 + (V_1\tau)^2}$. This means that if at time τ after the initial linear potential has been turned off, one suddenly quenches the Hamiltonian from the free Hamiltonian $\hat{H}_0$ dictating the dynamics to $\hat{\mathcal{H}}_{\rm eff}(\tau)$, all evolution will stop as the system will be in a thermal equilibrium state of $\hat{\mathcal{H}}_{\rm eff}(\tau)$ with temperature $T_{\rm eff}(\tau)$. This is something that could potentially be done in experiments with ultracold quantum gases to test the validity of the emergent Hamiltonian description.

In Fig. 5.9(a), we compare the exact results obtained from the quantum dynamics for the momentum distribution (main panel) and the site occupations (inset) with

those obtained using the emergent local Hamiltonian description from Eqs. (5.23) and (5.24). The results from both calculations are indistinguishable from each other. In the main panel in Fig. 5.9(b), we compare the results from the exact dynamics and the effective equilibrium description for the absolute value of one-body correlations. They are also identical, and exhibit an exponential decay with a correlation length that increases with τ, as expected from the emergent local Hamiltonian description. The latter also allows one to understand why the position of the momentum peak moves toward larger values of k. This is the result of the change of the phase (5.22) with τ [133]. The inset in Fig. 5.9(b) shows the phase, from $\rho_{lj} = |\rho_{lj}|e^{i\theta_{lj}}$ for $l = 500$, corresponding to the absolute values in the main panel. One can see that θ_{lj} increases linearly with the distance $l - j$ and that the slope increases with τ.

As mentioned before, the effective equilibrium description based on Eqs. (5.23) and (5.24) applies only while there are sites with occupation one in the left boundary of the chain and zero in the right one [133]. Thus the minimum effective temperature is determined by Eq. (5.23) at the time τ_c at which the occupation in the leftmost (rightmost) site departs from one (zero). If we assume that $L > 2N$, the occupation of the leftmost site will depart from one before the occupation of the rightmost one departs from zero. Because of the Lieb-Robinson bound, the time for the former to occur increases linearly with N. Since the appropriate thermodynamic limit requires $\tilde{\rho} = V_1 N$ =const, the minimum effective temperature is given by $T_{\text{eff}}^{\min} = T/\sqrt{1 + (\tilde{\rho}\tau_c/N)^2}$. Thus $T_{\text{eff}}^{\min}$ is size independent when N is large enough. The behavior of $[\lambda_0]_{\max}$ and $[n_k^m]_{\max}$ depicted in Fig. 5.8 can be reproduced with the effective thermal equilibrium state with $T_{\text{eff}}^{\min}$.

5.3.3 Reference Hamiltonian

Another, maybe more intuitive, way to understand the behavior observed during the expansion of the Mott domains of hard-core bosons is to think of the dynamical state as a thermal equilibrium state in a boosted reference frame, an idea that was explored in Ref. [93] in the context of the expansion of ground-state Mott insulators in the Fermi-Hubbard model. In this picture, the effective cooling in the dynamical system can be understood to be the result of internal energy being converted into center-of-mass energy, leading to a continuous reduction of the internal energy in

the reference frame.

In order to construct the reference Hamiltonian $\hat{H}_{\rm ref}$ in the comoving frame, one needs to modify the Hamiltonian dictating the dynamics by introducing a site-dependent potential of strength $\epsilon_l(\tau)$ to reproduce exactly the site occupations at time τ. For the expansion from the ground state, such a reference Hamiltonian was constructed in Ref. [176]

$$\hat{H}_{\rm ref} = -J\sum_l (\hat{f}^\dagger_{l+1}\hat{f}_l + {\rm H.c.}) + V_1(\tau)\sum_l l\,\hat{n}_l\ . \tag{5.25}$$

It is nothing but the Hamiltonian in Eq. (5.24) without the time-dependent phases in the hopping terms. Those phase factors do not alter the properties of observables such as the site occupations.

For initial states at finite temperature, the effective temperature in the reference system is identical to the time-dependent effective temperature in the context of the emergent local Hamiltonian; see Eq. (5.23). In Fig. 5.10(a), we show the momentum distribution in the reference frame and in the expanding system. The peaks can be seen to be shifted by a time-dependent momentum. In the reference frame, the momentum distribution is symmetric about $k = 0$. In Fig. 5.10(b), we

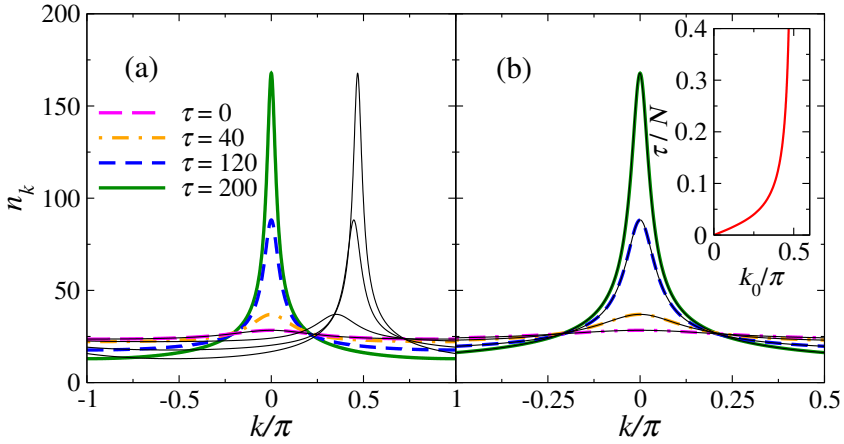

Figure 5.10: (a) Momentum distributions in the reference system [lines in the legend in panel (a)] compared to those during the expansion [thin lines, see also Fig. 5.9(a)]. (b) Results after shifting n_k during the expansion by the peak momentum k_0. (Inset) Peak momentum k_0 as a function of time. The calculations were done in a system with $N = 500$, an initial potential with $V_1 = 0.05$, and $T = 1.0$, and results are reported for four times (see also Fig. 5.9).

show the results in the reference frame and in the expanding system after shifting the momentum distribution of the latter by the momentum $k_0(\tau)$ of the maximum of n_k, which is determined by the phase in Eq. (5.24): $k_0(\tau) = \varphi(\tau) = \arctan(V_1\tau)$ [133]. The distributions are now indistinguishable from each other. The dependence of k_0 on τ for this particular setup is shown in the inset in Fig. 5.10(b).

Chapter 6

Emergent Eigenstate Solution to Expansion Dynamics

In the quantum quenches studied in Ref. [133], the initial states were eigenstates of Hamiltonians that contained the so-called boost operator (an operator that is used in integrable models to generate conserved quantities). While such Hamiltonians could potentially be engineered in optical lattice experiments, they are not directly relevant to current experiments. Our first goal in this chapter is to show that the emergent eigenstate solutions also exist for quenches that do not involve the boost operator. Our second goal is to formalize the numerical observation in Chapter 5 that the emergent local Hamiltonian can be used to understand the dynamics of thermal states after a quench. We justify analytically, and show numerically, the applicability of an emergent Gibbs ensemble (a Gibbs ensemble for the emergent local Hamiltonian) for quenches starting from Gibbs states.

We study bosons in the Tonks-Girardeau regime [8, 9, 11, 50] in 1D lattices, and consider systems that are initially at zero and nonzero temperatures confined in power-law traps (harmonic traps are the ones relevant to current experiments). The physical phenomenon that will be central to our discussions is the dynamical fermionization of the quasimomentum distribution function during the expansion after suddenly turning off the trap [31, 89, 90, 182]. In closing, by comparing results for power-law traps with even and odd exponents (for spectra that are bounded and unbounded from below, respectively), we show that different emergent local Hamiltonians can be used to describe dynamics of the same states, and that the target eigenstates can be ground states or highly excited states of such Hamiltonians.

6.1 Emergent Eigenstate Solution

We first review some key elements of the emergent eigenstate solution to quantum dynamics introduced in Ref. [133]. We consider a quantum quench from the initial Hamiltonian $\hat{H}_0$ to the final Hamiltonian $\hat{H}$, with the initial state $|\psi_0\rangle$ being an eigenstate of $\hat{H}_0$ ($\hat{H}_0|\psi_0\rangle = \lambda|\psi_0\rangle$). The time-evolving state $|\psi(t)\rangle = e^{-i\hat{H}t}|\psi_0\rangle$ is an eigenstate $\hat{\mathcal{M}}(t)|\psi(t)\rangle = 0$ of the operator

$$\hat{\mathcal{M}}(t) \equiv e^{-i\hat{H}t}\hat{H}_0 e^{i\hat{H}t} - \lambda\,, \tag{6.1}$$

which is in general nonlocal and therefore of no particular interest (we set $\hbar = 1$). However, there are physically relevant cases for which $\hat{\mathcal{M}}(t)$ is a local operator, i.e., an extensive sum of operators with support on a finite number of lattice sites [133]. We say that the emergent eigenstate solution to quantum dynamics exists whenever $\hat{\mathcal{M}}(t)$ can be replaced by a local operator $\hat{\mathcal{H}}(t)$ that we call the emergent local Hamiltonian. Since $\hat{\mathcal{H}}(t)|\psi(t)\rangle = 0$, instead of time-evolving the initial state one can solve for the dynamics by finding a single eigenstate of $\hat{\mathcal{H}}(t)$. Remarkably, $\hat{\mathcal{H}}(t)$ is time independent in the Heisenberg picture [$\langle\psi(t)|\hat{\mathcal{H}}(t)|\psi(t)\rangle = 0$]. Hence, $\hat{\mathcal{H}}(t)$ is a local conserved quantity even though it does not commute with the physical Hamiltonian that governs the dynamics.

The conditions for $\hat{\mathcal{H}}(t)$ to exist become apparent from the expansion of Eq. (6.1) in power series

$$e^{-i\hat{H}t}\hat{H}_0 e^{i\hat{H}t} = \hat{H}_0 + \sum_{n=1}^{\infty}\frac{(-it)^n}{n!}\hat{\mathcal{H}}_n\,, \tag{6.2}$$

where $\hat{\mathcal{H}}_n = [\hat{H}, ...[\hat{H}, [\hat{H}, \hat{H}_0]]...]$ is an n-th nested commutator of the final Hamiltonian with the initial Hamiltonian. An emergent local Hamiltonian exists if: (i) $\hat{\mathcal{H}}_n$ vanishes at some finite n_0, or (ii) if the nested commutators close the sum in Eq. (6.2).

6.2 Emergent Gibbs Ensemble

One can generalize the emergent eigenstate solution of quantum dynamics to initial thermal states. For an initial density matrix $\hat{\rho}_0 = e^{-\beta\hat{H}_0}/Z_0$, where $Z_0 = \mathrm{Tr}\{e^{-\beta\hat{H}_0}\}$ and $\beta = T^{-1}$ is the initial inverse temperature (we set $k_\mathrm{B} = 1$), the time-evolving

density matrix is

$$\begin{aligned}\hat{\rho}(t) &= Z_0^{-1} e^{-i\hat{H}t} e^{-\beta\hat{H}_0} e^{i\hat{H}t} \\ &= Z_0^{-1} \sum_{n=0}^{\infty} \frac{(-\beta)^n}{n!} e^{-i\hat{H}t} \left(\hat{H}_0\right)^n e^{i\hat{H}t}\,, \end{aligned} \tag{6.3}$$

where, in the second line, the operator $e^{-\beta\hat{H}_0}$ was expanded in a power series. Writing $e^{-i\hat{H}t}(\hat{H}_0)^n e^{i\hat{H}t} = (e^{-i\hat{H}t}\hat{H}_0 e^{i\hat{H}t})^n$ yields

$$\hat{\rho}(t) = Z_0^{-1} \exp\left(-\beta \left[e^{-i\hat{H}t}\hat{H}_0 e^{i\hat{H}t}\right]\right)\,. \tag{6.4}$$

In Eq. (6.4), one can introduce the operator $\hat{\mathcal{M}}(t) \equiv e^{-i\hat{H}t}\hat{H}_0 e^{i\hat{H}t}$ such that the time-evolving density matrix $\hat{\rho}(t)$ is a Gibbs density matrix of $\hat{\mathcal{M}}(t)$. $\hat{\mathcal{M}}(t)$ is in general nonlocal and, hence, of no particular use. However, whenever $\hat{\mathcal{M}}(t)$ is local [$\hat{\mathcal{M}}(t) \equiv \hat{\mathcal{H}}(t)$], Eq. (6.4) represents a physically meaningful emergent Gibbs ensemble

$$\hat{\Sigma}(t) = Z_0^{-1} e^{-\beta\hat{\mathcal{H}}(t)}\,. \tag{6.5}$$

Note that the temperature in $\hat{\Sigma}(t)$ is that of the initial state, only the emergent local Hamiltonian changes with time. The expectation value of any observable $\hat{O}$ during the dynamics can be computed as $\langle\hat{O}(t)\rangle = \mathrm{Tr}\{\hat{\Sigma}(t)\hat{O}\}$.

6.3 Dynamical Fermionization

As mentioned before, here we study hard-core bosons in 1D lattices. We consider initial Hamiltonians of the form:

$$\hat{H}^{(\alpha)}_{0,\mathrm{HCB}} = -J \sum_{l=-L_0}^{L_0-1} \left(\hat{b}^\dagger_{l+1}\hat{b}_l + \mathrm{H.c.}\right) + \frac{J}{R^\alpha} \sum_{l=-L_0}^{L_0} l^\alpha\, \hat{b}^\dagger_l \hat{b}_l\,, \tag{6.6}$$

where $\hat{b}^\dagger_l$ ($\hat{b}_l$) is the creation (annihilation) operator of a hard-core boson at site l, J is the hopping amplitude, and J/R^α and α are the strength and exponent of the power-law trap, respectively. The quantity to be kept constant when taking the thermodynamic limit is the so-called characteristic density $\tilde{\rho} = N/R$ [44, 45], where N is the total number of particles in the trap.

Mapping hard-core bosons onto spins 1/2 and spins 1/2 onto fermions, $\hat{b}_l =$

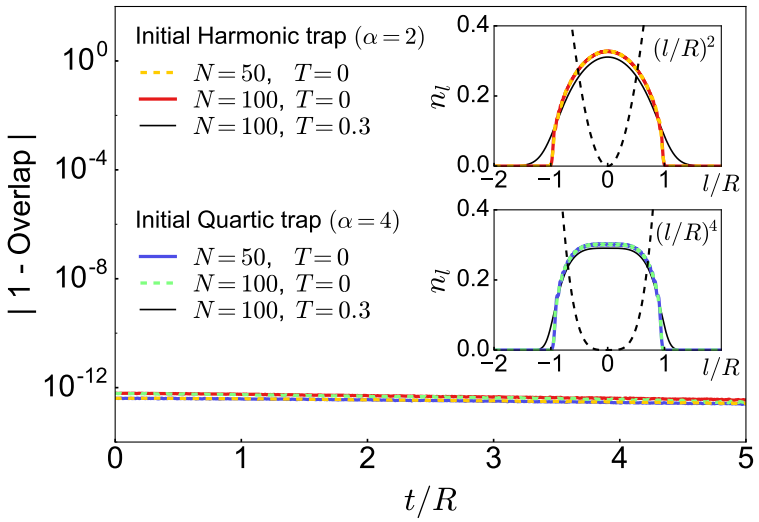

Figure 6.1: Initial site occupations and validity of the emergent eigenstate solution. (Insets) Initial site occupations in harmonic (top inset) and quartic (bottom inset) traps at zero and nonzero temperature. Results are shown for a characteristic density $\tilde{\rho} = N/R = 0.5$. (Main panel) Subtracted overlap $|1 - O(t)|$, where $O(t) = |\langle \Psi_t | \psi(t) \rangle|$, of the time-evolving state $|\psi(t)\rangle$ (for the $T = 0$ cases) with the ground state $|\Psi_t\rangle$ of the emergent local Hamiltonian $\hat{\mathcal{H}}^{(2)}(t)$ (6.13) and $\hat{\mathcal{H}}^{(4)}(t)$ (6.18).

$e^{i\pi \sum_{m<l} \hat{f}_m^\dagger \hat{f}_m} \hat{f}_l$ [2, 177, 183], Hamiltonian (6.6) maps onto a Hamiltonian of noninteracting spinless fermions

$$\hat{H}_0^{(\alpha)} = -J \sum_{l=-L_0}^{L_0-1} \left(\hat{f}_{l+1}^\dagger \hat{f}_l + \text{H.c.} \right) + \frac{J}{R^\alpha} \sum_{l=-L_0}^{L_0} l^\alpha \hat{f}_l^\dagger \hat{f}_l \,. \tag{6.7}$$

One can efficiently compute one-body observables of hard-core bosons solving for the fermions and using properties of Slater determinants [45, 46, 90, 182]. The site occupations of fermions $n_l = \langle \hat{n}_l \rangle$, with $\hat{n}_l = \hat{f}_l^\dagger \hat{f}_l$, and hard-core bosons are identical.

We first focus on the cases in which $\alpha = 2$ (harmonic trap) and $\alpha = 4$ (quartic trap). The insets in Fig. 6.1 show typical initial ground-state and finite-temperature ($T = 0.3J$) site occupations considered in our study. It is interesting to note that, in the center of the quartic trap, the site occupations are almost constant. Our quench consists of turning off the trap, so that the dynamics occur under the physical

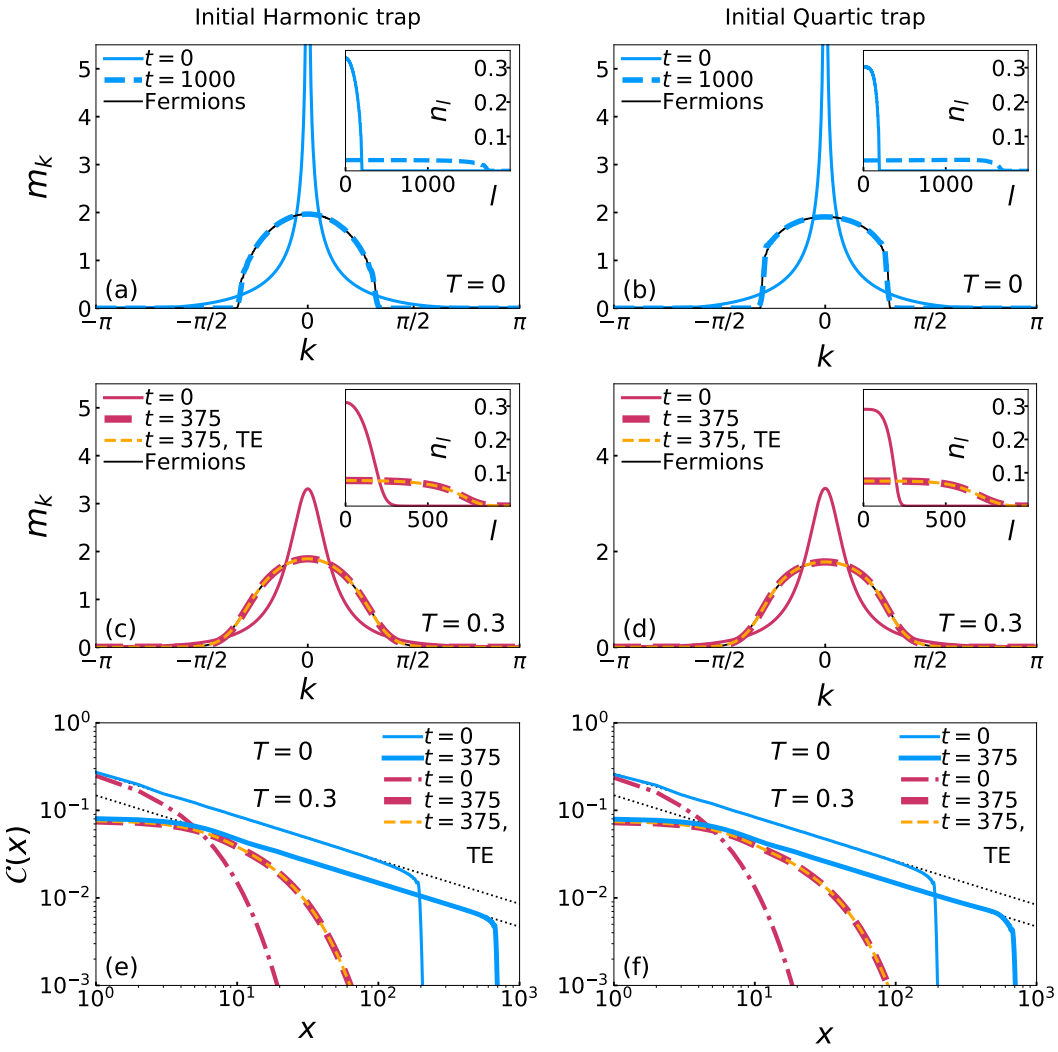

Figure 6.2: Dynamical fermionization of the hard-core boson momentum distribution function. All the results reported are obtained using the emergent local Hamiltonian $\hat{\mathcal{H}}^{(2)}(t)$ (6.13) [left panels] and $\hat{\mathcal{H}}^{(4)}(t)$ (6.18) [right panels]. The only exceptions are the thin dashed lines in (c)–(f), which depict results for the time evolution (TE) of thermal ($T = 0.3$) initial states. (a)–(d) Quasi-momentum distribution m_k (main panels) and site occupations n_l (insets) in the ground state of the emergent local Hamiltonian [(a),(b)] and in the emergent Gibbs ensemble [(c),(d)]. (e),(f) Absolute value of one-body correlations $\mathcal{C}(x) = |\langle b^\dagger_{l=0} \hat{b}_{l'=x}\rangle|$ in the ground state of the emergent local Hamiltonian and in the emergent Gibbs ensemble. Thin dotted lines are power-law fits to $\mathcal{C}(x) = ax^{-1/2}$ for the ground-state results in the interval $x \in [10, 100]$ at $t = 0$ and $x \in [50, 500]$ at $t = 375$. For the harmonic trap, we get $a = 0.270$ at $t = 0$ and $a = 0.148$ at $t = 375$, while for the quartic trap, we get $a = 0.264$ at $t = 0$ and $a = 0.149$ at $t = 375$. The results reported are for systems with $N = 100$ particles and a characteristic density $\tilde{\rho} = 0.5$.

Hamiltonian

$$\hat{H} = -J \sum_{l=-L_0}^{L_0-1} \left(\hat{f}_{l+1}^{\dagger} \hat{f}_l + \text{H.c.} \right) . \tag{6.8}$$

We measure time in units of $1/J$ and set $J \equiv 1$. This class of geometric quantum quenches is known as sudden expansion and has been widely studied theoretically [13, 88–90, 93, 118, 120–122, 125, 126, 129, 176, 181, 182, 184–195] and in experiments with ultracold atoms in optical lattices [112–115, 196]. In contrast to the standard time-of-flight measurements, the lattice potential and, as a result, strong interactions, are not switched off during the quench.

We now derive the emergent local Hamiltonian for this setup. Note that, in Ref [133], the initial and the final Hamiltonians satisfied the commutation relation $[\hat{H}, \hat{H}_0] \propto \hat{Q}$, with $\hat{Q}$ being a conserved quantity of the final Hamiltonian (up to boundary terms). Such a commutation relation was enforced by making $\hat{H}_0$ the sum of $\hat{H}$ and a boost operator. For $\alpha = 2$ and 4 [see Eq. (6.7)], the traps of interest here, this is not the case.

For the analysis that follows, it is useful to define the generalized kinetic energy $\hat{T}^{(m,\alpha)}$ and current $\hat{J}^{(m,\alpha)}$ operators

$$\hat{T}^{(m,\alpha)} = -R^{-\alpha} \sum_{l=-L_0}^{L_0-m} \left[\left(l + \frac{m}{2} \right)^{\alpha} \hat{f}_{l+m}^{\dagger} \hat{f}_l + \text{H.c.} \right] , \tag{6.9}$$

$$\hat{J}^{(m,\alpha)} = R^{-\alpha} \sum_{l=-L_0}^{L_0-m} \left[i \left(l + \frac{m}{2} \right)^{\alpha} \hat{f}_{l+m}^{\dagger} \hat{f}_l - \text{H.c.} \right] . \tag{6.10}$$

They allow us to write the initial Hamiltonian as $\hat{H}_0^{(\alpha)} = \hat{T}^{(1,0)} - \hat{T}^{(0,\alpha)}/2$, and the final Hamiltonian as $\hat{H} = \hat{T}^{(1,0)}$. Note that the operators $\hat{T}^{(m,0)}$ and $\hat{J}^{(m,0)}$ commute with $\hat{H}$, up to boundary terms. This is what ensures that the sum in Eq. (6.2) is convergent for our quenches of interest.

Let us consider first the initial harmonic confinement, $\alpha = 2$ in Eq. (6.7). The commutator of the final and the initial Hamiltonian yields

$$[\hat{H}, \hat{H}_0^{(2)}] = -2i\, R^{-1} \hat{J}^{(1,1)} . \tag{6.11}$$

While $\hat{J}^{(1,1)}$ does not commute with $\hat{H}$, their commutator yields the operators

$$[\hat{H}, \hat{J}^{(1,1)}] = -i\, R^{-1} \hat{T}^{(2,0)} + 2i\, R^{-1} \hat{N} , \tag{6.12}$$

with $\hat{N} = \sum_l \hat{n}_l$, which both commute with $\hat{H}$ (up to boundary terms). We therefore truncate the series in Eq. (6.2) at $n_0 = 2$. Consequently, the emergent local Hamiltonian for the initial harmonic trap reads

$$\hat{\mathcal{H}}^{(2)}(t) = \hat{H}_0^{(2)} - \lambda - \frac{2t}{R}\hat{J}^{(1,1)} + \left(\frac{t}{R}\right)^2 \hat{T}^{(2,0)} + \left(\frac{\sqrt{2}t}{R}\right)^2 \hat{N}\,. \tag{6.13}$$

Remarkably, when mapping spinless fermions back to hard-core bosons, the operator $\hat{T}^{(2,0)}$ in Eq. (6.13) becomes a two-body operator $-\sum_l (\hat{b}^\dagger_{l+2}[1 - 2\hat{b}^\dagger_{l+1}\hat{b}_{l+1}]\hat{b}_l + \text{H.c.})$. Hence, the emergent local Hamiltonian for hard-core bosons contains correlated next-nearest neighbor hoppings, even though the emergent local Hamiltonian for the corresponding fermions is quadratic.

The emergent local Hamiltonian to describe the expansion dynamics from other initial power-law traps, with $\alpha > 2$, can also be determined in a straightforward way. However, the calculations become increasingly lengthy with increasing α as the series in Eq. (6.2) is truncated at $n = \alpha$. For the quartic trap $\alpha = 4$, the emergent local Hamiltonian $\hat{\mathcal{H}}^{(4)}(t)$ is derived by evaluating elements $\hat{\mathcal{H}}^{(4)}_n$ of the series in Eq. (6.2). The first-order term is

$$\hat{\mathcal{H}}^{(4)}_1 = -iR^{-3}\hat{J}^{(1,1)} - 4i\,R^{-1}\hat{J}^{(1,3)}\,, \tag{6.14}$$

the second-order term is

$$\hat{\mathcal{H}}^{(4)}_2 = 24R^{-2}\hat{T}^{(0,2)} - 2R^{-4}\hat{T}^{(2,0)} - 12R^{-2}\hat{T}^{(2,2)} - 4R^{-4}\hat{N}, \tag{6.15}$$

the third-order term is

$$\hat{\mathcal{H}}^{(4)}_3 = 72i\,R^{-3}\hat{J}^{(1,1)} - 24i\,R^{-3}\hat{J}^{(3,1)}\,, \tag{6.16}$$

and the fourth-order term is

$$\hat{\mathcal{H}}^{(4)}_4 = 96R^{-4}\hat{T}^{(2,0)} - 24R^{-4}\hat{T}^{(4,0)} + 144R^{-4}\hat{N}\,. \tag{6.17}$$

One then realizes that $\hat{\mathcal{H}}^{(4)}_4$ commutes with $\hat{H}$ (up to boundary terms), and, hence, the series in Eq. (6.2) can be truncated at $n_0 = 4$. The resulting emergent local

Hamiltonian reads,

$$\begin{aligned}\hat{\mathcal{H}}^{(4)}(t) = \hat{H}_0^{(4)} - \lambda - 6\left(\frac{t}{R}\right)^2 \hat{T}^{(0,2)} + \left(\frac{t}{R}\right)^2 \left[4\left(\frac{t}{R}\right)^2 + R^{-2}\right] \hat{T}^{(2,0)} \\ + 6\left(\frac{t}{R}\right)^2 \hat{T}^{(2,2)} - \left(\frac{t}{R}\right)^4 \hat{T}^{(4,0)} - \frac{t}{R}\left[12\left(\frac{t}{R}\right)^2 + R^{-2}\right] \hat{J}^{(1,1)} \\ - 4\left(\frac{t}{R}\right) \hat{J}^{(1,3)} + 4\left(\frac{t}{R}\right)^3 \hat{J}^{(3,1)} + 2\left(\frac{t}{R}\right)^2 \left[3\left(\frac{t}{R}\right)^2 + R^{-2}\right] \hat{N}\,,\end{aligned} \tag{6.18}$$

which is significantly more complex than $\hat{\mathcal{H}}^{(2)}(t)$. However, it still consists of sums of local operators.

The emergent local Hamiltonian construction implies that if the initial state is the ground state of $\hat{H}_0^{(\alpha)}$ (6.7) [for α even and positive] and $\hat{\mathcal{H}}^{(\alpha)}(t)$ is nondegenerate, the time-evolving state $|\psi(t)\rangle$ is the ground state of $\hat{\mathcal{H}}^{(\alpha)}(t)$ at all times, which we denote as $|\Psi_t\rangle$. This statement is not limited to a particular initial characteristic density $\tilde{\rho}$. We check this numerically for $\alpha = 2$ and 4, and $\tilde{\rho} = 0.5$ in Fig. 6.1 by calculating the overlap $O(t) = |\langle\Psi_t|\psi(t)\rangle|$. The overlap is essentially one to machine precision. This confirms that, if the lattice is sufficiently large such that the site occupations at the edges vanish at all times, the emergent eigenstate solution is valid at all times. In the derivation of $\hat{\mathcal{H}}^{(2)}(t)$ and $\hat{\mathcal{H}}^{(4)}(t)$, we neglected boundary terms that appear in the commutators $\hat{\mathcal{H}}_n$. These terms enter the series in Eq. (6.2) generating operators at the lattice boundaries whose support increases with the power of t, and eventually result in a breakdown of the emergent eigenstate description of the dynamics on finite lattices and long times. Physically, the breakdown time can be understood to be the time at which propagating particles reach the lattice boundaries [133]. Hence, by taking limits appropriately, no breakdown of the emergent eigenstate solution will occur. One needs to first take the lattice size to infinity while keeping the time fixed, and then take the infinite time limit. Moreover, Figs. 6.2(c)–6.2(f) show results for various one-body observables for initial finite-temperature states, obtained both by time-evolving the initial density matrix (as in Ref. [182]) and by using the emergent Gibbs ensemble. The results can be seen to agree, which demonstrates the validity of the emergent Gibbs ensemble description [see Eq. (6.5)].

Physically, the quench dynamics under investigation is of particular interest because the quasimomentum distribution of hard-core bosons undergoes a dynam-

ical fermionization, namely, it approaches that of spinless fermions as the cloud expands [89]. (Note that the quasimomentum distribution of the spinless fermions does not change in time because the fermionic occupations of the quasimomentum modes are conserved quantities.) This dynamical fermionization is to be contrasted to the result of the time-of-flight protocol, in which all the external potentials are switched off and the measured momentum distribution after expansion is, up to higher-order Bragg peaks, the same as the initial quasimomentum distribution of the hard-core bosons. Dynamical fermionization has been studied for hard-core bosons in initial ground states in a lattice [89, 90], in the continuum [31], and at finite temperatures in a lattice [182].

Figures 6.2(a)–6.2(d) display the quasimomentum distribution m_k for $\alpha = 2$ and 4. We define m_k of hard-core bosons as $m_k = (1/R)\sum_{l,l'} e^{ik(l-l')}\langle \hat{b}_l^\dagger \hat{b}_{l'}\rangle$ (for spinless fermions, one just needs to replace $\hat{b}_l^\dagger \hat{b}_{l'}$ by $\hat{f}_l^\dagger \hat{f}_{l'}$). In equilibrium, m_k of hard-core bosons is clearly different from its spinless fermion counterpart: it is sharply peaked at $k = 0$ in the ground state [Figs. 6.2(a) and 6.2(b)], while finite temperatures [Figs. 6.2(c) and 6.2(d)] smoothen the peak [46]. Remarkably, during the dynamics [see Figs. 6.2(a)–6.2(d)], m_k of hard-core bosons approaches the one of spinless fermions irrespective of the initial temperature [182] and of the exponent of the initial confining potential. The quasimomentum distribution of hard-core bosons is nearly identical to that of the fermions at the longest expansion times studied, when the occupations n_l in the center of the lattice are strongly reduced from their initial values [see the insets of Figs. 6.2(a)-6.2(d)].

The dynamical fermionization of the bosonic quasimomentum distribution function is not the only intriguing phenomenon that occurs during the expansion dynamics. Another remarkable feature is the preservation of coherence in the many-body wavefunction of pure states. This can be seen by studying the spatial decay of the absolute value of one-body correlations $\mathcal{C}(x) = |\langle \hat{b}_{l=0}^\dagger \hat{b}_{l'=x}\rangle|$, for which results are depicted in Figs. 6.2(e) and 6.2(f). While the spatial decay for finite-temperature initial states is exponential [182], it is intriguing that for initial ground states the correlations retain a power-law decay with the ground-state exponent $\mathcal{C}(x) \propto x^{-1/2}$ at all times [89, 90]. The fact that the expanding states that start their dynamics from ground states are eigenstates of emergent local Hamiltonians (6.13) and (6.18) allow one to gain an intuitive understanding for why correlations can be power law. This is a behavior typical of gapless 1D systems in their ground states, which are

described by the Luttinger-liquid theory [2].

6.4 Nonuniqueness of the Emergent Local Hamiltonian

Before concluding, let us also consider initial Hamiltonians of the form

$$\hat{H}_0'^{(\alpha)} = \sum_{l=-L_0}^{L_0} l^\alpha \hat{n}_l \,, \tag{6.19}$$

which commute for different values of α. Let us consider two initial Hamiltonians $\hat{H}_0'^{(\alpha_1)}$ and $\hat{H}_0'^{(\alpha_2)}$ and the same final Hamiltonian $\hat{H}$ after the quench. The corresponding emergent local Hamiltonians $\hat{\mathcal{H}}'^{(\alpha_1)}(t)$ and $\hat{\mathcal{H}}'^{(\alpha_2)}(t)$ commute [this follows from Eq. (6.1)], i.e., they share eigenstates. This means that different emergent local Hamiltonians can be used to describe dynamics from initial states that are common eigenstates of $\hat{H}_0'^{(\alpha_1)}$ and $\hat{H}_0'^{(\alpha_2)}$.

An interesting aspect about the nonuniqueness of the emergent local Hamiltonian appears when studying $\hat{H}_0'^{(\alpha)}$ for even and odd values of α, as the former (latter) exhibits a spectrum that is bounded (unbounded) from below. If one considers an initial state that is a Fock state with one particle per site in the center of the lattice, see the insets in Fig. 6.3, that state is the ground state of $\hat{H}_0'^{(2)}$ and $\hat{H}_0'^{(4)}$, while it is a highly-excited (degenerate) eigenstate of $\hat{H}_0'^{(1)}$. As a result, the expansion dynamics can be described using the ground state of $\hat{\mathcal{H}}'^{(2)}(t)$ and $\hat{\mathcal{H}}'^{(4)}(t)$ [obtained by replacing $\hat{H}_0^{(\alpha)} \to \hat{H}_0'^{(\alpha)}$ and $R \to 1$ in Eqs. (6.13) and (6.18), respectively] or using a highly-excited eigenstate of

$$\hat{\mathcal{H}}'^{(1)}(t) = \hat{H}_0'^{(1)} - t\,\hat{J}^{(1,0)} - \lambda \,, \tag{6.20}$$

with $\lambda = 0$ [133]. In the main panel in Fig. 6.3, we show overlaps between the target eigenstates of $\hat{\mathcal{H}}'^{(1)}(t)$, $\hat{\mathcal{H}}'^{(2)}(t)$, and $\hat{\mathcal{H}}'^{(4)}(t)$ as a function of time. The overlaps are one within machine precision for all times shown.

This example offers an understanding for why one-body correlations with ground-state character can be found in highly-excited eigenstates of emergent local Hamiltonians with spectra that are unbounded from below [133]. In the case

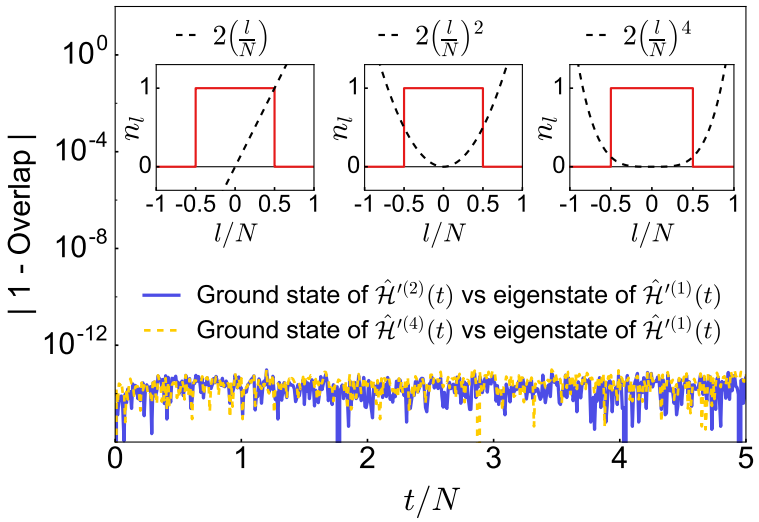

Figure 6.3: Nonuniqueness of the emergent local Hamiltonian. We consider an initial product state $|\psi_0\rangle = \prod_{l\in L_c} \hat{b}_l^\dagger |\emptyset\rangle$, where the particles occupy L_c consecutive sites in the center of the lattice. This state is an eigenstate of $\hat{H}_0'^{(1)}$, $\hat{H}_0'^{(2)}$, and $\hat{H}_0'^{(4)}$ (see insets for the corresponding site occupations). In the quench, the trap is turned off and hopping between nearest neighbor sites is turned on. As a result, a highly excited eigenstate of the emergent local Hamiltonian $\hat{\mathcal{H}}'^{(1)}(t)$ is identical to the ground states of $\hat{\mathcal{H}}'^{(2)}(t)$ and $\hat{\mathcal{H}}'^{(4)}(t)$, as shown in the main panel by the vanishing values of the subtracted overlap between these states. Results are reported for systems with $N = 100$ and $L = 2500$.

considered here, a highly-excited eigenstate of $\hat{\mathcal{H}}'^{(1)}(t)$ is the ground state of $\hat{\mathcal{H}}'^{(2)}(t)$ and $\hat{\mathcal{H}}'^{(4)}(t)$. Note that, actually, a macroscopic number of low-energy eigenstates of $\hat{\mathcal{H}}'^{(2)}(t)$ and $\hat{\mathcal{H}}'^{(4)}(t)$ appears (is "cloned") in the middle of the spectrum of $\hat{\mathcal{H}}'^{(1)}(t)$.

Chapter 7

Conclusions

In this dissertation, we applied two main numerical techniques to study equilibrium and non-equilibrium properties of 1D strongly-interacting bosons in optical lattices. We used the path integral Monte Carlo in continuous space with worm algorithm to study one-body correlations of Lieb-Liniger gases and phase diagrams of bosons with an underlying periodic lattice. We also implemented an exact lattice approach based on the Bose-Fermi mapping, and by utilizing the properties of Slater determinants, we studied both equilibrium properties and far-from-equilibrium dynamics of hard-core bosons on lattices. In the following, we summarize the most important results from our work.

In Chapter 3, we carried out an unbiased study of 1D trapped bosons in the ground state and at finite temperature using the worm algorithm, and the Bose-Fermi mapping in the presence of a lattice at low fillings. Whenever possible, we compared our results to the predictions of the Bethe ansatz, obtaining an excellent agreement.

Our study focused on the behavior of the density and momentum distribution functions, as well as one-particle correlations. We discussed in detail how to scale density and momentum profiles to observe universal behavior, which was demonstrated by our numerical results. For trapped systems in the ground state, we showed that fixing γ in the center of the trap is all that is required to obtain a universal scaling of density and momentum profiles. This is to be contrasted with the Bose-Hubbard model, for which one needs to fix the so-called characteristic density and the on-site interaction strength [156]. At finite temperature in systems in the continuum, in addition to the condition for the ground state, one needs to

fix the scaled temperature in the center of the trap. Those two parameters fully characterize the densities and momentum distribution functions.

In our study of the momentum distribution function, we paid special attention to the k^{-4} asymptotic behavior at high momenta. As shown by our numerical calculations, those momentum tails become increasingly challenging to resolve as the temperature increases and the interactions become weaker, making the Tonks-Girardeau limit at low temperatures the ideal regime for their experimental observation.

In Chapter 4, we presented a careful study of the transitions from superfluid to Mott insulator phases due to the effect of an underlying lattice, specifically we focused on the incommensurate transition. We used two indicators, i.e., a finite-size scaling of the superfluid fraction and the exponential decay of the zero-momentum Green's function, to locate the phase boundaries. We computed the phase diagrams by changing the lattice depth and keeping the interaction strength constant. Our *ab initio* calculations show that, for $n \lesssim 1$, the one-band Bose-Hubbard model remains useful as an effective theory far into the multiband regime – provided that its parameters are properly renormalized to account for the contributions of the excited bands. Here, the renormalized parameters are obtained from an inverse confined scattering analysis. For $n \gtrsim 2$ and $\gamma > 1/2$, our results highlight the need for a more refined effective theory than the traditional one-band Hubbard model. Having found experimentally relevant regimes [64, 114] in which the traditional Bose-Hubbard model fails, our study is a first step in the needed exploration of beyond Bose-Hubbard model physics in 1D lattices in the presence of strong interactions and/or high fillings. Previous studies of extended Bose-Hubbard models [72] provide candidates beyond the conventional Bose-Hubbard model, and our *ab initio* results can be used to benchmark such effective models.

In Chapter 5, we extended the finite-temperature equilibrium method (developed for lattice hard-core bosons based on the Bose-Fermi mapping) to study the sudden expansion of hard-core bosons in thermal equilibrium in 1D lattices. For low initial site occupations, we showed that the expansion is self-similar and that the momentum distribution fermionizes at long times. This had been shown to occur during the expansion from initial ground states in Refs. [31, 89]. In addition, we showed that the natural orbital occupations almost do not change in time (they exhibit the characteristic η^{-4} behavior of systems in thermal equilibrium) and

are distinctively different from those of noninteracting fermions. This means that the natural orbital occupations can be used to distinguish hard-core bosons from fermions even after the momentum distribution of the former has fermionized.

For the expansion from an initial Mott insulator, we showed that the enhancement of one-body correlations known from studies of pure states [88] is robust against nonzero initial temperatures. However, increasing the temperature does weaken those correlations, and results in smaller peaks in the momentum distribution. Remarkably, the expansion leads to an effective cooling, namely, the system can be described by effective thermal equilibrium states with a correlation length that increases with time. We discussed two related ways to understand this phenomenon, one in terms of an emergent local Hamiltonian and the second one in terms of a thermal equilibrium state in a boosted reference frame. Our results explain why experiments with ultracold gases, such as the ones in Ref. [115], should be able to observe large momentum peaks in n_k even if the initial states are not in the ground state.

In Chapter 6, we formalized the application of the emergent local Hamiltonian to understand the dynamics after quenches from thermal states, for which we introduced the concept of *emergent Gibbs ensemble*. We tested the emergent eigenstate solutions by numerically studying the dynamical fermionization of hard-core boson quasimomentum distribution functions after turning off power-law confining potentials. Those quenches do not involve the boost operator, which was central to the discussion in Ref. [133]. Our construction is applicable independently of the characteristic density chosen, the exponent of the power-law traps, the initial temperature, and for arbitrarily long times, so long as particles do not reach the edges of the lattice. The emergent local Hamiltonians constructed provide a promising tool to manipulate time-evolving states in optical lattices. For example, by quenching to the emergent Hamiltonian during the expansion one can suddenly freeze the atomic cloud, as it becomes a stationary state [197]. This opens a door towards the efficient engineering of tailored many-particle states.

Appendix A

Yang-Yang Thermodynamics

The Yang-Yang equation for the dressed energy is [158]

$$\epsilon(k) = \frac{\hbar^2 k^2}{2m} - \mu - \frac{k_B T}{2\pi} \int_{-\infty}^{\infty} dq \frac{2c}{c^2 + (k-q)^2} \ln[1 + e^{-\frac{\epsilon(q)}{k_B T}}] \,, \tag{A.1}$$

$\epsilon(k)$ is used to compute thermodynamic quantities. The thermodynamic potential density is given by the expression

$$\Omega(\mu, c, T) = -\frac{k_B T}{2\pi} \int_{-\infty}^{\infty} dq \ln[1 + e^{-\frac{\epsilon(q)}{k_B T}}] \,. \tag{A.2}$$

All other thermodynamic quantities of interest here can be derived from $\Omega(\mu, c, T)$ through the following relations

$$e = \Omega + \mu\rho + Ts, \; p = -\Omega, \; \rho = -\frac{\partial \Omega}{\partial \mu}, \; s = -\frac{\partial \Omega}{\partial T} \,, \tag{A.3}$$

where e is the energy density, s is the entropy density, and p is the pressure.

For very strong contact interactions, i.e., $c \gg 1$, one can Taylor expand $\epsilon(k)$ in terms of $1/c$

$$\epsilon(k) = \frac{\hbar^2 k^2}{2m} - \mu + \frac{2}{c}\Omega + O\left(\frac{1}{c^3}\right) \,. \tag{A.4}$$

The dressed energy $\epsilon(k)$ can then be obtained iteratively. To zeroth order: $\epsilon^{(0)}(k) = \hbar^2 k^2/(2m) - \mu$. This allows one to compute Ω to lowest order

$$\Omega^{(0)} = -\frac{\sqrt{m}(k_B T)^{3/2}}{\hbar\sqrt{2\pi}} f_{3/2}\left(\frac{\mu}{k_B T}\right) \,, \tag{A.5}$$

where

$$f_\nu(\alpha) = \frac{1}{\Gamma(\nu)} \int_0^\infty \frac{x^{\nu-1} dx}{e^{(x-\alpha)} + 1} \,, \tag{A.6}$$

is the Fermi-Dirac function. Using Eq. (A.5), and the relations (A.3), one obtains the following expressions for the density and the energy of the system

$$\rho^{(0)} = \frac{\sqrt{m}(k_B T)^{1/2}}{\hbar\sqrt{2\pi}} f_{1/2}\left(\frac{\mu}{k_B T}\right) \,, \tag{A.7a}$$

$$e^{(0)} = \frac{\sqrt{m}(k_B T)^{3/2}}{2\hbar\sqrt{2\pi}} f_{3/2}\left(\frac{\mu}{k_B T}\right) \,. \tag{A.7b}$$

These are nothing but the density and the energy density of a system of noninteracting spinless fermions.

Substituting $\Omega \to \Omega^{(0)}$ in Eq. (A.4), one obtains

$$\begin{aligned} &\epsilon^{(1)}(k) = k^2 - \mu^{(1)} \,, \quad \text{where} \\ &\mu^{(1)} = \mu + \frac{\sqrt{2m}(k_B T)^{3/2}}{\hbar\sqrt{\pi}c} f_{3/2}\left(\frac{\mu}{k_B T}\right) \,. \end{aligned} \tag{A.8}$$

Now, substituting $\mu \to \mu^{(1)}$ in Eq. (A.5), and expanding to first order in $1/c$, we get

$$\Omega^{(1)} = -\frac{\sqrt{m}(k_B T)^{3/2}}{\hbar\sqrt{2\pi}} f_{3/2} \times \left(1 + \frac{\sqrt{2mk_B T}}{c\hbar\sqrt{\pi}} f_{1/2}\right) \,, \tag{A.9}$$

where, from now on, by f_ν it is meant $f_\nu(\mu/k_B T)$. Finally, substituting $\Omega \to \Omega^{(1)}$ in Eq. (A.4), we get that

$$\begin{aligned} &\epsilon^{(2)}(k) = k^2 - \mu^{(2)} \,, \quad \text{where} \\ &\mu^{(2)} = \mu + \frac{\sqrt{2m}(k_B T)^{3/2}}{\hbar\sqrt{\pi}c} f_{3/2} \times \left(1 + \frac{\sqrt{2mk_B T}}{c\hbar\sqrt{\pi}} f_{1/2}\right) \,. \end{aligned} \tag{A.10}$$

This expression allows us to obtain $\Omega^{(2)}$ by substituting $\mu \to \mu^{(2)}$ in Eq. (A.5). Expanding the resulting equation up to second order in $1/c$, one obtains

$$\begin{aligned} \Omega^{(2)} = &\frac{\sqrt{m}(k_B T)^{3/2}}{\hbar\sqrt{2\pi}} f_{3/2} \\ &\times \left[1 + \frac{\sqrt{2mk_B T}}{c\hbar\sqrt{\pi}} f_{1/2} + \left(\frac{\sqrt{2mk_B T}}{c\hbar\sqrt{\pi}}\right)^2 \left(f_{1/2}^2 + \frac{1}{2} f_{3/2} f_{-1/2}\right)\right] \,. \end{aligned} \tag{A.11}$$

Using Eq. (A.11), we can calculate Tan's contact through Tan's sweep relation

$$\mathcal{C} = -\frac{2mc^2 L}{\hbar^2}\left(\frac{\partial p}{\partial c}\right)_{\mu,T} . \tag{A.12}$$

The result obtained to order $1/c$ is:

$$\mathcal{C} = \frac{(2mk_BT)^2 L}{\hbar^4 2\pi} f_{3/2} \times \left[f_{1/2} + \frac{\sqrt{2m}(k_BT)^{1/2}}{\hbar\sqrt{\pi}c}(2f_{1/2}^2 + f_{-1/2}f_{3/2})\right] . \tag{A.13}$$

Appendix B

Units Definition in the PIMC Simulation

In the actual PIMC simulation of a continuous system, we usually choose an arbitrary length l_0 as the unit length. The energy unit is then defined by $\epsilon_0 = \hbar^2/(2ml_0^2)$ and the temperature unit is $T_0 = \epsilon_0/k_B$.

Consider a specific example of simulating cold atoms on an optical lattice. For a lattice spacing $A = \lambda/2 = \mathcal{A}l_0$, where $\mathcal{A}$ is a unitless constant, one can define the effective mass $m_p = mA^2k_B/\hbar^2 = 1/2$ (with the inverse temperature unit, e.g., nK^{-1}, μK^{-1} or K^{-1}) due to the arbitrariness of the length unit l_0. For the case of ^{87}Rb atoms, if one choose the unit of m_p to be in nK, then $l_0 = 333.2nm$.

One other example involves the recoil energy $E_R = \hbar^2k^2/(2m)$, where $k = \pi/A$. Again, by plugging the previously defined formula, the recoil energy is $E_R/\epsilon_0 = \pi^2/A^2$. Other relevant parameters such as the chemical potential μ and the external confining potential V_0 should also be defined in units of ϵ_0.

B.1 Harmonic Trap

For an external harmonic potential of the form,

$$V_H = \frac{1}{2}m\omega^2x^2 \ . \tag{B.1}$$

One can rewrite it in terms of the dimensionless quantities,

$$\frac{V_H}{\epsilon_0} = \frac{1}{4}\left(\frac{\hbar\omega}{\epsilon_0}\right)^2 \tilde{x}^2 \ . \tag{B.2}$$

The other important parameter is the trapping length a_{HO},

$$a_{\mathrm{HO}} = \sqrt{\frac{\hbar}{m\omega}} \ . \tag{B.3}$$

Under the dimensionless representation,

$$\frac{a_{\mathrm{HO}}}{l_0} = \sqrt{\frac{2\epsilon_0}{\hbar\omega}} \ . \tag{B.4}$$

From the derivation above, one realizes immediately that the effect of a harmonic trap is governed by the dimensionless parameter $\hbar\omega/\epsilon_0$.

B.2 Gaussian Trap

Another frequently used trapping potential is the Gaussian potential,

$$U(x) = U_0\left[1 - \exp\left(-\frac{x^2}{2\sigma^2}\right)\right] \ , \tag{B.5}$$

where, U_0 and σ denote the strength and width of the trap. From experiments, U_0 is usually defined in units of the recoil energy E_R and σ in standard length units. One can obtain the dimensionless version of U_0 and σ, by calculating $\tilde{\sigma} = \sigma/l_0$ and $\tilde{U_0} = U_0 E_R/\epsilon_0$.

Appendix C

Slater Determinants for 1D Lattice Systems

This appendix is complementary to the finite temperature approach introduced in Sec. 5.1. We first review the lattice approach for the ground state, proposed in Ref. [44, 45, 88, 89]. Then, we discuss the application of the lattice approach to fermionic systems [178].

C.1 Ground-state Approach for Bosons

C.1.1 Ground-State in Equilibrium

This section is a review of the method proposed in Refs. [44, 45]. The one-body correlations in the ground state of the system can be written as

$$G_{ij} = \langle \Psi_B^G | \, b_i b_j^\dagger \, | \Psi_B^G \rangle = \langle \Psi_F^G | \prod_{\alpha=1}^{i-1} e^{i\pi n_\alpha^f} f_i f_j^\dagger \prod_{\beta=1}^{j-1} e^{-i\pi n_\beta^f} \, | \Psi_F^G \rangle \ . \tag{C.1}$$

The ground-state wave function of the equivalent fermionic can be written in the following form

$$|\Psi_F^G\rangle = \prod_{\delta=1}^{N} \sum_{\sigma=1}^{L} P_{\sigma\delta} f_\sigma^\dagger \, |0\rangle \ . \tag{C.2}$$

For simplicity, one can express above wave function in terms of a Slater determinant, that means $|\Psi_F^G\rangle$ can be represented as a matrix $\{P_{\sigma\delta}\}$. In Eq. (C.1), the action of the phase $\prod_{\beta=1}^{j-1} e^{-i\pi n_\beta^f}$ on $|\Psi_F^G\rangle$ changes sign of $P_{\sigma\delta}$ for $\sigma \leq j-1$, labeled as P_B. The further creation of one particle at site j implies the addition of one more column

to P_B with $P_{Bj,N+1} = 1$ and other terms zero, labeled as P_B^j. Then the Green's function is given as the product of the two Slater determinant $G_{ij} = \det[P_B^{i\dagger} P_B^j]$. It then follows that the one-body density matrix can be written as

$$\rho_{ij} = \langle \Psi_B^G | \, b_i^\dagger b_j \, | \Psi_B^G \rangle = G_{ji} + \delta_{ij}(1 - 2G_{ii}) \; . \tag{C.3}$$

C.1.2 Time-evolving Initial Ground-State

This section is a review of the method proposed in Ref. [88, 89]. To study dynamics at zero temperature, one can construct arbitrary initial states (as long as they are pure states) and time evolve them in the Schrödinger picture. In the equivalent fermionic system, time evolving an initial wave function $|\Psi_F^I\rangle$ can be calculated as $|\Psi_F(\tau)\rangle = e^{-iH_F\tau} |\Psi_F^I\rangle$. Since $|\Psi_F^I\rangle$ can be represented with a matrix P, the time evolved state can be conveniently represented with $P(\tau) = e^{-iH_F\tau} P$. The one-body correlation function is

$$\begin{aligned} G_{ij}(\tau) &= \langle \Psi_B(\tau) | \, b_i b_j^\dagger \, | \Psi_B(\tau) \rangle \\ &= \langle \Psi_F(\tau) | \prod_{\alpha=1}^{i-1} e^{i\pi n_\alpha^f} f_i f_j^\dagger \prod_{\beta=1}^{j-1} e^{-i\pi n_\beta^f} \, | \Psi_F(\tau) \rangle \; . \end{aligned} \tag{C.4}$$

Action of the phase $\prod_{\beta=1}^{j-1} e^{-i\pi n_\beta^f}$ on the time evolving wave function $\Psi_F(\tau)$ leads to a sign change of elements in $P(\tau)$ for rows index $\sigma \leq j-1$, labeled as $P_B(\tau)$. The further creation of a particle at site j implies the addition of one extra column (with column index $\delta = N+1$) to $P_B(\tau)$ with nonzero element $P_{Bj,N+1}(\tau) = 1$. The corresponding matrix is labeled as $P_B^j(\tau)$. Thus the one-body correlation function is drastically simplified and can be calculated as

$$G_{ij}(\tau) = \det \left\{ [P_B^i(\tau)]^\dagger P_B^j(\tau) \right\} \; . \tag{C.5}$$

The one-body density matrix $\rho_{ij}(\tau)$ is related to $G_{ij}(\tau)$ by switching the order of b_i and $b_j^\dagger$, which leads to the following relations

$$\rho_{ij}(\tau) = G_{ji}(\tau) + \delta_{ij}[1 - 2G_{ii}(\tau)] \; . \tag{C.6}$$

C.2 Noninteracting Fermions

C.2.1 Ground State in Equilibrium

As shown in Sec. C.1, the fermionic ground-state wave function [Eq. (C.2)] can be represented as a matrix $P_{L\times N}$, where L is the number of lattice sites. Define $\hat{f}_\alpha^\dagger$ as the single-particle creation operator in the eigenenergy basis, then P is the matrix connecting $\hat{f}_\alpha^\dagger$ to $\hat{f}_i^\dagger$ in real space and $P^\dagger$ is the matrix for the inverse transformation. Based on this observation, it is straightforward to calculate the one-body density matrix,

$$\begin{aligned}\rho_{ij}^F &= \left\langle \Psi_F^G \middle| \hat{f}_i^\dagger \hat{f}_j \middle| \Psi_F^G \right\rangle \\ &= \left\langle \Psi_F^G \middle| \left(\sum_{\alpha=1}^N P_{i\alpha}\hat{f}_\alpha^\dagger\right)\left(\sum_{\beta=1}^N P_{j\beta}^*\hat{f}_\beta\right) \middle| \Psi_F^G \right\rangle = \sum_{\alpha=1}^N P_{i\alpha}P_{j\alpha}^* \,.\end{aligned} \tag{C.7}$$

Thus, it is clear that the density matrix is given as,

$$\rho^F = PP^\dagger \,. \tag{C.8}$$

One can prove Eq. (C.8) by simplifying the results in Sec. C.1.1. The one-body correlation function could be obtained directly as

$$G_{ij}^F = \langle \Psi_F^G | \, \hat{f}_i \hat{f}_j^\dagger \, | \Psi_F^G \rangle = \det[P^{i\dagger}P^j] \,. \tag{C.9}$$

We can further take a look at the kernel of the determinant in Eq. (C.9). From the definition in Sec. C.1.1, $P^i = [P,\ \mathbf{v}_i]$, where $\mathbf{v}_i$ is a unit column vector with ith element 1. Thus,

$$P^{i\dagger}P^j = \begin{bmatrix} P^\dagger \\ \mathbf{v}_i^T \end{bmatrix} \begin{bmatrix} P & \mathbf{v}_j \end{bmatrix} = \begin{bmatrix} I & P_{\cdot\, j}^\dagger \\ P_{i\,\cdot} & \delta_{ij} \end{bmatrix} \,. \tag{C.10}$$

This nice property of $P^{i\dagger}P^j$ leads directly to the result for G_{ij}^F,

$$G_{ij}^F = \delta_{ij} - P_{i\,\cdot}P_{\cdot\, j}^\dagger \,, \tag{C.11}$$

which is consistent with Eq. (C.8), and the correlation matrix can be expressed as,

$$G^F = I - PP^\dagger \ . \tag{C.12}$$

C.2.2 Dynamics of the Ground State

As being pointed out previously, the time-evolving fermionic state can be written as a matrix $P(\tau)$. correspondingly, the equal-time one-body correlation can be generalized from Eq. (C.8) and Eq. (C.12).

C.2.3 Finite Temperature in Equilibrium

The one-particle Green's function of noninteracting fermions at finite temperature is given by

$$G^F_{ij} = \mathrm{Tr}\left[\hat{f}_i \hat{f}_j^\dagger \hat{\rho}^F_{\mathrm{GE}}\right] = \frac{1}{Z}\mathrm{Tr}\left[\hat{f}_i \hat{f}_j^\dagger \exp\left(-\frac{\hat{H}_f - \mu\hat{N}}{T}\right)\right] \ . \tag{C.13}$$

If we define $\gamma_\alpha = (E_\alpha - \mu)/T$, and combine Eq. (5.8) [178],

$$\begin{aligned} G^F_{ij} &= \frac{\mathrm{Tr}\left[\hat{f}_i \hat{f}_j^\dagger \prod_\alpha e^{-\hat{f}_\alpha^\dagger \gamma_\alpha \hat{f}_\alpha}\right]}{\prod_\alpha (1 + e^{-\gamma_\alpha})} \\ &= \sum_\beta P^*_{i\beta} P_{j\beta} \frac{\mathrm{Tr}\left[\hat{f}_\beta \hat{f}_\beta^\dagger \prod_\alpha e^{-\hat{f}_\alpha^\dagger \gamma_\alpha \hat{f}_\alpha}\right]}{\prod_\alpha (1 + e^{-\gamma_\alpha})} = \sum_\beta P^*_{i\beta} P_{j\beta} \frac{1}{1 + e^{-\gamma_\beta}} \\ &= \left[P\left(I + e^{-(E-\mu I)/T}\right)^{-1} P^\dagger\right]_{ij} = \left[I + e^{-(H_f - \mu I)/T}\right]^{-1}_{ij} \ . \end{aligned} \tag{C.14}$$

Thus it is straightforward to conclude that,

$$G^F = \left[I + e^{-(H_f - \mu I)/T}\right]^{-1} \ . \tag{C.15}$$

Eq. (C.14) also serves as a proof for the alternative expressions of the diagonal terms of one-body density matrix in Eq. (5.12) and Eq. (5.15). In addition, it is important to stress that the one-particle correlation matrix and subsequently the one-body density matrix calculated from Eq. (C.15) is much more efficient than the bosonic analogs, Eq. (5.10) and Eq. (5.14).

C.2.4 Dynamics at Finite Temperature

Based on Eq. (C.15), it is straightforward to calculate the equal-time one-particle correlations,

$$G^F(\tau) = \left[e^{iH_F\tau}\left(I + e^{-(H_I-\mu I)/T}\right)e^{-iH_F\tau}\right]^{-1} , \tag{C.16}$$

where H_I (H_F) is the pre-quench (post-quench) Hamiltonian. Correspondingly, the one-body density matrix is given as

$$\rho^F(\tau) = I - G^F(\tau) . \tag{C.17}$$

Appendix D

Calculating Renormalized On-site Interactions

This appendix provides details about constructing the multi-orbital Hubbard model for a single-site problem. We discuss constructions for a harmonic potential and a hard-wall box potential.

D.1 Harmonic Potential

The full Hamiltonian for contact interacting bosons under an 1D harmonic trap is written here again for reference,

$$\begin{aligned}
\hat{H} &= \hat{H}_{\text{free}} + \hat{H}_{\text{int}} \ , \\
\hat{H}_{\text{free}} &= \int dx \hat{\Psi}^\dagger(x) \left[-\frac{\hbar^2}{2m}\frac{\partial^2}{\partial x^2} + \frac{1}{2}m\omega^2 x^2 \right] \hat{\Psi}(x) \ , \\
\hat{H}_{\text{int}} &= \frac{g_{1\text{D}}}{2} \int dx \hat{\Psi}^\dagger(x)\hat{\Psi}^\dagger(x)\hat{\Psi}(x)\hat{\Psi}(x) \ ,
\end{aligned} \tag{D.1}$$

where the bosonic field operator satisfies the following commutation relation,

$$[\hat{\Psi}(x), \hat{\Psi}^\dagger(x')] = \delta(x - x') \ . \tag{D.2}$$

The field operator $\hat{\Psi}$ ($\hat{\Psi}^\dagger$) is further expanded on the basis of single-particle harmonic oscillator eigenstates ψ_l,

$$\begin{aligned} \hat{\Psi}(x) &= \sum_{l=0}^{\infty} \psi_l(x)\hat{b}_l \ , \\ [\hat{b}_l, \hat{b}_{l'}^\dagger] &= \delta_{l,l'} \ . \end{aligned} \tag{D.3}$$

The complete expression of ψ_l is rewritten here,

$$\psi_l(x) = \frac{1}{\sqrt{2^l l!}} \left(\frac{m\omega}{\pi\hbar}\right)^{1/4} \exp\left(-\frac{m\omega}{2\hbar}x^2\right) H_l\left(\sqrt{\frac{m\omega}{\hbar}}x\right) \ . \tag{D.4}$$

where, $H_l(x)$ is the Hermite polynomials with $l = 0, 1, 2, \cdots$. By transforming the Hubbard Hamiltonian Eq. (D.1) in the ladder operator basis, it is straightforward to obtain a simplified form of $\hat{H}_{\text{free}}$,

$$\hat{H}_{\text{free}} = \sum_{l,m} \hbar\omega \left(m + \frac{1}{2}\right) \hat{b}_l^\dagger \hat{b}_m \delta_{l,m} \ . \tag{D.5}$$

In addition, the interaction term $\hat{H}_{\text{int}}$ becomes,

$$\hat{H}_{\text{int}} = \frac{g_{1\text{D}}}{2} \int dx \sum_{l,m,n,q} \psi_l(x)\psi_m(x)\psi_n(x)\psi_q(x) \hat{b}_l^\dagger \hat{b}_m^\dagger \hat{b}_n \hat{b}_q \ . \tag{D.6}$$

Here, we define U_{lmnq} as the coefficient in front of the ladder operators and substitute $y = x\sqrt{m\omega/\hbar}$, then

$$\begin{aligned} \hat{H}_{\text{int}} &= \sum_{l,m,n,q} U_{lmnq} \hat{b}_l^\dagger \hat{b}_m^\dagger \hat{b}_n \hat{b}_q \ , \quad \text{with} \\ U_{lmnq} &= \frac{g_{1\text{D}}}{2\pi} \sqrt{\frac{m\omega}{\hbar}} \int dy e^{-2y^2} \frac{H_l(y)H_m(y)H_n(y)H_q(y)}{\sqrt{2^l l! 2^m m! 2^n n! 2^q q!}} \ . \end{aligned} \tag{D.7}$$

To further simplify the expression in Eq. (D.7), we introduce the following constant of integral,

$$I_{lmnq} = \frac{1}{\pi} \int dy e^{-2y^2} \frac{H_l(y)H_m(y)H_n(y)H_q(y)}{\sqrt{2^l l! 2^m m! 2^n n! 2^q q!}} \ . \tag{D.8}$$

By rewriting the Hamiltonian in units of $\hbar\omega$, and define $u_{lmnq} = U_{lmnq}/(\hbar\omega)$, we obtain the final unit free expression for the Hubbard Hamiltonian, labeled as $\hat{\tilde{H}}$,

$$\hat{\tilde{H}} = \sum_m \left(\frac{1}{2} + m\right) \hat{b}_m^\dagger \hat{b}_m + \sum_{lmnq} u_{lmnq} \hat{b}_l^\dagger \hat{b}_m^\dagger \hat{b}_n \hat{b}_q \ , \quad \text{where}$$
$$u_{lmnq} = -\frac{a_{\rm HO}}{a_{\rm 1D}} I_{lmnq} \ . \tag{D.9}$$

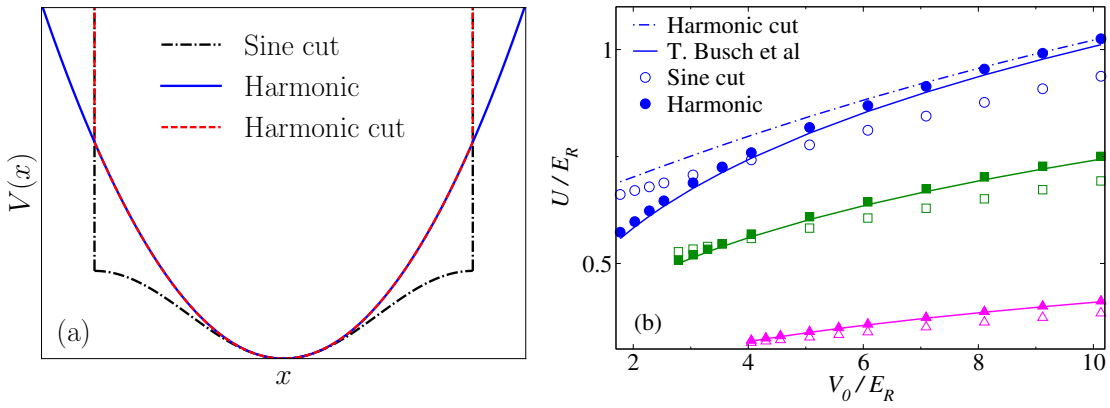

Figure D.1: (a) Schematics of different trapping potentials for a single site, including a harmonic (solid), cut harmonic (dashed), cut sine (dash-dot) potentials. (b) Comparison of U from exact-diagonalization results from a multi-orbital model of two particles in different traps. These values of U are obtained by taking the asymptotic limit of fitted values with increasing orbital numbers. These results are compared with the exact calculations of two-particle wavefunctions in a harmonic trap [168]. Data for different interaction strengths $a_{\rm 1D}/a = -2, \ -1, \ -2/3$ are shown (magenta, dark-green, blue).

For a given cutoff in number of orbitals $N_{\rm orb}$, one can obtain the manybody ground state from diagonalizing the Hamiltonian in Eq. (D.9) and U accordingly from the ground-state interaction energy. For slightly different external traps, one can still expand in the harmonic oscillator basis. In these cases, off-diagonal quadratic terms will enter in Eq. (D.9). Fig. D.1(b) extrapolated results of U for external harmonic trap and its descendants, cut sine and harmonic potential at the boundary of a single site. For a harmonic trap, the diagonalization results of U are compared with exact two-particle wavefunction calculations [168]. The agreement is pretty good for weaker interactions and a slight difference at strong interactions exists, e.g., $a_{\rm 1D}/a = -2/3$, because higher-level orbitals are involved.

In Fig. D.1(b), estimations of U from cut harmonic trap become increasingly higher with decreasing depth of the trap. There exists more involved results comparing a cut sine potential with a harmonic trap. It is shown in Fig. D.1(b) that U from sine potential is lower at deeper lattice depth and vice versa. This is because, in a sine potential, low-level orbitals are less confined and high-level orbitals becomes more confined compared with a harmonic trap, as shown in the schematic plot in Fig. D.1(a).

D.2 Hard-wall Box Potential

For the case of contact interacting bosons trapped in an 1D infinite square well potential,

$$V_{\text{trap}}(x) = \begin{cases} 0\ , & 0 \le x \le A \\ \infty\ , & x < 0,\ x > A \end{cases} \tag{D.10}$$

where A defines width of the box. As opposed to Eq. (D.3), the field operator should be expanded in the basis of single-particle eigenstates of an infinite square well (with $l = 1, 2, 3, \cdots$). Now, ψ_l becomes

$$\psi_l(x) = \sqrt{\frac{2}{A}} \sin\left(\frac{l\pi}{A}x\right)\ . \tag{D.11}$$

with eigenenergy $\epsilon_l = l^2\pi^2\epsilon_0$, and $\epsilon_0 = \hbar^2/(2mA^2)$. Then, according to the definition of U_{lmnq} in Eq. (D.7) and redefine the energy unit as ϵ_0, thus $u_{lmnq} = U_{lmnq}/\epsilon_0$ and

$$\begin{aligned} u_{lmnq} &= -\frac{A}{a_{1\text{D}}} I_{lmnq}\ , \quad \text{where} \\ I_{lmnq} &= \frac{8}{\pi}\int_0^\pi dy \sin(ly)\sin(my)\sin(ny)\sin(qy)\ . \end{aligned} \tag{D.12}$$

in which, the constant of integral I_{lmnq} can be solved analytically. The we obtain the equivalent Hubbard Hamiltonian of Eq. (D.9),

$$\hat{\tilde{H}} = \sum_{l=1} l^2\pi^2 \hat{b}_l^\dagger \hat{b}_l + \sum_{lmnq} u_{lmnq} \hat{b}_l^\dagger \hat{b}_m^\dagger \hat{b}_n \hat{b}_q\ . \tag{D.13}$$

Appendix E

Inverse Scattering Approach: A Practitioner's Guide

E.1 Mathieu Function

The single-particle Hamiltonian $\hat{H}_0$ in Eq. (4.3) can be solved analytically. The corresponding Schrödinger equation is given as,

$$-\frac{d^2}{dz^2}\phi_q^{(n)}(z) + \frac{V_0}{4E_R}[2 - 2\cos(2z)]\phi_q^{(n)}(z) = \frac{E_q^{(n)}}{E_R}\phi_q^{(n)}(z) \ , \tag{E.1}$$

where E_R is the recoil energy as defined in Sec. 4.1, and we applied the transformation $z = kx$. Eq. (E.1) can be directly related to the canonical form for Mathieu differential equation,

$$\frac{d^2y}{dz^2} + [a - 2s\,\cos(2z)]y = 0 \ . \tag{E.2}$$

The solution y corresponds to the eigenfunction $\phi_q^{(n)}(z)$. The parameter s is related to lattice depth $s = -V_0/(4E_R)$ and a to eigenenergy via $a = E_q^{(n)}/E_R - V_0/(2E_R)$. The eigenfunction y is given by the Floquet solution,

$$F(a, s, z) = e^{ir(a,s)z}u(a, s, z) \ . \tag{E.3}$$

In the language of a lattice model, $F(a, s, z)$ is of Bloch form, with $r(a, s)$ corresponding to the quasimomentum, and $u(a, s, z)$ is a complex valued function which is periodic in z with period π. Depending on the value of $r(a, s)$, the Floquet solution Eq. (E.3) can be further classified as shown in Table E.1[198].

Values of $r(a,s)$	Stability of $F(a,s,z)$	Period of $F(a,s,z)$	Second Independent Solution
complex	not bounded	not periodic	$F(a,s,-z)$
real and irrational	bounded	not periodic	$F(a,s,-z)$
rational and noninteger	bounded	periodic (not π or 2π)	$F(a,s,-z)$
integer	bounded	periodic (π or 2π)	$\tau z F(a,s,z) + f(z)$

Table E.1: Categorization of the Floquet solution in Eq. (E.3) based on the values of quasimomentum $r(a,s)$.

There are two real-valued functions which are closely related to the Floquet solution Eq. (E.3). The Mathieu cosine function $C(a,s,z)$ is a even function of z and takes the following form,

$$C(a,s,z) = \frac{F(a,s,z) + F(a,s,-z)}{2F(a,s,0)} \,. \tag{E.4}$$

At $z=0$, based on the definition, the Mathieu cosine function satisfies $C(a,s,0)=1$ and $C^{'}(a,s,0)=0$. Similarly, the Mathieu sine function $S(a,s,z)$ is an odd function of z and satisfies $S^{'}(a,s,0)=1$ and $S(a,s,0)=0$ at the origin,

$$S(a,s,z) = \frac{F(a,s,z) - F(a,s,-z)}{2F'(a,s,0)} \,. \tag{E.5}$$

Due to the connection to the Floquet solution, in general, the Mathieu cosine and sine functions[1] are aperiodic. Nonetheless, there exist special cases when the Mathieu cosine and sine functions become periodic. In the zero lattice limit $s \to 0$, Floquet solutions become pure plane waves, thus the Mathieu cosine and sine functions reduce to bare cosine and sine functions of z. As shown in Fig. E.1, for moderately small value of s, the Mathieu functions can still be well approximated by the corresponding trigonometric functions. The other case involves integer values of

[1]The Mathieu cosine and sine functions can be obtained from **MathieuC** and **MathieuS** functions in Mathematica,

$$C(a,s,z) = \frac{\textbf{MathieuC}[a,s,z]}{\textbf{MathieuC}[a,s,0]}, \quad S(a,s,z) = \frac{\textbf{MathieuS}[a,s,z]}{\textbf{MathieuSPrime}[a,s,0]} \,. \tag{E.6}$$

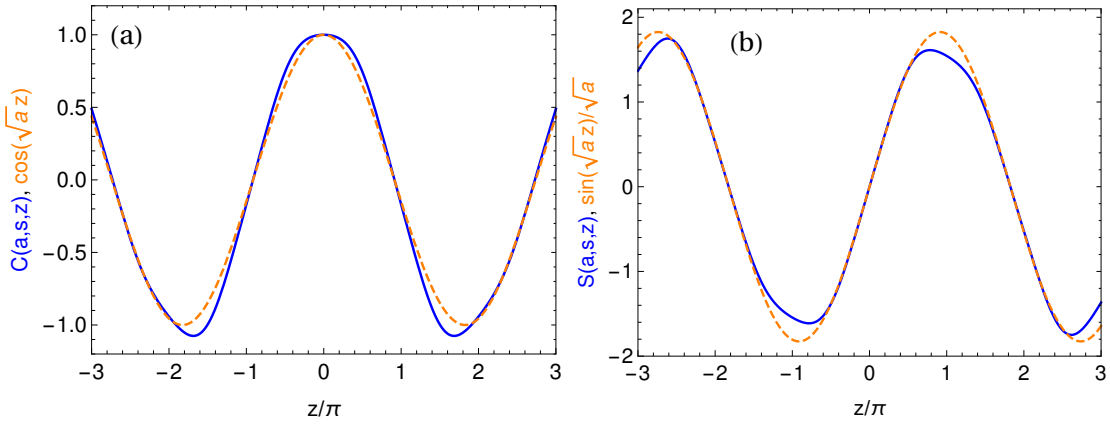

Figure E.1: (a) Mathieu cosine and (b) Mathieu sine functions for $a = 0.3$ and $s = 0.1$ (blue lines), compared with zero lattice depth $s = 0$ asymptotic results (orange dashed lines).

the quasimomentums $r(a, s)$, for which there exist special values of a, the Floquet solution is a periodic function with period at most π or 2π. In the single-particle energy spectrum, these values of quasimomentums correspond to momentums where energy gaps exist. Examples of Mathieu cosine and sine functions with integer $r(a, s)$, labeled as $CE(r, s, z)$ and $SE(r, s, z)$ respectively are shown in Fig. E.2.

We can also obtain the original Floquet solution from the Mathieu cosine and sine functions. For $z = \pi$,

$$\begin{aligned} C(a, s, \pi) &= \frac{e^{ir(a,s)\pi}F(a, s, 0) + e^{-ir(a,s)\pi}F(a, s, 0)}{2F(a, s, 0)} , \\ S(a, s, \pi) &= \frac{e^{ir(a,s)\pi}F(a, s, 0) - e^{-ir(a,s)\pi}F(a, s, 0)}{2F'(a, s, 0)} . \end{aligned} \tag{E.7}$$

This equation can be obtained by taking the property that $u(a, s, 0) = u(a, s, \pi)$. By combining Eq. (E.7), Eq. (E.4) and Eq. (E.5), one reaches the convenient expression for $F(a, s, z)$,

$$\begin{aligned} F(a, s, z) &= C(a, s, z)F(a, s, 0) + S(a, s, z)F'(a, s, 0) \\ &= F(a, s, 0)\left[C(a, s, z) + \frac{e^{ir(a,s)\pi} - C(a, s, \pi)}{S(a, s, \pi)}S(a, s, z)\right] . \end{aligned} \tag{E.8}$$

We apply Eq. (E.8) to numerically calculate the Floquet wavefunctions $F(a, s, z)$ normalized by $F(a, s, 0)$.

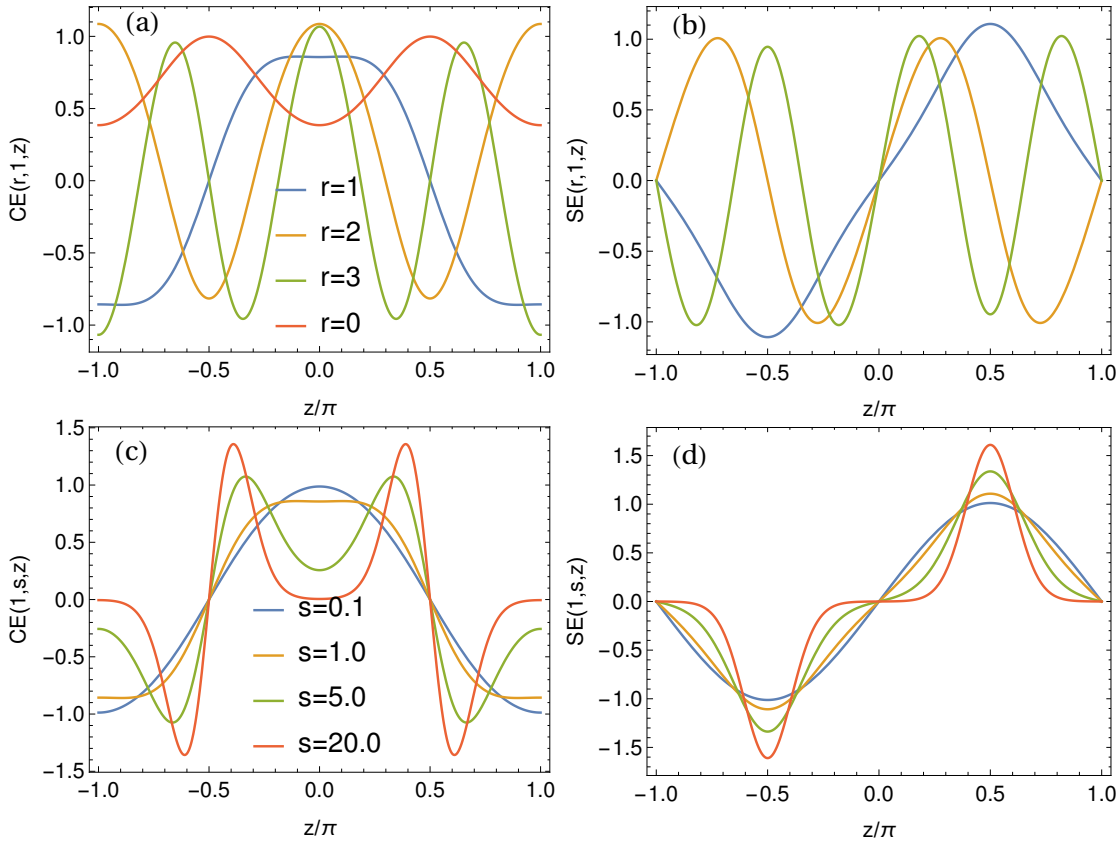

Figure E.2: (a) and (b) the Mathieu cosine functions $CE(r, s = 1, z)$ and sine functions $SE(r, s = 1, z)$ at integer values of $r = 0,\ 1,\ 2,\ 3$. (c) and (d) the Mathieu cosine functions $CE(r = 1, s, z)$ and sine functions $SE(r = 1, s, z)$ for different values of lattice depths $s = 0.1,\ 1,\ 5,\ 20$.

E.2 Two Particles in a Lattice

In the following, we consider single-particle Hamiltonian $\hat{H}_0 = -\hbar^2/(2m)\partial_z^2 + W\cos(\kappa_L z)$, which is connected to Eq. (4.3) with $\kappa_L = 2k_L$, $W = V_0/2$ and an overall constant energy shift W. Here, for simplicity, we define $\hbar = m = \kappa_L = 1$. The recoil energy based on the definition in Sec. 4.1 is $E_R = \hbar^2 k_L^2/(2m) = 1/8$ and the lattice spacing $a = 2\pi/\kappa_L = 2\pi$. Then the Bloch wavefunctions are related to the Floquet soltions to the Mathieu equation in the following way,

$$\psi(\epsilon, W, \pm z) = F(8\epsilon, 4W, \pm z/2)\ , \tag{E.9}$$

with ϵ and W now represent the single-particle energy and lattice depth, ψ is the same as the single-particle Bloch wavefunction in Sec. 4.4. The Bloch momentum and eigenenergy are also related to two reciprocal functions,

$$\begin{aligned} k(\epsilon, W) &= r(8\epsilon, 4W)/2 \ , \\ \epsilon(k, W) &= a(2k, 4W)/8 \ . \end{aligned} \tag{E.10}$$

Fig. E.3 shows the relation k vs $\epsilon(k)$. Due to the presence of the periodic lattice, energy gaps open at integer multiples of $\kappa_L/2$. In addition, for $\epsilon(k)$ within the energy gaps, the quasimomentum k is complex.

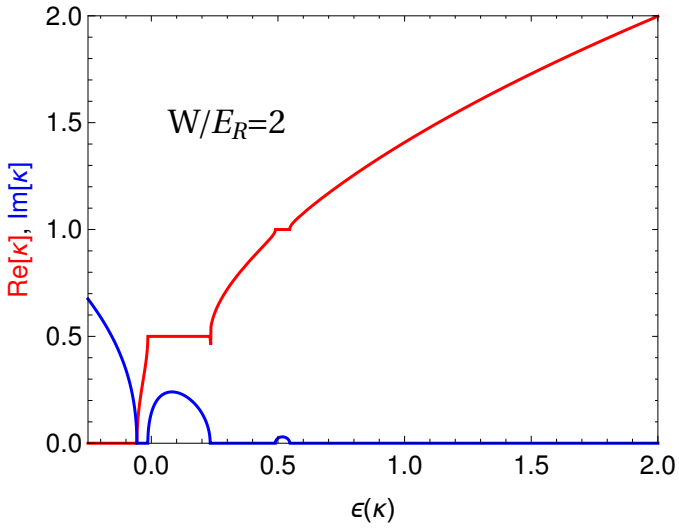

Figure E.3: Real and imaginary part of the quasimomentum vs the eigenenergy for an external lattice depth $W/E_R = 2$ (or equivalently $s = 1$ for the Floquet solution).

In order to obtain the effective scattering length $a_{\rm CM}$ of the continuous model, we focus on single-particle energy $\epsilon(q) = \epsilon(q \to 0, W)$ close to ground state energy $\epsilon(0, W)$. It was indicated in Eq. (4.39) that the two-body scattering state is a combination of the propagating and evanescent components. The propagating part of the two-body wavefunction along the interaction line $r \to 0$, as defined in Eq. (4.41), is composed of real and periodic functions of the COM position R with period the same as the lattice spacing a. Their derivatives with respect to the relative position r are vanishingly small, as the single-particle momentum $q = k(\epsilon(q), W)$ is approaching zero. An example of $\Psi^{(2)}_{+,\infty}(R)$ and $\Psi'^{(2)}_{+,\infty}(R)$ is shown

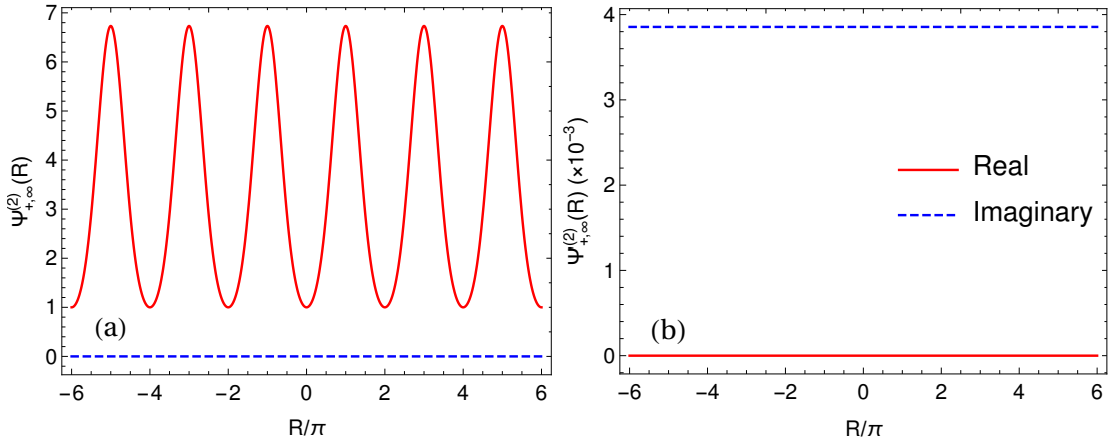

Figure E.4: (a) the propagating part of the two-body wavefunction $\Psi^{(2)}_{+,\infty}(R)$ and (b) its derivative $\Psi'^{(2)}_{+,\infty}(R)$ with respect to the relative position r, along the interaction line $r = 0$.

in Fig. E.4.

In addition, as explained in Sec. 4.4.3, there also exist contributions to the two-body wavefunction with complex single-particle energies (see Eq. (4.33)) but a total two-body energy $2\epsilon(q)$. This leads to complex Bloch momentums, thus the single-particle eigenstate vanishes or diverges at infinity, as shown in Fig. E.5(b) and E.5(c). Interestingly, the corresponding two-body states are real and periodic functions of the COM and relative positions. Along the interaction line, the periodicity is given by a/l. l is a positive integer and the real part of the Bloch momentum is required to be $\mathrm{Re}[k(\eta_l)] = l\kappa/2$, as also being pointed out in Eq. (4.38). An example of the two-body states $\chi^{(2)}_l(R)$ and its derivative with respect to r at $r = 0$ is shown in Fig. E.5(d) and E.5(e). Due to the periodicity of all functions involved in Eq. (4.42), one can solve for a_{CM} with Fourier expansion as outlined in Sec. 4.4.4.

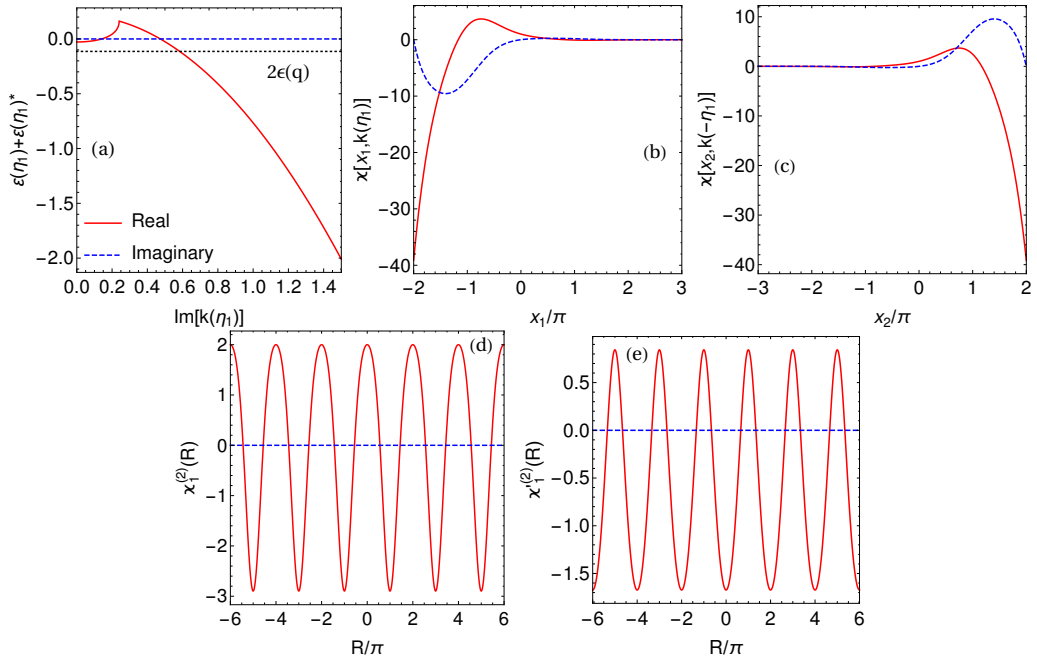

Figure E.5: Evanescent part of the scattering wavefunction for $W/E_R = 2$ (or equivalently $s = 1$). (a) Matching the total kinetic energy of two particles for the evanescent solution with $2\epsilon(q)$ by tuning the imaginary part of the quasimomentum $k(\eta_1)$, of which the real part is $\mathrm{Re}[k(\eta_1)] = \kappa/2$. By definition, $\varepsilon(\eta) = \epsilon(q) + i\eta$. (b) and (c) single-particle evanescent solutions $\chi[x_1, k(\eta_1)]$ and $\chi[x_2, -k(\eta_1)]$. (d) and (e) contribution of the evanescent solutions to the two-body wavefunction $\chi_l^{(2)}(R)$ and $\chi_l'^{(2)}(R)$ along the interaction line $r = 0$.

Bibliography

[1] I. Bloch, J. Dalibard, and W. Zwerger, "Many-body physics with ultracold gases," Rev. Mod. Phys. **80**, 885 (2008).

[2] M. A. Cazalilla, R. Citro, T. Giamarchi, E. Orignac, and M. Rigol, "One-dimensional bosons: From condensed matter systems to ultracold gases," Rev. Mod. Phys. **83**, 1405 (2011).

[3] M. Greiner, I. Bloch, O. Mandel, T. W. Hänsch, and T. Esslinger, "Exploring phase coherence in a 2D lattice of Bose-Einstein condensates," Phys. Rev. Lett. **87**, 160405 (2001).

[4] H. Moritz, T. Stöferle, M. Köhl, and T. Esslinger, "Exciting collective oscillations in a trapped 1D gas," Phys. Rev. Lett. **91**, 250402 (2003).

[5] E. H. Lieb and W. Liniger, "Exact analysis of an interacting Bose gas. I. The general solution and the ground state," Phys. Rev. **130**, 1605 (1963).

[6] E. H. Lieb, "Exact analysis of an interacting Bose gas. II. The excitation spectrum," Phys. Rev. **130**, 1616 (1963).

[7] S. Li, S. R. Manmana, A. M. Rey, R. Hipolito, A. Reinhard, J.-F. Riou, L. A. Zundel, and D. S. Weiss, "Self-trapping dynamics in a two-dimensional optical lattice," Phys. Rev. A **88**, 023419 (2013).

[8] M. Olshanii, "Atomic scattering in the presence of an external confinement and a gas of impenetrable bosons," Phys. Rev. Lett. **81**, 938 (1998).

[9] T. Kinoshita, T. Wenger, and D. S. Weiss, "Observation of a one-dimensional Tonks-Girardeau gas," Science **305**, 1125 (2004).

[10] T. Kinoshita, T. Wenger, and D. S. Weiss, "Local pair correlations in one-dimensional Bose gases," Phys. Rev. Lett. **95**, 190406 (2005).

[11] M. Girardeau, "Relationship between systems of impenetrable bosons and fermions in one dimension," J. Math. Phys. **1**, 516 (1960).

[12] C.-N. Yang and C.-P. Yang, "Thermodynamics of a one-dimensional system of bosons with repulsive delta-function interaction," J. Math. Phys. **10**, 1115 (1969).

[13] D. Iyer and N. Andrei, "Quench dynamics of the interacting Bose gas in one dimension," Phys. Rev. Lett. **109**, 115304 (2012).

[14] J.-S. Caux and R. M. Konik, "Constructing the generalized Gibbs ensemble after a quantum quench," Phys. Rev. Lett. **109**, 175301 (2012).

[15] D. Iyer, H. J. Guan, and N. Andrei, "Exact formalism for the quench dynamics of integrable models," Phys. Rev. A **87**, 053628 (2013).

[16] M. Kormos, A. Shashi, Y.-Z. Chou, J. S. Caux, and A. Imambekov, "Interaction quenches in the one-dimensional Bose gas," Phys. Rev. B **88**, 205131 (2013).

[17] J. De Nardis, B. Wouters, M. Brockmann, and J.-S. Caux, "Solution for an interaction quench in the Lieb-Liniger Bose gas," Phys. Rev. A **89**, 033601 (2014).

[18] J. C. Zill, T. M. Wright, K. V. Kheruntsyan, T. Gasenzer, and M. J. Davis, "Relaxation dynamics of the Lieb-Liniger gas following an interaction quench: A coordinate Bethe-ansatz analysis," Phys. Rev. A **91**, 023611 (2015).

[19] T. Kinoshita, T. Wenger, and D. S. Weiss, "A quantum Newton's cradle," Nature **440**, 900 (2006).

[20] M. Rigol, V. Dunjko, V. Yurovsky, and M. Olshanii, "Relaxation in a completely integrable many-body quantum system: An *ab initio* study of the dynamics of the highly excited states of 1D lattice hard-core bosons," Phys. Rev. Lett. **98**, 050405 (2007).

[21] A. C. Cassidy, C. W. Clark, and M. Rigol, "Generalized thermalization in an integrable lattice system," Phys. Rev. Lett. **106**, 140405 (2011).

[22] J. S. Caux, P. Calabrese, and N. A. Slavnov, "One-particle dynamical correlations in the one-dimensional Bose gas," J. Stat. Mech. **2007**, P01008 (2007).

[23] G. E. Astrakharchik and S Giorgini, "Correlation functions and momentum distribution of one-dimensional Bose systems," Phys. Rev. A **68**, 031602 (2003).

[24] G. E. Astrakharchik and S. Giorgini, "Correlation functions of a Lieb-Liniger Bose gas," J. Phys. B: At. Mol. Opt. Phys. **39**, S1 (2006).

[25] P. Deuar, A. G. Sykes, D. M. Gangardt, M. J. Davis, P. D. Drummond, and K. V. Kheruntsyan, "Nonlocal pair correlations in the one-dimensional Bose gas at finite temperature," Phys. Rev. A **79**, 043619 (2009).

[26] M. Olshanii and V. Dunjko, "Short-distance correlation properties of the Lieb-Liniger system and momentum distributions of trapped one-dimensional atomic gases," Phys. Rev. Lett. **91**, 090401 (2003).

[27] A. Lenard, "Momentum distribution in the ground state of the one-dimensional system of impenetrable bosons," J. Math. Phys. **5**, 930 (1964).

[28] A. Lenard, "One-dimensional impenetrable bosons in thermal equilibrium," J. Math. Phys. **7**, 1268 (1966).

[29] H. G. Vaidya and C. A. Tracy, "One particle reduced density matrix of impenetrable bosons in one dimension at zero temperature," J. Math. Phys. **20**, 2291 (1979).

[30] M. Jimbo, T. Miwa, Y. Môri, and M. Sato, "Density matrix of an impenetrable Bose gas and the fifth painlevé transcendent," Phys. D **1**, 80 (1980).

[31] A. Minguzzi and D. M. Gangardt, "Exact coherent states of a harmonically confined Tonks-Girardeau gas," Phys. Rev. Lett. **94**, 240404 (2005).

[32] P. Vignolo and A. Minguzzi, "Universal contact for a Tonks-Girardeau gas at finite temperature," Phys. Rev. Lett. **110**, 020403 (2013).

[33] Y. Y. Atas, I. Bouchoule, D. M. Gangardt, and K. V. Kheruntsyan, "Collective many-body bounce in the breathing-mode oscillations of a Tonks-Girardeau gas," arXiv:1612.04593 (2016).

[34] Y. Y. Atas, D. M. Gangardt, I. Bouchoule, and K. V. Kheruntsyan, "Exact nonequilibrium dynamics of finite-temperature Tonks-Girardeau gases," Phys. Rev. A **95**, 043622 (2017).

[35] E. H. Lieb, T. Shultz, and D. Mattis, "Two soluble models of an antiferromagnetic chain," Ann. Phys. **16**, 407 (1961).

[36] B. M. McCoy, "Spin correlation functions of the X-Y model," Phys. Rev. **173**, 531 (1968).

[37] H. G. Vaidya and C. A. Tracy, "Crossover scaling function for the one-dimensional XY model at zero temperature," Phys. Lett. A **68**, 378 (1978).

[38] M. D. Girardeau, E. M. Wright, and J. M. Triscari, "Ground-state properties of a one-dimensional system of hard-core bosons in a harmonic trap," Phys. Rev. A **63**, 033601 (2001).

[39] A. Minguzzi, P. Vignolo, and M.P. Tosi, "High-momentum tail in the Tonks gas under harmonic confinement," Phys. Lett. A **294**, 222 (2002).

[40] G. J. Lapeyre, M. D. Girardeau, and E. M. Wright, "Momentum distribution for a one-dimensional trapped gas of hard-core bosons," Phys. Rev. A **66**, 023606 (2002).

[41] T. Papenbrock, "Ground-state properties of hard-core bosons in one-dimensional harmonic traps," Phys. Rev. A **67**, 041601(R) (2003).

[42] P. J. Forrester, N. E. Frankel, T. M. Garoni, and N. S. Witte, "Finite one-dimensional impenetrable Bose systems: Occupation numbers," Phys. Rev. A **67**, 043607 (2003).

[43] D. M. Gangardt, "Universal correlations of trapped one-dimensional impenetrable bosons," J. Phys. A: Math. Gen. **37**, 9335 (2004).

[44] M. Rigol and A. Muramatsu, "Universal properties of hard-core bosons confined on one-dimensional lattices," Phys. Rev. A **70**, 031603 (2004).

[45] M. Rigol and A. Muramatsu, "Ground-state properties of hard-core bosons confined on one-dimensional optical lattices," Phys. Rev. A **72**, 013604 (2005).

[46] M. Rigol, "Finite-temperature properties of hard-core bosons confined on one-dimensional optical lattices," Phys. Rev. A **72**, 063607 (2005).

[47] T. Jacqmin, B. Fang, T. Berrada, T. Roscilde, and I. Bouchoule, "Momentum distribution of one-dimensional Bose gases at the quasicondensation crossover: Theoretical and experimental investigation," Phys. Rev. A **86**, 043626 (2012).

[48] M. P. A. Fisher, P. B. Weichman, G. Grinstein, and D. S. Fisher, "Boson localization and the superfluid-insulator transition," Phys. Rev. B **40**, 546 (1989).

[49] T. Stöferle, H. Moritz, C. Schori, M. Köhl, and T. Esslinger, "Transition from a strongly interacting 1D superfluid to a Mott insulator," Phys. Rev. Lett. **92**, 130403 (2004).

[50] B. Paredes, A. Widera, V. Murg, O. Mandel, S. Fölling, I. Cirac, G. V. Shlyapnikov, T. W. Hänsch, and I. Bloch, "Tonks-Girardeau gas of ultracold atoms in an optical lattice," Nature **429**, 277 (2004).

[51] D. Jaksch, C. Bruder, J. I. Cirac, C. W. Gardiner, and P. Zoller, "Cold bosonic atoms in optical lattices," Phys. Rev. Lett. **81**, 3108 (1998).

[52] G. G. Batrouni, R. T. Scalettar, and G. T. Zimanyi, "Quantum critical phenomena in one-dimensional Bose systems," Phys. Rev. Lett. **65**, 1765 (1990).

[53] N. Elstner and H. Monien, "Dynamics and thermodynamics of the Bose-Hubbard model," Phys. Rev. B **59**, 12184 (1999).

[54] T. D. Kühner, S. R. White, and H. Monien, "One-dimensional Bose-Hubbard model with nearest-neighbor interaction," Phys. Rev. B **61**, 12474 (2000).

[55] S. Ejima, H. Fehske, and F. Gebhard, "Dynamic properties of the one-dimensional Bose-Hubbard model," EPL **93**, 30002 (2011).

[56] J. Carrasquilla, S. R. Manmana, and M. Rigol, "Scaling of the gap, fidelity susceptibility, and bloch oscillations across the superfluid-to-Mott-insulator transition in the one-dimensional Bose-Hubbard model," Phys. Rev. A **87**, 043606 (2013).

[57] E. Dagotto, "Correlated electrons in high-temperature superconductors," Rev. Mod. Phys. **66**, 763 (1994).

[58] M. Imada, A. Fujimori, and Y. Tokura, "Metal-insulator transitions," Rev. Mod. Phys. **70**, 1039 (1998).

[59] I. Bloch, J. Dalibard, and W. Zwerger, "Many-body physics with ultracold gases," Rev. Mod. Phys. **80**, 885 (2008).

[60] H. P. Büchler, G. Blatter, and W. Zwerger, "Commensurate-incommensurate transition of cold atoms in an optical lattice," Phys. Rev. Lett. **90**, 130401 (2003).

[61] E. Haller, R. Hart, M. J. Mark, J. G. Danzl, L. Reichsöllner, M. Gustavsson, M. Dalmonte, G. Pupillo, and H.-C. Nägerl, "Pinning quantum phase transition for a Luttinger liquid of strongly interacting bosons," Nature **466**, 597 (2010).

[62] T. Giamarchi, *Quantum Physics in One Dimension* (Oxford University Press, Oxford, 2003).

[63] G. E. Astrakharchik, K. V. Krutitsky, M. Lewenstein, and F. Mazzanti, "One-dimensional Bose gas in optical lattices of arbitrary strength," Phys. Rev. A **93**, 021605 (2016).

[64] G. Boéris, L. Gori, M. D. Hoogerland, A. Kumar, E. Lucioni, L. Tanzi, M. Inguscio, T. Giamarchi, C. D'Errico, G. Carleo, G. Modugno, and L. Sanchez-Palencia, "Mott transition for strongly interacting one-dimensional bosons in a shallow periodic potential," Phys. Rev. A **93**, 011601 (2016).

[65] S. Will, T. Best, U. Schneider, L. Hackermüller, D. Lühmann, and I. Bloch, "Time-resolved observation of coherent multi-body interactions in quantum phase revivals," Nature **465**, 197 (2010).

[66] P. R. Johnson, D. Blume, X. Y. Yin, W. F. Flynn, and E. Tiesinga, "Effective renormalized multi-body interactions of harmonically confined ultracold neutral bosons," New J. Phys. **14**, 053037 (2012).

[67] M. Łacki and J. Zakrzewski, "Fast dynamics for atoms in optical lattices," Phys. Rev. Lett. **110**, 065301 (2013).

[68] M. Łacki, D. Delande, and J. Zakrzewski, "Dynamics of cold bosons in optical lattices: effects of higher Bloch bands," New J. Phys. **15**, 013062 (2013).

[69] J. Major, M. Łacki, and J. Zakrzewski, "Reexamination of the variational Bose-Hubbard model," Phys. Rev. A **89**, 043626 (2014).

[70] O. Jürgensen, F. Meinert, M. J. Mark, H.-C. Nägerl, and D.-S. Lühmann, "Observation of density-induced tunneling," Phys. Rev. Lett. **113**, 193003 (2014).

[71] T. Sowiński, "Quantum phase transition in a shallow one-dimensional optical lattice," J. Opt. Soc. Am. B **32**, 670 (2015).

[72] O. Dutta, M. Gajda, P. Hauke, M. Lewenstein, D.-S. Lühmann, B. A. Malomed, T. Sowiński, and J. Zakrzewski, "Non-standard Hubbard models in optical lattices: a review," Rep. Prog. Phys. **78**, 066001 (2015).

[73] L. D'Alessio, Y. Kafri, A. Polkovnikov, and M. Rigol, "From quantum chaos and eigenstate thermalization to statistical mechanics and thermodynamics," Adv. Phys. **65**, 239 (2016).

[74] D. Fausti, R. I. Tobey, N. Dean, S. Kaiser, A. Dienst, M. C. Hoffmann, S. Pyon, T. Takayama, H. Takagi, and A. Cavalleri, "Light-induced superconductivity in a stripe-ordered cuprate," Science **331**, 189 (2011).

[75] L. Stojchevska, I. Vaskivskyi, T. Mertelj, P. Kusar, D. Svetin, S. Brazovskii, and D. Mihailovic, "Ultrafast switching to a stable hidden quantum state in an electronic crystal," Science **344**, 177 (2014).

[76] J. H. Mentink, K. Balzer, and M. Eckstein, "Ultrafast and reversible control of the exchange interaction in Mott insulators," Nat. Commun. **6**, 6708 (2015).

[77] J. J. Mendoza-Arenas, F. J. Gómez-Ruiz, M. Eckstein, D. Jaksch, and S. R. Clark, "Ultra-fast control of magnetic relaxation in a periodically driven Hubbard model," Ann. Phys. (Berlin) **529**, 1700024 (2017).

[78] T. Prosen, "Open XXZ spin chain: Nonequilibrium steady state and a strict bound on ballistic transport," Phys. Rev. Lett. **106**, 217206 (2011).

[79] M. Mierzejewski, P. Prelovšek, and T. Prosen, "Breakdown of the generalized Gibbs ensemble for current-generating quenches," Phys. Rev. Lett. **113**, 020602 (2014).

[80] E. Ilievski, M. Medenjak, T. Prosen, and L. Zadnik, "Quasilocal charges in integrable lattice systems," J. Stat. Mech. **2016**, 064008 (2016).

[81] O. A. Castro-Alvaredo, B. Doyon, and T. Yoshimura, "Emergent hydrodynamics in integrable quantum systems out of equilibrium," Phys. Rev. X **6**, 041065 (2016).

[82] B. Bertini, M. Collura, J. De Nardis, and M. Fagotti, "Transport in out-of-equilibrium XXZ chains: Exact profiles of charges and currents," Phys. Rev. Lett. **117**, 207201 (2016).

[83] A. De Luca, M. Collura, and J. De Nardis, "Nonequilibrium spin transport in integrable spin chains: Persistent currents and emergence of magnetic domains," Phys. Rev. B **96**, 020403 (2017).

[84] E. Ilievski and J. De Nardis, "Microscopic origin of ideal conductivity in integrable quantum models," Phys. Rev. Lett. **119**, 020602 (2017).

[85] M. Medenjak, C. Karrasch, and T. Prosen, "Lower bounding diffusion constant by the curvature of Drude weight," Phys. Rev. Lett. **119**, 080602 (2017).

[86] T. Antal, Z. Rácz, A. Rákos, and G. M. Schütz, "Transport in the XX chain at zero temperature: Emergence of flat magnetization profiles," Phys. Rev. E **59**, 4912 (1999).

[87] D. Karevski, "Scaling behaviour of the relaxation in quantum chains," Eur. Phys. J. B **27**, 147 (2002).

[88] M. Rigol and A. Muramatsu, "Emergence of quasicondensates of hard-core bosons at finite momentum," Phys. Rev. Lett. **93**, 230404 (2004).

[89] M. Rigol and A. Muramatsu, "Fermionization in an expanding 1D gas of hard-core bosons," Phys. Rev. Lett. **94**, 240403 (2005).

[90] M. Rigol and A. Muramatsu, "Free expansion of impenetrable bosons on one-dimensional optical lattices," Mod. Phys. Lett. B **19**, 861 (2005).

[91] D. Gobert, C. Kollath, U. Schollwöck, and G. Schütz, "Real-time dynamics in spin-1/2 chains with adaptive time-dependent density matrix renormalization group," Phys. Rev. E **71**, 036102 (2005).

[92] A. J. Daley, S. R. Clark, D. Jaksch, and P. Zoller, "Numerical analysis of coherent many-body currents in a single atom transistor," Phys. Rev. A **72**, 043618 (2005).

[93] F. Heidrich-Meisner, M. Rigol, A. Muramatsu, A. E. Feiguin, and E. Dagotto, "Ground-state reference systems for expanding correlated fermions in one dimension," Phys. Rev. A **78**, 013620 (2008).

[94] L. F. Santos and A. Mitra, "Domain wall dynamics in integrable and chaotic spin-1/2 chains," Phys. Rev. E **84**, 016206 (2011).

[95] S. Jesenko and M. Žnidarič, "Finite-temperature magnetization transport of the one-dimensional anisotropic Heisenberg model," Phys. Rev. B **84**, 174438 (2011).

[96] C. Karrasch, J. E. Moore, and F. Heidrich-Meisner, "Real-time and real-space spin and energy dynamics in one-dimensional spin-1/2 systems induced by local quantum quenches at finite temperatures," Phys. Rev. B **89**, 075139 (2014).

[97] V. Eisler and Z. Rácz, "Full counting statistics in a propagating quantum front and random matrix spectra," Phys. Rev. Lett. **110**, 060602 (2013).

[98] T. Sabetta and G. Misguich, "Nonequilibrium steady states in the quantum XXZ spin chain," Phys. Rev. B **88**, 245114 (2013).

[99] V. Alba and F. Heidrich-Meisner, "Entanglement spreading after a geometric quench in quantum spin chains," Phys. Rev. B **90**, 075144 (2014).

[100] R. Vasseur, C. Karrasch, and J. E. Moore, "Expansion potentials for exact far-from-equilibrium spreading of particles and energy," Phys. Rev. Lett. **115**, 267201 (2015).

[101] J. L. Lancaster, "Nonequilibrium current-carrying steady states in the anisotropic XY spin chain," Phys. Rev. E **93**, 052136 (2016).

[102] V. Eisler, F. Maislinger, and H. G. Evertz, "Universal front propagation in the quantum Ising chain with domain-wall initial states," SciPost Phys. **1**, 014 (2016).

[103] M. Ljubotina, M. Žnidarič, and T. Prosen, "Spin diffusion from an inhomogeneous quench in an integrable system," Nat. Commun. **8**, 16117 (2017).

[104] M. Heyl, A. Polkovnikov, and S. Kehrein, "Dynamical quantum phase transitions in the transverse-field Ising model," Phys. Rev. Lett. **110**, 135704 (2013).

[105] R. Vosk and E. Altman, "Dynamical quantum phase transitions in random spin chains," Phys. Rev. Lett. **112**, 217204 (2014).

[106] M. Heyl, "Dynamical quantum phase transitions in systems with broken-symmetry phases," Phys. Rev. Lett. **113**, 205701 (2014).

[107] F. Andraschko and J. Sirker, "Dynamical quantum phase transitions and the Loschmidt echo: A transfer matrix approach," Phys. Rev. B **89**, 125120 (2014).

[108] M. Heyl, "Scaling and universality at dynamical quantum phase transitions," Phys. Rev. Lett. **115**, 140602 (2015).

[109] N. Y. Yao, A. C. Potter, I.-D. Potirniche, and A. Vishwanath, "Discrete time crystals: Rigidity, criticality, and realizations," Phys. Rev. Lett. **118**, 030401 (2017).

[110] J. Zhang, P. W. Hess, A. Kyprianidis, P. Becker, A. Lee, J. Smith, G. Pagano, I.-D. Potirniche, A. C. Potter, A. Vishwanath, N. Y. Yao, and C. Monroe, "Observation of a discrete time crystal," Nature **543**, 217 (2017).

[111] S. Choi, J. Choi, R. Landig, G. Kucsko, H. Zhou, J. Isoya, F. Jelezko, S. Onoda, H. Sumiya, V. Khemani, C. von Keyserlingk, N. Y. Yao, E. Demler, and M. D. Lukin, "Observation of discrete time-crystalline order in a disordered dipolar many-body system," Nature **543**, 221 (2017).

[112] U. Schneider, L. Hackermüller, J. P. Ronzheimer, S. Will, S. Braun, T. Best, I. Bloch, E. Demler, S. Mandt, D. Rasch, and A. Rosch, "Fermionic transport and out-of-equilibrium dynamics in a homogeneous Hubbard model with ultracold atoms," Nat. Phys. **8**, 213 (2012).

[113] J. P. Ronzheimer, M. Schreiber, S. Braun, S. S. Hodgman, S. Langer, I. P. McCulloch, F. Heidrich-Meisner, I. Bloch, and U. Schneider, "Expansion dynamics of interacting bosons in homogeneous lattices in one and two dimensions," Phys. Rev. Lett. **110**, 205301 (2013).

[114] L. Xia, L. A. Zundel, J. Carrasquilla, A. Reinhard, J. M. Wilson, M. Rigol, and D. S. Weiss, "Quantum distillation and confinement of vacancies in a doublon sea," Nat. Phys. **11**, 316 (2015).

[115] L. Vidmar, J. P. Ronzheimer, M. Schreiber, S. Braun, S. S. Hodgman, S. Langer, F. Heidrich-Meisner, I. Bloch, and U. Schneider, "Dynamical quasicondensation of hard-core bosons at finite momenta," Phys. Rev. Lett. **115**, 175301 (2015).

[116] A. Micheli, A. J. Daley, D. Jaksch, and P. Zoller, "Single atom transistor in a 1D optical lattice," Phys. Rev. Lett. **93**, 140408 (2004).

[117] A. Micheli and P. Zoller, "Single-atom mirror for one-dimensional atomic lattice gases," Phys. Rev. A **73**, 043613 (2006).

[118] K. Rodriguez, S. R. Manmana, M. Rigol, R. M. Noack, and A. Muramatsu, "Coherent matter waves emerging from Mott-insulators," New J. Phys. **8**, 169 (2006).

[119] S. Langer, M. J. A. Schuetz, I. P. McCulloch, U. Schollwöck, and F. Heidrich-Meisner, "Expansion velocity of a one-dimensional, two-component Fermi gas during the sudden expansion in the ballistic regime," Phys. Rev. A **85**, 043618 (2012).

[120] C. J. Bolech, F. Heidrich-Meisner, S. Langer, I. P. McCulloch, G. Orso, and M. Rigol, "Long-time behavior of the momentum distribution during the sudden expansion of a spin-imbalanced Fermi gas in one dimension," Phys. Rev. Lett. **109**, 110602 (2012).

[121] L. Vidmar, S. Langer, I. P. McCulloch, U. Schneider, U. Schollwöck, and F. Heidrich-Meisner, "Sudden expansion of Mott insulators in one dimension," Phys. Rev. B **88**, 235117 (2013).

[122] Z. Mei, L. Vidmar, F. Heidrich-Meisner, and C. J. Bolech, "Unveiling hidden structure of many-body wave functions of integrable systems via sudden-expansion experiments," Phys. Rev. A **93**, 021607 (2016).

[123] I. Hen and M. Rigol, "Strongly interacting atom lasers in three-dimensional optical lattices," Phys. Rev. Lett. **105**, 180401 (2010).

[124] M. Jreissaty, J. Carrasquilla, F. A. Wolf, and M. Rigol, "Expansion of Bose-Hubbard Mott insulators in optical lattices," Phys. Rev. A **84**, 043610 (2011).

[125] J. Hauschild, F. Pollmann, and F. Heidrich-Meisner, "Sudden expansion and domain-wall melting of strongly interacting bosons in two-dimensional optical lattices and on multileg ladders," Phys. Rev. A **92**, 053629 (2015).

[126] F. Heidrich-Meisner, S. R. Manmana, M. Rigol, A. Muramatsu, A. E. Feiguin, and E. Dagotto, "Quantum distillation: Dynamical generation of low-entropy states of strongly correlated fermions in an optical lattice," Phys. Rev. A **80**, 041603 (2009).

[127] D. Muth, D. Petrosyan, and M. Fleischhauer, "Dynamics and evaporation of defects in Mott-insulating clusters of boson pairs," Phys. Rev. A **85**, 013615 (2012).

[128] A. Jreissaty, J. Carrasquilla, and M. Rigol, "Self-trapping in the two-dimensional Bose-Hubbard model," Phys. Rev. A **88**, 031606 (2013).

[129] C. D. E. Boschi, E. Ercolessi, L. Ferrari, P. Naldesi, F. Ortolani, and L. Taddia, "Bound states and expansion dynamics of interacting bosons on a one-dimensional lattice," Phys. Rev. A **90**, 043606 (2014).

[130] F. Andraschko and J. Sirker, "Propagation of a single-hole defect in the one-dimensional Bose-Hubbard model," Phys. Rev. B **91**, 235132 (2015).

[131] I. Bouchoule, S. S. Szigeti, M. J. Davis, and K. V. Kheruntsyan, "Finite-temperature hydrodynamics for one-dimensional Bose gases: Breathing-mode oscillations as a case study," Phys. Rev. A **94**, 051602 (2016).

[132] B. Fang, G. Carleo, A. Johnson, and I. Bouchoule, "Quench-induced breathing mode of one-dimensional Bose gases," Phys. Rev. Lett. **113**, 035301 (2014).

[133] L. Vidmar, D. Iyer, and M. Rigol, "Emergent eigenstate solution to quantum dynamics far from equilibrium," Phys. Rev. X **7**, 021012 (2017).

[134] M. A. Cazalilla, "Bosonizing one-dimensional cold atomic gases," J. Phys. B: At. Mol. Opt. Phys. **37**, S1 (2004).

[135] V. Gritsev and A. Polkovnikov, "Integrable Floquet dynamics," SciPost Phys. **2**, 021 (2017).

[136] D. Sels and A. Polkovnikov, "Minimizing irreversible losses in quantum systems by local counterdiabatic driving," Proc. Natl. Acad. Sci. **114**, E3909 (2017).

[137] M. Boninsegni, N. Prokof'ev, and B. Svistunov, "Worm algorithm for continuous-space path integral Monte Carlo simulations," Phys. Rev. Lett. **96**, 070601 (2006).

[138] M. Boninsegni, N. V. Prokof'ev, and B. V. Svistunov, "Worm algorithm and diagrammatic Monte Carlo: A new approach to continuous-space path integral Monte Carlo simulations," Phys. Rev. E **74**, 036701 (2006).

[139] D. M. Ceperley, "Path integrals in the theory of condensed Helium," Rev. Mod. Phys. **67**, 279 (1995).

[140] B. Gaveau and L. S. Schulman, "Explicit time-dependent Schrödinger propagators," J. Phys. A: Math. Gen. **19**, 1833 (1986).

[141] E. B. Manoukian, "Explicit derivation of the propagator for a Dirac delta potential," J. Phys. A: Math. Gen. **22**, 67 (1989).

[142] M. Casula, D. M. Ceperley, and E. J. Mueller, "Quantum Monte Carlo study of one-dimensional trapped fermions with attractive contact interactions," Phys. Rev. A **78**, 033607 (2008).

[143] S.-N. Tan, "Large momentum part of a strongly correlated Fermi gas," Ann. Phys. **323**, 2971 (2008).

[144] S.-N. Tan, "Energetics of a strongly correlated Fermi gas," Ann. Phys. **323**, 2952 (2008).

[145] S.-N. Tan, "Generalized virial theorem and pressure relation for a strongly correlated Fermi gas," Ann. Phys. **323**, 2987 (2008).

[146] R. J. Wild, P. Makotyn, J. M. Pino, E. A. Cornell, and D. S. Jin, "Measurements of tan's contact in an atomic Bose-Einstein condensate," Phys. Rev. Lett. **108**, 145305 (2012).

[147] Z. Ristivojevic, "Excitation spectrum of the Lieb-Liniger model," Phys. Rev. Lett. **113**, 015301 (2014).

[148] A. Del Maestro and I. Affleck, "Interacting bosons in one dimension and the applicability of Luttinger-liquid theory as revealed by path-integral quantum Monte Carlo calculations," Phys. Rev. B **82**, 060515 (2010).

[149] T. Comparin and W. Krauth, "Momentum distribution in the unitary Bose gas from first principles," Phys. Rev. Lett. **117**, 225301 (2016).

[150] K. Van Houcke, F. Werner, E. Kozik, N. Prokof'ev, and B. Svistunov, "Contact and momentum distribution of the unitary Fermi gas by bold diagrammatic Monte Carlo," arXiv:1303.6245 (2013).

[151] A. M. Rey, I. I. Satija, and C. W. Clark, "Noise correlations of hard-core bosons: quantum coherence and symmetry breaking," J. Phys. B: At. Mol. Opt. Phys. **39**, S177 (2006).

[152] K. He and M. Rigol, "Scaling of noise correlations in one-dimensional-lattice-hard-core-boson systems," Phys. Rev. A **83**, 023611 (2011).

[153] E. B. Kolomeisky, T. J. Newman, J. P. Straley, and X.-Y. Qi, "Low-dimensional Bose liquids: Beyond the Gross-Pitaevskii approximation," Phys. Rev. Lett. **85**, 1146 (2000).

[154] P. Vignolo, A. Minguzzi, and M. P. Tosi, "Exact particle and kinetic-energy densities for one-dimensional confined gases of noninteracting fermions," Phys. Rev. Lett. **85**, 2850 (2000).

[155] M. Brack and B. P. van Zyl, "Simple analytical particle and kinetic energy densities for a dilute fermionic gas in a d-dimensional harmonic trap," Phys. Rev. Lett. **86**, 1574 (2001).

[156] M. Rigol, G. G. Batrouni, V. G. Rousseau, and R. T. Scalettar, "State diagrams for harmonically trapped bosons in optical lattices," Phys. Rev. A **79**, 053605 (2009).

[157] Y.-Z. Jiang, Y.-Y. Chen, and X.-W. Guan, "Understanding many-body physics in one dimension from the Lieb-Liniger model," Chinese Phys. B **24**, 050311 (2015).

[158] X.-W. Guan and M. T. Batchelor, "Polylogs, thermodynamics and scaling functions of one-dimensional quantum many-body systems," J. Phys. A: Math. Theor. **44**, 102001 (2011).

[159] Y.-Y. Chen, Y.-Z. Jiang, X.-W. Guan, and Q. Zhou, "Critical behaviours of contact near phase transitions," Nat. Commun. **5**, 5140 (2014).

[160] W. Xu and M. Rigol, "Universal scaling of density and momentum distributions in Lieb-Liniger gases," Phys. Rev. A **92**, 063623 (2015).

[161] S. Pilati and M. Troyer, "Bosonic superfluid-insulator transition in continuous space," Phys. Rev. Lett. **108**, 155301 (2012).

[162] T. T. Nguyen, A. J. Herrmann, M. Troyer, and S. Pilati, "Critical temperature of interacting Bose gases in periodic potentials," Phys. Rev. Lett. **112**, 170402 (2014).

[163] T. Mishra, J. Carrasquilla, and M. Rigol, "Phase diagram of the half-filled one-dimensional $t - V - V'$ model," Phys. Rev. B **84**, 115135 (2011).

[164] S. Rachel, N. Laflorencie, H. F. Song, and K. Le Hur, "Detecting quantum critical points using bipartite fluctuations," Phys. Rev. Lett. **108**, 116401 (2012).

[165] H. F. Song, S. Rachel, C. Flindt, I. Klich, N. Laflorencie, and K. Le Hur, "Bipartite fluctuations as a probe of many-body entanglement," Phys. Rev. B **85**, 035409 (2012).

[166] I. Hen, M. Iskin, and M. Rigol, "Phase diagram of the hard-core Bose-Hubbard model on a checkerboard superlattice," Phys. Rev. B **81**, 064503 (2010).

[167] B. Capogrosso-Sansone, N. V. Prokof'ev, and B. V. Svistunov, "Phase diagram and thermodynamics of the three-dimensional Bose-Hubbard model," Phys. Rev. B **75**, 134302 (2007).

[168] T. Busch, B.-G. Englert, K. Rzażewski, and M. Wilkens, Found. Phys. **28**, 549 (1998).

[169] V. Dunjko, V. Lorent, and M. Olshanii, "Bosons in cigar-shaped traps: Thomas-Fermi regime, Tonks-Girardeau regime, and in between," Phys. Rev. Lett. **86**, 5413 (2001).

[170] K. Winkler, G. Thalhammer, F. Lang, R. Grimm, J. H. Denschlag, A. J. Daley, A. Kantian, H. P. Büchler, and P. Zoller, "Repulsively bound atom pairs in an optical lattice," Nature **441**, 853 (2006).

[171] M. Valiente and D. Petrosyan, "Two-particle states in the hubbard model," J. Phys. B: At. Mol. Opt. Phys. **41**, 161002 (2008).

[172] M. Grupp, R. Walser, W. P. Schleich, A. Muramatsu, and M. Weitz, "Resonant Feshbach scattering of fermions in one-dimensional optical lattices," J. Phys. B: At. Mol. Opt. Phys. **40**, 2703 (2007).

[173] H. P. Büchler, "Microscopic derivation of Hubbard parameters for cold atomic gases," Phys. Rev. Lett. **104**, 090402 (2010).

[174] R. Walters, G. Cotugno, T. H. Johnson, S. R. Clark, and D. Jaksch, "*Ab initio* derivation of Hubbard models for cold atoms in optical lattices," Phys. Rev. A **87**, 043613 (2013).

[175] T. Johnson, S. Clark, and G. Cotugno, *Wannier states for optical lattices* (2013).

[176] V. Eisler, F. Iglói, and I. Peschel, "Entanglement in spin chains with gradients," J. Stat. Mech. **2009**, P02011 (2009).

[177] P. Jordan and E. Wigner, "über das paulische äquivalenzverbot," Zeitschrift Phys. **47**, 631 (1928).

[178] M. P. Nightingale and C. J. Umrigar, *Quantum Monte Carlo methods in physics and chemistry*, 525 (Springer Science & Business Media, 1998).

[179] E. Y. Loh and J. E. Gubernatis, "Stable numerical simulations of models of interacting electrons in condensed matter physics," Electronic phase transitions **32**, 177 (1992).

[180] O. Penrose and L. Onsager, "Bose-Einstein condensation and liquid Helium," Phys. Rev. **104**, 576 (1956).

[181] J. L. Lancaster and A. Mitra, "Quantum quenches in an XXZ spin chain from a spatially inhomogeneous initial state," Phys. Rev. E **81**, 061134 (2010).

[182] W. Xu and M. Rigol, "Expansion of one-dimensional lattice hard-core bosons at finite temperature," Phys. Rev. A **95**, 033617 (2017).

[183] T. Holstein and H. Primakoff, "Field dependence of the intrinsic domain magnetization of a ferromagnet," Phys. Rev. **58**, 1098 (1940).

[184] A. Del Campo and J. G Muga, "Dynamics of a Tonks-Girardeau gas released from a hard-wall trap," Europhys. Lett. **74**, 965 (2006).

[185] A. Del Campo, "Fermionization and bosonization of expanding one-dimensional anyonic fluids," Phys. Rev. A **78**, 045602 (2008).

[186] H. Buljan, R. Pezer, and T. Gasenzer, "Fermi-Bose transformation for the time-dependent Lieb-Liniger gas," Phys. Rev. Lett. **100**, 080406 (2008).

[187] D. Jukić, B. Klajn, and H. Buljan, "Momentum distribution of a freely expanding Lieb-Liniger gas," Phys. Rev. A **79**, 033612 (2009).

[188] J. Kajala, F. Massel, and P. Törmä, "Expansion dynamics in the one-dimensional Fermi-Hubbard model," Phys. Rev. Lett. **106**, 206401 (2011).

[189] M. Collura, S. Sotiriadis, and P. Calabrese, "Equilibration of a Tonks-Girardeau gas following a trap release," Phys. Rev. Lett. **110**, 245301 (2013).

[190] M. Collura, S. Sotiriadis, and P. Calabrese, "Quench dynamics of a Tonks-Girardeau gas released from a harmonic trap," J. Stat. Mech. **2013**, P09025 (2013).

[191] A. S. Campbell, D. M. Gangardt, and K. V. Kheruntsyan, "Sudden expansion of a one-dimensional Bose gas from power-law traps," Phys. Rev. Lett. **114**, 125302 (2015).

[192] G. P. Brandino, J.-S. Caux, and R. M. Konik, "Glimmers of a quantum KAM theorem: Insights from quantum quenches in one-dimensional Bose gases," Phys. Rev. X **5**, 041043 (2015).

[193] J. Ren, Y.-Z. Wu, and X.-F. Xu, "Expansion dynamics in a one-dimensional hard-core boson model with three-body interactions," Sci. Rep. **5**, 14743 (2015).

[194] N. Schlünzen, S. Hermanns, M. Bonitz, and C. Verdozzi, "Dynamics of strongly correlated fermions: *Ab initio* results for two and three dimensions," Phys. Rev. B **93**, 035107 (2016).

[195] N. J. Robinson, J.-S. Caux, and R. M. Konik, "Motion of a distinguishable impurity in the Bose gas: Arrested expansion without a lattice and impurity snaking," Phys. Rev. Lett. **116**, 145302 (2016).

[196] P. M. Preiss, R. Ma, M. E. Tai, A. Lukin, M. Rispoli, P. Zupancic, Y. Lahini, R. Islam, and M. Greiner, "Strongly correlated quantum walks in optical lattices," Science **347**, 1229 (2015).

[197] R. Modak, L. Vidmar, and M. Rigol, "Quantum adiabatic protocols using emergent local hamiltonians," Phys. Rev. E **96**, 042155 (2017).

[198] R. Coïsson, G. Vernizzi, and X.-K. Yang, "Mathieu functions and numerical solutions of the Mathieu equation," in *OSSC* (IEEE, 2009) p. 3.

Vita

Wei Xu

Education

- Ph.D. Physics, Pennsylvania State University, Aug 2012 - May 2018
- B.S. Physics, University Of Science And Technology Of China, Aug 2008 - Jun 2012

Publications

- **W. Xu** and M. Rigol, Expansion of one-dimensional lattice hard-core bosons at finite temperature, Phys. Rev. A **95**, 033617 (2017)
- **W. Xu**, M. Olshanii and M. Rigol, Multiband effects and the Bose-Hubbard model in one-dimensional lattices, Phys. Rev. A **94**, 031601(R) (2016)
- **W. Xu** and M. Rigol, Universal scaling of density and momentum distributions in Lieb-Liniger gases, Phys. Rev. A **92**, 063623 (2015)
- L. Vidmar, **W. Xu** and M. Rigol, Emergent eigenstate solution and emergent Gibbs ensemble for expansion dynamics in optical lattices, Phys. Rev. A **96**, 013608 (2017)

Awards

- David C. Duncan Graduate Fellowship in Physics, 2015/2016